A STUDY OF THE BOUND STATES OF ^{15}O
and
A STUDY OF T = 3/2 STATES IN ^{13}C, ^{17}O, AND ^{21}Ne

Thesis by

David Cecil Hensley

In Partial Fulfillment of the Requirements

For the Degree of

Doctor of Philosophy

California Institute of Technology

Pasadena, California

1969

(Submitted December 13, 1968)

ACKNOWLEDGMENTS

Sincere thanks are extended to Professor C. A. Barnes for his assistance in all phases of this work. His ideas lead to this study of T = 3/2 states, and discussions with him have been stimulating and enjoyable. Thanks are also extended to Professor W. A. Fowler for suggestions and discussions which lead to the study of ^{15}O, and it is hoped that he will find a pleasant blend of nuclear physics and astrophysics in this study. The assistance of the staff of the Kellogg Radiation Laboratory, without which this work would not have been possible, is deeply appreciated. Financial assistance from the Office of Naval Research, from the National Aeronautics and Space Administration, and from the California Institute of Technology is gratefully acknowledged.

ABSTRACT

The bound states of ^{15}O were studied in the $^{16}O(^{3}He, \alpha)^{15}O$ reaction, and the binding energy of the 6th excited state of ^{15}O with respect to $^{14}N + p$ was measured with special care, for astrophysical reasons. In addition, T = 3/2 states in ^{13}C, ^{17}O, and ^{21}Ne were studied in the $(^{3}He, p)$ reaction on ^{11}B, ^{15}N, and ^{19}F and in the $(^{3}He, \alpha)$ reaction on ^{14}C, ^{18}O, and ^{22}Ne. In all cases, the reaction products were analyzed with a 61-cm radius, double-focusing magnetic spectrometer and detected by a 16-counter array in the focal plane of the spectrometer. The results for the four nuclei studied are summarized below.

(1) ^{15}O: the spins and parities of all of the bound states of ^{15}O were either determined for the first time or confirmed. The 6th excited state has $J^{\pi} = 7/2^{+}$ and lies 21.2 ± 0.6 keV below the $^{14}N + p$ threshold; the 5th excited state has $J^{\pi} = 5/2^{+}$. A correction of -4.6 ± 0.6 keV to the previously accepted mass excess of ^{15}O was determined; the new mass excess of ^{15}O is 2855.3 ± 0.6 keV. On the basis of this work, it is shown that the 6th excited state of ^{15}O has a negligible effect on the stellar rate of the $^{14}N(p, \gamma)^{15}O$ reaction.

(2) ^{13}C: four T = 3/2 states were identified in ^{13}C at the following excitation energies (spin and parity are included, where determined): 15105 ± 3 keV ($3/2^{-}$); 18655 ± 10 keV; 18692 ± 15 keV; and 19122 ± 5 keV ($\leq 7/2^{-}$). The 15.10-MeV state has a width, $\Gamma \leq 6$ keV.

(3) ^{17}O: seven T = 3/2 states were identified in ^{17}O at the following excitation energies: 11076 ± 4 keV ($1/2^{-}$); 12467 ± 4 keV ($3/2^{-}$); 12947 ± 5 keV ($1/2^{+}$); 12994 ± 5 keV ($5/2^{-}$); 13636 ± 4 keV ($3/2^{+}$ or $5/2^{+}$); 14210 ± 10 keV; and 14243 ± 10 keV.

(4) ^{21}Ne: five T = 3/2 states were identified in ^{21}Ne at the following excitation energies: 8856 ± 6 keV ($3/2^+$ or $5/2^+$); 9136 ± 6 keV ($1/2^+$); 9962 ± 6 keV ($1/2^-$ or $3/2^-$); 10602 ± 10 keV; and 10901 ± 10 keV.

Analog-state correspondences were made on the basis of relative intensities, excitation energies, and spin-parity assignments; four completed T = 3/2 quartets were established. The completed T = 3/2 quartets were then used to test the quadratic mass equation for isobaric multiplets. Within the experimental uncertainties, the lowest mass-13 and mass-17 quartets are fitted by the quadratic mass equation, but the two lowest mass-21 quartets deviate significantly.

TABLE OF CONTENTS

LIST OF TABLES

I. INTRODUCTION

The first section of this thesis is concerned with the properties and the excitation energies of the bound states of ^{15}O. The initial interest in this nucleus centered on the possible effect that a state near the $^{14}N + p$ threshold in ^{15}O might have on the stellar rate of the $^{14}N(p, \gamma)^{15}O$ reaction. Eventually the study was broadened to learn more about all of the bound states of ^{15}O and to clear up a small but important disagreement in the excitation energy of the state just below the $^{14}N + p$ threshold.

The second section is concerned with locating and studying $T = 3/2$ states in ^{13}C, ^{17}O, and ^{21}Ne and with seeing how strongly these states are excited by $(^3He, p)$ and $(^3He, \alpha)$ reactions. Of additional interest was the testing of the accuracy of a quadratic mass equation for isobaric multiplets; the $T = 3/2$ multiplets provide the first meaningful test of the equation, and for this reason special care was given to a precise determination of the excitation energies of these states.

Both of these studies have in common the use of the 61-cm double-focusing magnetic spectrometer as the instrument for analyzing the reaction products, and the technique used in this work for utilizing the resolution capabilities of the spectrometer in the determination of excitation energies will be discussed in Appendix I. The nature of the nuclear reaction data obtained with the magnetic spectrometer and how they were analyzed will be discussed in the next chapter.

II. EXPERIMENTAL METHOD

A. Application of the Magnetic Spectrometer

Most of the data for this study were taken with the 61-cm double-focusing magnetic spectrometer and the 16-counter array. Because this system has been discussed in detail previously by Groce (1963), McNally (1966), and Moss (1968), only those aspects of the experimental techniques which have a bearing on the present investigation will be discussed here.

The data from the 16-counter array consist of the number of charged particles of a particular type, detected in each of the 16 silicon surface-barrier counters, for some magnetic field setting and for a known integrated incident current. These yields were corrected for the various collection efficiencies of the counters, and the nuclear magnetic resonance (N. M. R.) frequency for each counter was determined directly from the N. M. R. frequency setting for the array (taken to be the frequency of counter eight). Because of the dead spaces between the counters and because of the approximately 0. 3% width in energy of the apertures in front of the counter array, sets of data were taken at slightly differing frequencies in order to fill in the fine details of high resolution spectra.

The observed experimental resolution depends on the energy spread in the incident beam, on the size of the target spot, on the target thickness, on the kinematic energy change over the angular spread of the opening into the spectrometer, and on the width of the apertures in front of the counters in the array. Usually the experimental arrangement was such as to have the target thickness, kinematic-spread, and counter apertures dominate the resolution, with one or more of these three taking precedence depending on the

target, the reaction being studied, and the energies being considered. When only these factors significantly affected the resolution, most of the particle groups in high resolution spectra tended to have approximately triangular shapes. This happens because each of these factors contributes an essentially rectangular resolution function, and, when two equal rectangular resolution functions are folded together, a triangular shape results. The folding in of an additional rectangular resolution function tends to "smooth out" the triangle somewhat. (See the analysis on page 48 of the shape of the proton group from the $^{11}B(^{3}He, p)^{13}C$ reaction.) In a few cases, the experiment was arranged in such a way that the target thickness dominated the contributions to the experimental resolution, and the groups were then approximately trapezoidal. For example, the spectrum in Figure 1 shows a trapezoidal peak resulting from elastic scattering on the moderately thick gold backing for a thin ^{14}C target used in the course of this work. The low energy side (left hand) of this trapezoidal peak is less steep than the high energy side because of the effects of energy-loss straggling in the target. Examples of triangular particle groups can be found in Figures 3 and 5 through 8.

Figure 2 shows the momentum profile of a ^{212}Po α-source as analyzed by the spectrometer; the approximately triangular shape results directly from the dimensions of the α source and the counter aperture (both 1/32"). The triangles at lower field settings were spread out by straggling of the α particles in the targets being measured.

The interest in being able to analyze spectra with triangles arises from the fact that the N. M. R. frequency to be assigned to a particle group is unambiguously given by the frequency corresponding to the peak of the triangle, and the yield, which must be determined

by integrating over the peak, can be obtained in a simple fashion from the area of the triangle (see Appendix III). In most cases, the experimental resolution could not be predicted with better than about 30% accuracy without an unreasonable amount of effort, so that normally only two restrictions were placed on the actual shape of the triangles used to describe the groups.

(1) The triangles in a given spectrum must have approximately the same base width, since this width should be directly related to the experimental resolution. The base width should be roughly consistent with twice the expected experimental resolution. This width may vary slightly for cases where the counter apertures dominate the resolution as the width in energy for the apertures at the high energy end of the array is about 15% greater than for those at the low energy end.

(2) The triangles should not lean to the low energy side -- that is, the peak should not be to the low energy side of the midpoint of the base. (There are some important exceptions, particularly for non-uniform targets.)

The uncertainties in the peak position and the area of the triangle were obtained by seeing how much these quantities would be changed when the triangle was varied within the statistical uncertainties of the data points, but while the two previously discussed restrictions were maintained. Obvious corrections to the area were made for shapes deviating grossly from the triangular shape, and uncertainties in the area were always considered to be at least 5% of the area, even when the statistical uncertainties were much less, because the relative efficiency factors for the various counters, upon which the yield is dependent, were usually not known with any greater precision.

B. Targets

A variety of targets were used in this study, and the major restrictions on the targets were that they be transmitting targets (where the outgoing particles leave the target from the side opposite to the side on which the beam is incident) and that they be reasonably thin (so that the energy loss of the particles in the target was comparable to or less than the energy resolution of the counter apertures).

Most of the targets were prepared by the standard technique of evaporating the target material in vacuo from a heated tantalum boat onto glass slides which had previously been coated with about $4\mu g/cm^2$ of either BaI_2 or $BaCI_2$. When the slide was gently immersed into water, the salt layer dissolved, and the layer of insoluble evaporated material floated off onto the surface of the water. The target layers, which had been cut into the proper sizes while still on the glass slide, were lifted out of the water onto 10-mil-thick tantalum target frames with a 5/16-inch diameter hole, with the layer covering the hole as it was laid down on the surface of the frame. The frame was brought vertically up under the floating target foil, catching the edge of the foil on its edge, and then the frame was gently lifted vertically out of the water. This method for initially attaching the foil to the frame was found to be vastly superior for very fragile foils to the method of simply pushing the floating foil up against the frame while lifting the frame -- a method which usually was sufficiently awkward that fragile foils were destroyed.

A target can often be strengthened and the target thickness effectively doubled by bringing the frame up under the center of the foil so that the foil is laid down on both sides of the frame. The

"doubled-target" and this method of target preparation have several advantages:

(1) As the frame is removed from the water, the water coating the under surface of the floating target foil is squeezed out of the hole by the two layers approaching from either side. During the same process with a single-layer target, the single layer is often ruptured by surface-tension forces acting through the hole in the target frame while the frame is being lifted out of the water. Many fragile foils, which could not be mounted successfully as a single layer because the single layer was too weak for the size of the hole in the frame, were mounted, often easily, as a doubled-target.

(2) Besides external forces, such as water surface tension or pressure from air currents, target foils are often destroyed by internal forces, the most destructive of which causes curling. For materials evaporated at very high temperatures, successive micro-layers of the foil are laid down on layers which have already partially cooled and contracted. When the foil cools, it has a strong tendency to roll or curl up. By doubling a foil, this curling tendency is nullified because the foil adheres across the hole to a foil which tends to curl in the opposite direction. Moreover, a small flaw in a single-layer target may allow the foil to begin curling and tear, but the doubled-target generally matches the flawed section with an unflawed section which supports the flawed section and counteracts any tendency to curl and tear.

(3) Because the two layers are symmetrically positioned with respect to the center of the target, a non-uniform distribution of some material in the original evaporated layer, such as a surface contamination of oxygen, will be symmetrically distributed in the

doubled-foil, eliminating the problem which arises in many experiments of knowing exactly where the contaminant material is in the target.

There are two major disadvantages with doubling:

(1) The target is twice as thick as the original layer-- a difficulty in high resolution experiments where very thin targets are desired.

(2) The doubled foil sometimes stretches itself so tightly against the edges of the hole in the target frame that the foil is weakened there and may come free. The free doubled foil can sometimes be recovered, however, by sticking it to a target frame with a smaller hole.

Materials which could not be made into self-supporting foils, such as WO_3 or CaF_2, were evaporated onto previously mounted foils of carbon, nickel, or gold. Nickel-oxide targets were prepared by heating thin, mounted foils of nickel with a short-focus, high-intensity light source. When targets of $Ni^{18}O$ were required, the heating was performed through the wall of a small,glass bell jar which had been filled with ^{18}O-enriched gas to a pressure of several millimeters of Hg; $Ni^{16}O$ targets were prepared in air. Because NiO is fairly transparent, heating with a light source becomes less efficient as the foil oxidizes. For this reason and because the oxygen must diffuse to the increasingly deeper layers of the foil, targets made in this manner were not completely oxidized throughout their thickness; a 1000-Å nickel foil was measured to have been nearly 70% oxidized by this method.

In order to be able to make ^{14}C targets with very little waste, a special kind of carbon target was prepared, following an idea of Douglas et al. (1956). An A. C. discharge was initiated in

^{14}C-enriched acetylene (at a pressure of about a centimeter of Hg), and polymerized acetylene deposited on foils which covered the electrodes. The foils were 0.5 mg/cm^2 Au backed by 1.0 mg/cm^2 Cu, and, after the acetylene was deposited, the copper was chemically stripped away to leave gold-backed ^{14}C targets.

Finally, a gas target was used for the reactions involving ^{15}N, ^{22}Ne, and, in some experiments, ^{18}O. The gas cell used (Goosman 1967) consisted of a cylinder with an inner diameter of 0.87 inches whose entrance window was covered with a 5000-Å nickel foil and whose exit window was covered by a 10,000-Å nickel foil. A set of rectangular apertures 0.96, 1.47, and 14.0 inches from the gas cell defined the "effective" volume of the gas target, and corrections were made for the change in this effective volume with the spectrometer angle in the final results for angular distributions. A brief discussion of how the gas-cell data were calibrated for excitation-energy measurements is discussed in Appendix I.

C. Target Measurement

The thickness and composition of the targets used were determined either by measuring the energy loss of particles in the target or by comparing reaction yields from the target with those from previously measured targets.

The usual technique for self-supporting targets was to measure with the spectrometer the energy loss in the target of the 8.785-MeV α particles from a ^{212}Po source. Energy losses could readily be measured with an accuracy of 5% for targets where the total energy loss was less than 100 keV; for thicker targets, the α-spectrum was smeared out by energy-loss straggling in the target,

and the uncertainty in the energy loss became somewhat greater. Sample measurements of a ^{11}B and a ^{12}C target by this method are shown in Figure 2.

Some targets were thick enough that their thicknesses could be inferred from the observed experimental resolution for some reaction, usually elastic scattering. For this kind of measurement, the experimental set-up was chosen so that the target thickness would certainly dominate other factors contributing to the experimental resolution, as in the elastic scattering from the gold backing shown in Figure 1.

When the target was not self-supporting, elastic scattering from the backing was measured both directly and with the target material between the backing and the beam, and the target thickness was derived from the observed energy difference in the scattered particles for the two cases; e. g., see Figure 1. The thicknesses of relatively thin backings could be measured in the same way by using the target material as the scatterer. Examples of both kinds of measurement are shown in Figure 3. The above methods were used at lab angles of 90^{o} or greater, and the targets were positioned so that the effects due to the thickness would be enhanced.

The mass per unit area of a target of known chemical composition was inferred from the measured energy loss of particles in the target using the proton-stopping cross-section results of Demirlioglu and Whaling (1962). Targets which had uncertain chemical compositions, such as tungsten-oxide or the partially oxidized nickel foils, were measured by comparing reaction yields from the targets with yields from the same reaction on targets of known chemical composition. For example, the oxygen content of the tungsten-oxide and oxidized-nickel targets was obtained by a

comparison with data from SiO targets and with data taken with pure oxygen in the gas target.

D. Particle-gamma Angular Correlations

Particle-gamma angular correlations were studied with the spectrometer positioned at 0^{o} and with a single charged-particle detector in the focal plane of the spectrometer. A 5-inch diameter by 4-inch long NaI(T1) detector, 13.7 ± 0.1 cm from the target, detected γ-rays at angles of 90^{o}, 120^{o}, 135^{o}, and 150^{o}, with respect to the beam. The γ-ray detector was supported by a wooden table clamped to a part of the target chamber; the angles, which could be determined with an accuracy of about 0.5 degrees, were established by means of lines drawn on the wooden support table.

With this choice of geometry the theoretical description of the α-γ angular correlations takes on a very simple form (see Appendix V). An experimental difficulty with this geometry for the (^{3}He, $\alpha\gamma$) correlations was that, even though the ^{3}He beam was caught in the entrance region of the spectrometer in a 1.2-degree-radius cup, enough multiple scattering took place in the spectrometer that a disturbingly large number of the beam particles were detected in the charged-particle detector. The energy spectrum of these particles was characterized by a fairly narrow peak at an energy close to that of the incident beam and with a very high and long low-energy tail. Unfortunately, all of the correlation measurements of this study were made for outgoing α particles with energies such that both the peak and large tail from the scattered incident beam were present, and the α-particle group was superimposed on the tail. It was found that careful focusing of the beam and slight

changes in the magnetic field of the spectrometer could significantly reduce the effect of the scattered beam -- the latter changes presumably optimized the amount of scattered beam which was trapped behind the internal baffles of the spectrometer. For weak α-particle groups, it turned out to be impossible to normalize the γ-ray energy spectra taken at each angle to the number of α particles detected, and for these cases it was necessary to normalize to the total charge measured in the beam-current integration.

Pulses from the γ-ray detector and from the charged-particle detector were fed simultaneously into two identical coincidence circuits with resolving times of about 80 nsec. One circuit was set in coincidence and the other was set out of coincidence by 2 μsec, each circuit gating one half of a 400-channel analyzer in which the γ-ray energy spectrum was stored. The resolving times of the circuits were adjusted so that their coincidence counting rates, for a totally random input, were equal to within 1%. In this way the true-coincidence spectrum and a properly normalized random-coincidence spectrum could be collected at the same time, making the correction for random events quite straight-forward.

Additional details concerning this experimental set-up are discussed by Moss (1968) and Earwaker and Montague (1968).

III. A STUDY OF THE BOUND STATES OF ^{15}O

A. Introduction

Special interest in the 6th excited state of ^{15}O was generated by a report (Warburton et al. 1965) which placed this state only 8.8 ± 7 keV below the ^{14}N + p threshold in ^{15}O. Because of the possible large effect on the stellar rate of the $^{14}N(p,\gamma)^{15}O$ reaction of a state in ^{15}O very near threshold, and because the rate of the $^{14}N(p,\gamma)^{15}O$ reaction determines the rate of the CNO cycle (Caughlan and Fowler 1962), it became important immediately to know as precisely as possible all those properties of the state which might influence the proton-capture reaction rate. Some of the information on ^{15}O up to the 7th excited state, taken from the report by Warburton et al. (1965), is shown in Figure 4, and it was clear that, even for the bound states, much information on spins and parities as well as on excitations energies remained to be determined.

In a subsequent publication (Hensley, 1967), the present author reported that the 6th excited state had a spin of 7/2 -- a result to be discussed in this paper -- and that the state was 21.6 ± 1.1 keV below the ^{14}N + p threshold. More accurate measurements of the γ rays de-exciting this state were then reported (Alburger and Warburton 1966 and Chasman et al. 1967), placing the state at 16.6 ± 1.3 keV below threshold. The disagreement between these two values suggested a possible internal inconsistency in the excitation-energy scheme for ^{15}O. For this reason and also because of the incomplete nature of the information on the bound states of ^{15}O, it was decided to repeat the measurements on the 6th excited state and to extend the measurements to all of the bound states.

The results of these measurements will be presented in three separate parts: relative and absolute excitation energies; particle angular distributions; and particle-gamma angular correlations. A synthesis of these results with other information, along with a discussion of their astrophysical significance, will be presented in the concluding section of this chapter.

B. Experimental Results

1. Relative and absolute excitations

Because of the special significance of the position of the 6^{th} excited state of ^{15}O with respect to the $^{14}N + p$ threshold, it was decided to measure the (7-6) separation (the separation in excitation energy between the 6^{th} and 7^{th} excited states) and thus to relate the 6^{th} excited state to the threshold through the 7^{th} excited state. The 7^{th} excited state, which lies above threshold (Figure 4), has been studied as a resonance in the $^{14}N(p,\gamma)^{15}O$ reaction, and its energy above threshold has been quite accurately measured. Inasmuch as the α-particle group corresponding to the 6^{th} excited state could be included in the span of the counter array along with the groups for either the 7^{th} excited state or the 4^{th} and 5^{th} excited states, all the separations between these states were studied. The results have been listed in Table I.

The first experiment was performed with a SiO target and with an incident energy of 12 MeV, and data were taken at angles from 30^{o} to 80^{o}. An α-particle spectrum taken at 50^{o} is shown in Figure 5. There was considerable difficulty in analyzing the spectra because α particles from the competing $^{28}Si(^{3}He,\alpha)^{27}Si$ reaction distorted and obscured the ^{15}O α-particle spectra. Groups can be

seen in the spectrum (Figure 5) which do not correspond to known states of either ^{15}O or ^{11}C and which show kinematic shifts with angle consistent with their corresponding to excited states of ^{27}Si.

In order to eliminate this difficulty, the measurements were repeated with targets of tungsten-oxide (listed as WO_3) on carbon backings. Figure 6 shows a spectrum taken under conditions closely similar to those for the previous figure, but now the ^{15}O α-particle spectrum appears to be free of extraneous groups. Because of the ease of making SiO targets, another attempt was made with a SiO target to measure the (7-6) separation, this time at a beam energy of 8 MeV where the Coulomb barrier might significantly reduce the reactions on ^{28}Si. At this lower energy, it was better to work at forward angles to avoid elastic scattering, but, over the angle spread studied (from 15^o to 45^o), the 4^{th} and 5^{th} excited state groups were difficult to examine and were not included.

In all of these measurements, each excitation energy was generally measured at several angles; the separations, however, were derived only from excitation energies measured at the same angle. An uncertainty was assigned to each measurement which included the uncertainty arising from the determination of the N. M. R. frequency of the corresponding particle group but which may have underestimated probable systematic errors (Appendix I). The uncertainties in the separation measurements, derived in the usual manner from the uncertainties assigned to the excitation measurements, normally depended mainly on the uncertainties in the N. M. R. frequencies determined for the two respective particle groups. Since most of the possible systematic errors have negligible effect on the separation energies, this estimate of the uncertainties was felt to be realistic. Several determinations of a separation S

were combined to yield the "best value", the weighted mean:

$$S_{wm} = \frac{\Sigma\, w_i\, S_i}{\Sigma\, w_i} \tag{1}$$

where w_i is the weighting factor and was taken equal to $1/(\Delta S_i)^2$, where ΔS_i was the uncertainty assigned to the i^{th} separation measurement. In almost all cases, the weighted mean agreed closely with the mean value of the measurements. The uncertainty in S_{wm} was taken to be the internal error:

$$e_{int} = (\Sigma\, w_i)^{-1/2} \quad . \tag{2}$$

The external error was also calculated:

$$e_{ext} = \left[\frac{\Sigma\, \delta_i^2\, w_i}{(N-1)\Sigma w_i}\right]^{1/2} \tag{3}$$

where δ_i is the deviation of the i^{th} separation from the weighted mean and N is the number of values being combined. It was found that the external error was typically a factor of two to four smaller than the internal error, and it appeared that the uncertainties in the separation energies might have been overestimated. It was decided to take e_{int} as the uncertainty in the weighted mean, however, to compensate for the possibility of systematic errors.

A comparison can be made with γ-ray energy measurements by using both the value for the $^{14}N + p$ threshold of 7292.8 ± 1.2 keV (Mattauch, Thiele, and Wapstra 1965) and the center-of-mass

proton resonance energy (E_r) for the 7^{th} excited state. This energy was measured by Pixley (1957) in the $^{14}N(p,\gamma)^{15}O$ reaction and was given with respect to a standard calibration resonance in the $^{19}F(p,\alpha\gamma)^{16}O$ reaction. When the resonance energy and its uncertainty are adjusted to take into account the newest value and uncertainty for the calibration reaction (Marion 1966), a value of $E_r = 259.5 \pm 0.3$ keV is obtained. This resonance was also studied by Tangen (1946) who reported a value (similarly adjusted for the same calibration reaction) of $E_r = 259.5 \pm 1.0$ keV, in agreement with Pixley's measurement. By combining E_r with the weighted average value for the (7-6) separation, taken from Table I, it is found that the 6^{th} excited state lies 21.2 ± 1.0 keV below threshold. On the other hand, by subtracting the excitation energy for the 6^{th} excited state obtained from γ-ray energy measurements (Alburger and Warburton 1966 and Chasman et al. 1967), from the previously listed value for the $^{14}N + p$ threshold, it is found that the 6^{th} excited state lies 16.6 ± 1.3 keV below threshold, in apparent disagreement with the 21.2 keV value by 4.6 ± 1.6 keV.

The measurements were then extended to include all of the bound states of ^{15}O. With a 12-MeV beam and a NiO target, data were taken at 9 angles, ranging from 10^o to 70^o. The 50^o spectrum shown in Figure 7 was the only one taken which included the 7^{th} excited state. The arrows in the figure indicate the positions of two intense ^3He-particle groups, originating from elastic scattering on the nickel and the oxygen in the target. At more forward angles, these groups completely masked the α-particle group for the 7^{th} excited state. A spectrum taken at 25^o in the same experiment is shown in Figure 8. The results of the separation measurements from this experiment are listed in both Tables I and II, and there

appears to be quite good agreement of the separation measurements with the γ-ray energies listed in the last column of Table II. This comparison, however, is not precise enough to check closely the γ-ray measurements for the excitation energy of the 6^{th} excited state, particularly because of the large uncertainty in the measurement of the (2-0) separation. This uncertainty is directly related to the uncertainty in the energy calibration of the magnetic spectrometer; for the 5 or 6 MeV difference in α-particle energy between the group for the ground state and those for the excited states, the possible error from this source could easily be as large as 2.5 keV.

As an alternative check, a Q-value determination for the $^{16}O(^{3}He, \alpha)$ reaction leading to the excited states of ^{15}O was made for the 50^{o} data. This determination relied upon the relatively intense elastic scattering on the ^{16}O in the target; this ^{3}He-particle group was measured twice in that data set, and the ^{15}O Q-values were determined relative to this elastic scattering reaction. The results, which do not include the ground-state Q-value since the α-particle group for that state had an uncertain shape, have been converted to excitation energies and are listed in Table III. The excitation energy for the 7^{th} excited state is in good agreement with the value of 7552.3 ± 1.2 keV obtained by adding E_r to the threshold energy, but the remaining excitations show the same ~ 4 keV discrepancy with the γ-ray measurements. These Q-values can be related directly to E_r by the following equation:

$$E'_r = (7\text{-}n) - Q_n + {}^{16}O + {}^{3}He - \alpha - {}^{14}N - p$$

where (7-n) is the excitation-energy separation between the 7^{th} and the n^{th} excited states, Q_n is the Q-value to the n^{th} state, and the

atomic symbols indicate the respective masses. Note that E_r' does not depend on the mass of ^{15}O or any of the γ-ray measurements. E_r' has been calculated for the four states for which the (7-n) separations have been measured and are given below.

State	E_r' (keV)
7	260.2 ± 3.3
6	260.1 ± 2.3
5	260.0 ± 3.9
4	259.3 ± 4.1

The weighted average of the results gives $E_r' = 260.0 \pm 1.6$ keV, in good agreement with the experimental value $E_r = 259.5 \pm 0.3$ keV. This appears to indicate that the Q-value determinations cannot be in error sufficiently to explain the ~4 keV discrepancy.

In an attempt both to measure the Q-value to the ^{15}O ground state and to reduce the uncertainty in the calibration of the magnetic spectrometer, measurements were made at 10^o and 15^o with a 12-MeV beam using thin, doubled, boron targets with a small oxygen contamination which was assumed to be symmetrically distributed with respect to the center of the targets (see page 6). The experiment was intended to determine the ^{15}O Q-values relative to those of the $^{11}B(^3He, \alpha)$ reaction leading to states of ^{10}B, but, fortunately, there were several additional well-measured reactions which could also be used. Table IV lists the reactions used as calibrations for this Q-value determination and, as a check of consistency, the Q-values of the calibration reactions as they were then determined from the data. The internal consistency of the experimental data

appears to be quite good, as evidenced by the close agreement of the output Q-values with the input calibration values.

The results for other reactions which were not known with sufficient precision to be used as calibration reactions are listed in Table VI along with the most recently reported Q-value for the reactions. There is generally very good agreement except for the two results from the $^{11}B(^3He,t)^{11}C$ reaction. The discrepancy in the excitation energy of the 4.32-MeV state of ^{11}C can be examined in an indirect way by combining results from two other sources. In a study of the excited states of ^{11}C, Earwaker and Montague (1968) found an excitation energy for the 1st excited state of ^{11}C of 1999 ± 4 keV, in agreement with the value of 1999.3 ± 2.5 keV of this work. They obtained also a value of 2017 ± 4 keV for the excitation-energy separation of the 4th excited state (6.34 MeV) of ^{11}C and the 2nd excited state (4.32 MeV). If this quantity is subtracted from the excitation energy of 6339 ± 5 keV given by Ajzenberg-Selove and Lauritsen (1968) for the 4th excited state of ^{11}C, a value of 4322 ± 6 keV is obtained for the excitation energy of the 2nd excited state of ^{11}C, in good agreement with the value of 4320.7 ± 0.5 keV of this work but in disagreement with the value of 4305 ± 6 keV given by Ajzenberg-Selove and Lauritsen (1968). Because of this indirect confirmation of one of the questioned $^{11}B(^3He,t)^{11}C$ measurements of this work, no re-evaluation of the boron-target data was felt to be warranted. The results for ^{15}O from these data are summarized in Tables II and III.

Additional measurements of the $^{16}O(^3He,\alpha)^{15}O$ Q-values were made with Ni^{18}O and Ni^{16}O (both ~ 1000-Å Ni) targets at an incident energy of 10 MeV, and these results are included in Tables I, II, and III. The data were analyzed relative to the ground state

groups of ^{17}F and ^{18}F observed in the concomitant $^{16}O(^{3}He, d)$ and $^{16}O(^{3}He, p)$ reactions.

It would appear from the agreement of the measurements of the (2-0) separation (Table II) with the corresponding γ-ray measurement that the discrepancy of ~ 4 keV between the results of the absolute Q-value measurements (Table III) and the γ-ray energies cannot be explained by an error in this energy separation. Moreover, the non-zero, ground-state excitation energy listed in Table III, derived from the measurement of the ground state Q-value, indicates that the discrepancy can be fully explained by an error in the mass of ^{15}O. It is concluded, therefore, that the γ-ray energies, with the exception of the 6180- keV measurement, have been adequately verified by the present energy-level separation measurements and that the major part of the discrepancy in the ^{15}O energies is contained in the mass-table value for the ground-state mass of ^{15}O. On the basis of this conclusion, the separation measurements, Q-value measurements, E_r, and the γ-ray measurements can be combined to give a new value for the mass of ^{15}O; Table VI lists the results of such a combination, where ΔM is the correction to the mass table value (Mattauch, Thiele, and Wapstra 1965) of the ^{15}O mass. The first values are derived from the absolute Q-value measurements of Table III which when compared to the appropriate gamma-ray energies -- either directly or through a separation measurement -- give the correction to the ^{15}O mass. The 3^{rd} excited state was unusual in that it was compared to three different γ-ray energies through the (6-3), (5-3), and (3-2) separations; the 4^{th} excited was compared through the (6-4) and (5-4) separations. Finally, three of the separations were compared to the sum of E_r and the $^{14}N + p$ threshold energy minus the appropriate γ-ray energies. (This last comparison was the first indication of the

discrepancy in the ^{15}O energy scheme.) Not all of the measurements have been included in this analysis, partly because the included measurements have the smaller uncertainties but mainly because these measurements form a set possessing the least internal correlation. If one included more of the measurements, but kept track of all of the correlations, it is doubtful if either the final correction or its uncertainty would be significantly changed. Since all of these values for the mass correction, except for the one from the absolute measurement of the ground-state Q-value, depend on the (2-0) γ-ray measurement, the mass correction should have its strong dependence on this measurement stated clearly along with it. With this restriction, the mass correction can be given as:

$$\Delta M = -4.58 - 0.8\delta \pm 0.6 \text{ keV}$$

$$\delta(\text{keV}) = \{Ex\,(^{15}O_2) - 5241.5\} \ .$$

The quoted uncertainty is slightly larger than the internal error in order to compensate somewhat for the strong dependence of most of the mass corrections on the (2-0) γ-ray energy measurement. Further consequences of this correction and the excitation measurements on ^{15}O will be discussed later.

2. Particle angular distributions

The α-particle angular distributions from the $^{16}O(^3He, \alpha)^{15}O$ reaction leading to the bound states of ^{15}O are shown in Figures 9 through 12. The majority of the data points were obtained with the counter array, but the distributions in Figure 9 for the ground state

and the 3rd excited state were remeasured and extended using a position-sensitive solid-state counter. The error bars contain contributions from counting statistics, peak analysis, and detector efficiencies. There is, in addition to these uncertainties, an uncertainty in the absolute normalization of approximately 10% due largely to uncertainties in the thickness and chemical composition of the targets and to uncertainties in the collection-efficiency factors for the 16-counter array.

The $\ell_n = 1$ experimental angular distributions for the ground state and the 3rd excited state of ^{15}O are shown in Figures 9 and 10. (A discussion of the theoretical distributions is given in Appendix IV.) The dip at forward angles predicted by the DWBA theory for these $\ell_n = 1$ distributions disagrees with the experimental data taken at 12 MeV (Figure 9), though the same experimental distributions taken at 10 MeV (Figure 10) do show this dip. The $\ell_n = 0$ distribution for the 1st excited state is shown in Figure 11 along with the $\ell_n = 2$ distributions for the 2nd, 4th, and 5th excited states; these distributions were taken at an incident energy of 12 MeV. In each case, as with the $\ell_n = 1$ distributions, the ℓ-value assignment is unique even though the comparison of experiment with theory shows only qualitative and not quantitative agreement. That is, there is agreement in general on the angles at which maxima and minima occur even though the theory fails to predict accurately the ratio of the cross-section from one maximum to another.

The distribution for the 6th excited state is shown in Figure 12, and it apparently has a pick-up maximum at 65^o. (Measurements to be presented in the next sub-section limit the ℓ-value to either 3 or 4, and only these ℓ-values will be considered.) The solid curve in the figure was generated by the optical-model code for an $\ell_n = 4$

distribution and obviously fails to predict the position of the maximum; an $\ell_n = 3$ distribution would of course do even worse. If one attempts to analyze the data with a simple plane-wave theory (Appendix IV), it is found that the necessary cut-off radius is smaller than would be expected. In order to describe properly the other data with this plane-wave theory, radii of 6.5 f to 7.25 f are necessary; however, in order to describe properly the experimental distribution for the 6^{th} excited state, a radius of 5.25 f is required for an $\ell_n = 4$ plane-wave distribution (the dashed curve in Figure 12) and 4.25 f for an $\ell_n = 3$ distribution. The $\ell_n = 3$ plane-wave distribution changes very slowly and gives a much broader maximum than does the $\ell_n = 4$ distribution. With either theory, $\ell_n = 4$ is clearly favored over $\ell_n = 3$, but there is no strong case for adopting the $\ell_n = 4$ assignment. It is likely that this strange behavior is related to the proximity of the state to a particle threshold, a fact which is not included in either theory.

The results of the ℓ-value analysis are summarized in Table IX.

3. Particle-gamma angular correlations

The experimental set-up for the study of particle-gamma angular correlations has already been discussed. The theory of the angular correlations for the $^{16}O(^3He, \alpha\gamma)^{15}O$ reaction when the α particles are detected at 0^o has a very simple form with no dependence on specific nuclear models. The theory presented by Litherland and Ferguson (1961) and further discussed by Poletti and Warburton (1965) is presented in brief in Appendix V. The form of the correlation for this special geometry is

$$W(\theta)_{a \to b} = A \sum_k F_k(J_a\, J_b\, X_{ab})\, P_k(\theta)$$

$$W(\theta)_{b \to c} = A \sum_k F_k(J_a\, J_b\, J_c\, X_{ab}\, X_{bc})\, P_k(\theta)$$

where $W(\theta)$ is the γ-ray yield as a function of the angle; the first equation is for a simple decay, and the second equation is for the 2^{nd} part of a cascade decay. A is the normalization of the data; k takes on even values from 0 to $2J_a$; F is a known function of its arguments; X is the multipole mixing; and $P_k(\theta)$ is a Legendre polynomial. The subscripts a, b, and c refer to the separate stages of the decay.

Angular correlations were taken for all but the first of the bound excited states of ^{15}O, and the experimental data for all of the correlations are presented in Figure 13 along with the final theoretical fits to the data. The data were also fitted by an expansion in Legendre polynomials of the form:

$$W(\theta)/A = 1 + a_2 P_2(\theta) + a_4 P_4(\theta)$$

and the a_2 and a_4 coefficients obtained by a least squares adjustment are listed in Table VII.

The data were analyzed by minimizing the following function:

$$Q^2 = \frac{1}{M - R} \sum_j \frac{(W_j' - W_j)^2}{\Delta^2 W_j'}$$

where W_j is the theoretical prediction for the angular correlation and W_j' and $\Delta^2 W_j'$ are the experimental measurement and the square of its uncertainty, respectively. M is the number of experimental

values, R is the number of parameters varied, and the sum is taken over the M experimental values. For a given choice of J_a, J_b, and X_{ab}, the normalization A was varied so as to make Q^2 a minimum; Q^2 has been normalized so that its expectation value for a true fit to the data is 1. A typical result of this analysis is given in Figure 14 for the (2-0) decay, where the value of Q^2 is plotted against the mixing ratio for several spin combinations. If, for a given spin combination, all minimum values of Q^2 are larger than the value indicated by the horizontal line marked "0.1% limit", then there is less than 0.1% statistical chance that the spin combination is correct (Wapstra et al. 1959), and, for such a case, the spin combination was rejected in this work. There are two properties of Q^2 which should be noted:

(1) Q^2, for this experiment, depends only on the multipole mixing and the normalization of the data, for a given spin combination. Thus, for a given value of the multipole mixing, Q^2 is minimized by varying only the normalization.

(2) The formula for Q^2 assumes that the errors are uncorrelated. This seems a good assumption for a single decay, but the data for the two or more γ rays detected in a cascade overlap, and there is certainly some correlation between the errors in the determined yields. The spectrum of the decay of the 7.276-MeV state (to the 5.241-MeV state) is shown in Figure 15; this spectrum is the sum of the spectra taken at the four angles normally used in these correlation measurements. The 5.24-MeV γ ray from the decay of the 2nd excited state clearly affects the determination of the yield of the 2.035-MeV γ ray de-exciting the 7.276-MeV state. For the background correction to the 2.035-MeV γ-ray yield, it was assumed that the 5.24-MeV γ-ray energy spectrum was flat in the

region of the peak corresponding to the 2.035-MeV γ ray, and the probable error in the determined yield was adjusted according to the size of this background correction. It was felt that the correlation in the errors was small and that it had been compensated for in the background correction; consequently, no correlations in the errors were included in the Q^2 analysis.

When a minimum in Q^2 was found below the 0.1% limit for an acceptable choice of spins, the minimum was analyzed with a chi-square analysis described by Smith (1964) in order to obtain the best value for the mixing parameter and its probable error. For all cases where χ^2 (the minimum value of Q^2) was greater than 1, the probable error of the mixing parameter was multiplied by $\sqrt{\chi^2}$. The spin assignments, value of χ^2, and the a_2 and a_4 coefficients derived from the chi-square analysis are listed in Table VII. The corresponding mixing parameters are listed in Table VIII.

The Q^2 analysis for the (2-0) decay, shown in Figure 14, has been limited to only those spin combinations allowed by the previously determined ℓ-values (Table IX). This analysis clearly excludes all spin combinations except a spin of 5/2 for the 2nd excited state of ^{15}O and a spin of 1/2 for the ground state.

A Q^2 analysis for the (3-0) correlation is not shown, but from the fact that the correlation is non-isotropic (see Table VII and Figure 13), a spin of 1/2 is excluded, and the 3rd excited state must have a spin of 3/2. The Q^2 analysis for the (4-0) correlation is shown in Figure 16 and confirms the assignment of a spin of 3/2 to the 4th excited state. Even though the theory is able to determine the spin uniquely in these two cases, the solution for the mixing parameter is double-valued. According to a theorem proved by Rinsvelt and Smith (1964), it is impossible to determine unambigu-

ously the multipole mixing of a γ ray to the ground state by means of intensity-direction measurements alone, if the spin of the decaying state is less than two. Both derived mixing parameters for the spin 3/2 states are accordingly listed in Table VIII.

The 5^{th} excited state decays entirely to the 2^{nd} excited state, and a Q^2 analysis of the (5-2) part of the correlation is shown in Figure 17. This analysis alone is unable, however, to eliminate either of the two spins allowed by the previously discussed ℓ-value, and it is necessary to consider a 2-dimensional Q^2 analysis (Figure 18) of the total cascade in order to select the proper spin. The 0.1% limit comes for $Q^2 = 4.5$ for this 2-dimensional case, and the solution is further restricted in that it must conform to the previous measurement of the mixing for the (2-0) decay (Table VIII). Those mixings (the solution was double-valued) and their probable errors are indicated by the heavy vertical lines in the figure, and it is seen that for a spin of 5/2 there are indeed minima below $Q = 4.5$ and within the error limits on the (2-0) mixing. A similar analysis for a spin of 3/2 excludes this spin assignment as there are no Q^2 minima below 4.5 and none within the error limits of the (2-0) mixing. This can be seen in a less complete fashion in Figure 19 where the 2-dimensional analysis is limited to the line where $X(2\text{-}0) = \tan(6^{\circ})$. In this figure, the Q^2 analysis for a spin of 3/2 obviously fails to satisfy the condition for a solution. A spin of 5/2 can, therefore, be assigned to the 5^{th} excited state.

The 6^{th} excited state also decays entirely to the 2^{nd} excited state, and the Q^2 analysis for the (6-2) correlation is given in Figure 20. Even though the analysis of the particle angular distribution placed no definite limit on the possible spin for this state, information to be discussed in the next section limits the spin to

$\leq 9/2$, and the Q^2 analysis has been limited correspondingly. Spins of 1/2 and 9/2 are clearly excluded by this analysis, and a 2-dimensional analysis excludes a spin of 5/2 because Q^2 fails to drop below the 0.1% limit value of 4.5. The 2-dimensional analysis for a spin of 3/2 has two Q^2 minima below the 0.1% limit, but these minima do not fall within the limits for the (2-0) mixing -- within these limits Q^2 is always greater than 4.5 -- so that a spin of 3/2 is also excluded. The 2-dimensional analysis along the line $X(2\text{-}0) = \tan(6^{\circ})$ (Figure 21) excludes spins of 3/2 and 5/2; the full 2-dimensional analysis for a spin of 7/2 (Figure 22) indicates a very good fit to the data, and the result is in excellent agreement with the previously measured (2-0) mixing. This agreement both allows and favors a spin of 7/2, and the 6^{th} excited state is, therefore, assigned a spin of 7/2.

Since the (2-0) decay was measured in three of the angular-correlation studies, the Q^2 analyses for all three correlations, using the derived values of the spin and multipole mixings (for the initial member of a cascade), are shown in Figure 23. There is very good agreement in these correlation measurements on the mixing for the (2-0) decay. The results of the multipole-mixing analysis for all of the decays are compared in Table VIII with several other measurements of these mixings. There is very good agreement among all of the measurements on the multipole mixings for these decays; the values of Povh and Hebbard (1959) are opposite in sign to the other values because a different sign convention was used.

The results of the angular correlation analyses are summarized in Table IX.

C. Discussion

1. Synthesis with previous results

The conclusions from the synthesis of the measurements of this paper with previous results are collected in Table IX. The excitation energies quoted for the 2^{nd}, 5^{th}, and 6^{th} excited states are derived from the γ-ray energy measurements (Alburger and Warburton 1966 and Chasman et al. 1967), although they have been checked by the work in this paper for general consistency. The excitation for the 1^{st} excited state is derived from the excitation energy for the 2^{nd} excited state minus the (2-1) separation given in Table II. The excitation energy for the 3^{rd} excited state was derived from the (6-3), (5-3), and (3-2) separations applied to the appropriate γ-ray energies. This value differs by two standard deviations from the previous γ-ray energy value (Warburton, Olness, and Alburger 1965) of 6180 ± 4 keV, but the disagreement reflects, perhaps, the difficulty of measuring higher energy γ rays. The excitation energy for the 4^{th} excited state was obtained from the (6-4) and (5-4) separations applied to the corresponding γ-ray energies. The excitation energy for the 7^{th} excited state was obtained by adding $E_r = 259.5 \pm 0.3$ keV to the corrected value for the $^{14}N + p$ threshold.

The new value for the ^{15}O mass excess was obtained by correcting the previous value (Mattauch, Thiele, and Wapstra 1965) by -4.58 ± 0.6 keV, and the uncertainty in the new value is, of course, just the uncertainty in the correction, 0.6 keV. The position for the $^{14}N + p$ threshold in ^{15}O was obtained simply by combining the respective mass excesses, but it was checked also that this value was consistent with the excitation-energy scheme for ^{15}O. The value for the separation between the threshold and the 6^{th} excited

state was obtained from the (7-6) separation and E_r and also from the excitation of the 6th excited state and the new value for the threshold.

It is important to note that the entire scheme for ^{15}O rests heavily on the γ-ray energy measurement for the γ-ray decay of the 2nd excited state, and this dependence has been stated explicitly (page 21) for the correction to the ^{15}O mass--the γ-ray measurement of the excitation energy of the 2nd excited state has a weight of 0.8 in the final correction. If this excitation energy were to be changed, then all of the bound state excitations would be changed by a nearly equal amount, and the $^{14}N + p$ threshold energy relative to ^{15}O would also be changed.

The spin for the 6th excited state was shown to be 7/2, but that conclusion rested on the assumption that the possible spin was limited to $\leq 9/2$. Rolland (1963) found $\ell_p = 2$ for the $^{14}N(d, n)^{15}O$ reaction to the 6th excited state but reported that the theoretical fit was not very good. In view of the difficulty of describing the corresponding angular distribution for the $^{16}O(^3He, \alpha)^{15}O$ reaction, this ℓ-value assignment, which would limit the spin to $\leq 7/2$, should not be given too much weight. A stronger argument can be based on the recently measured mean lifetime of the 6th excited state (Alburger and Warburton 1966) of 1.25 ± 0.3 psec, equivalent to $\Gamma_\gamma = 5.27 \times 10^{-4}$ eV. This would correspond to an E3 transition strength of $\sim 7 \times 10^5$ Weisskopf units (to be compared with an expected strength of < 100) and limits the transition to being quadrupole or lower. Since the transition is to a spin 5/2 state, this limits the spin to $\leq 9/2$. Further evidence limiting the possible spin comes from the measurement (Evans 1967) of a 0.11-eV transition width from the 9.49-MeV level (spin 5/2) to the 6th excited state. For an E2

transition this would represent a strength of over 2000 Weisskopf units, which is already an unreasonably large value. This certainly limits the transition from the spin 5/2 state to be quadrupole or lower and limits the spin of the 6th excited state to $\leq 9/2$. From the particle-gamma angular-correlation measurement of the present work, therefore, it can be concluded that the spin of the 6th excited state of ^{15}O is 7/2.

The ℓ-value assignments for the angular distributions from the ^{14}N(d, n)^{15}O and ^{16}O(^{3}He, α)^{15}O reactions provide evidence that the parity of the state is even, but this evidence cannot be considered conclusive because of the uncertainties in the ℓ-value assignments. The significance of the dipole transition widths for gamma decays to and from the 6th excited state can be assessed in a simple way proposed by Wilkinson (1960). If Γ_γ/E_γ^3, where Γ_γ is in eV and E_γ is in MeV, is greater than 4×10^{-2}, the transition is most probably E1; if it is less than 4×10^{-4} the transition is most probably M1. The 0.11-eV width of the transition from the 9.49-MeV state ($5/2^-$) to the 6th excited state gives a value for Γ_γ/E_γ^3 of 1.0×10^{-2}; this value favors an identification of the transition as E1, which would indicate even parity for the 6th excited state, but the possibility of the transition being M1 is not rigorously excluded. The 5.27×10^{-4} eV wide transition of the 6th excited state to the 2nd excited state ($5/2^+$) gives a value for Γ_γ/E_γ^3 of 6.2×10^{-5}; this value strongly excludes an E1 transition, and an M1 transition assignment requires that the 6th excited state have even parity. An even parity is assigned to the state on the basis of the ℓ-value assignments and the analysis of the transition widths, and the 6th excited state of ^{15}O, therefore, has $J^\pi = 7/2^+$.

The final results of the synthesis of the information on ^{15}O are given in Table IX and in Figure 24.

2. J-dependence

There has been some discussion of "j-dependence" in the angular distributions from the (^{3}He, α) reactions on isotopes of Ni and Fe (Glashausser and Rickey 1967) and also in the $\ell_n = 1$ angular distributions in the ^{16}O(^{3}He, α)^{15}O reaction (Max-Planck Institut für Kernphysik 1966). Because of the 6 MeV difference in Q-values between the two bound states in ^{15}O having $\ell_n = 1$ distributions in the ^{16}O(^{3}He, α) reaction, Q-value effects tend to mask any small j-dependence, particularly in the position of the forward maxima. The 2nd and 3rd maxima of the $1/2^-$ distribution appear to be shifted to smaller angles relative to the $3/2^-$ distribution (see Figure 9), but the present data are not sufficiently extensive to reveal unambiguously such an effect. The $\ell_n = 2$ distributions (Figure 11), however, appear to show clear indications of j-dependence effects; for these distributions there is little or no Q-value effect as the excitation separations are at most 1.6 MeV and as little as 70 keV. Note in Figure 11 that the distributions for the 2nd and 5th excited states (with $J^\pi = 5/2^+$) have their maxima to the right of the theoretical predictions while that for the 4th excited state (with $J^\pi = 3/2^+$) has its maxima to the left. Figure 25 shows a different presentation of the same effect with the plots of the simple ratios of cross-sections for the three $\ell_n = 2$ distributions. The states and their spins have been identified in the figure at the right of the curves (the smooth curves serve only to connect the data points). The two ratios of cross-sections of spin 5/2 to spin 3/2 show a clear maximum near 39^o. The ratio for spin 5/2 to spin 5/2 is relatively smooth over the same region, failing to reproduce the maximum at 39^o. Thus it appears that the $\ell_n = 2$ distributions for spin 5/2 states differ in a

distinctive way from the $\ell_n = 2$ distribution for the spin 3/2 state, and the assumption is made that these differences result from j-dependence.

3. Astrophysical significance of the 6th excited state of ^{15}O

Since the excitation energy, spin, parity, and lifetime of the 6th excited state of ^{15}O have now been established, an estimate can be made of the effect of this state on the stellar rate of the $^{14}N(p,\gamma)^{15}O$ reaction.

The cross section for the $^{14}N(p,\gamma)^{15}O$ reaction can be written in the form of $\frac{S(E)}{E} \exp(-211.8/E^{1/2})$, in order to isolate the rapidly varying Coulomb barrier factor. S(E) is in keV-barns and E is the center-of-mass energy of the proton in keV. The single-level resonance formula described by Marion and Fowler (1957) can then be used to calculate the contribution of the 6th excited state to the cross-section factor S(E). Because the state has $J^{\pi} = 7/2^+$, the reaction requires the protons incident on ^{14}N (1^+) to have an orbital angular momentum $\ell_p = 2$. The remainder of the symbols in the formulae below are either standard or are made clear through numerical substitution.

$$S(E) = 3.93 \times 10^6 \frac{\theta_p^2}{A} \Gamma_\gamma \omega \frac{(E_R E_C)^{1/2}}{(E-E_r)^2} f_\ell \exp\left(4\left(\frac{E_C}{E_R}\right)^{1/2}\right) \text{ eV-barns}$$

$$E_R = \frac{10 \text{ MeV}}{A(A_0^{1/3} + A_1^{1/3})^2} = \frac{10}{\frac{14}{15}(1 + 2.41)^2} = 0.922 \text{ MeV}$$

where $$R = 1.44 (A_0^{1/3} + A_1^{1/3}) f$$

$$E_C = \frac{Z_1 Z_0 \text{ MeV}}{A_1^{1/3} + A_0^{1/3}} = \frac{1 \times 7}{3.41} = 2.05 \text{ MeV}$$

$$E_\ell = (\ell + 1/2)^2 E_R = \frac{25}{4} \, 0.922 = 5.77 \text{ MeV}$$

$$f_\ell = \left(\frac{E_C + E_\ell}{E_C}\right)^{1/2} \exp\left\{-2(\ell + 1/2)^2 \left(\frac{E_R}{E_C}\right)^{1/2}\right\} = \left(\frac{7.82}{E_C}\right)^{1/2} e^{-8.39}$$

$$\omega = \frac{2J + 1}{(2J_0 + 1)(2J_1 + 1)} = \frac{4}{3}$$

$$S = 3.93 \times 10^6 \, \frac{\theta_p^2 \, \Gamma_\gamma(\text{eV})}{(E\text{-}E_r)^2_{\text{MeV}}} \, \frac{15}{14} \, \frac{4}{3} \, (0.922 \times 7.82)^{1/2} e^{-8.39+5.97} \text{ eV-barns}$$

$$S = \frac{\theta_p^2 \, \Gamma_\gamma(\text{eV})}{(E\text{-}E_r)^2_{\text{keV}}} \, 1.342 \times 10^6 \text{ eV-barns} \; .$$

$E\text{-}E_r$ is the energy separation between the 6^{th} excited state and the excitation in ^{15}O reached by protons of energy E (center-of-mass). For protons with zero energy ($E_p = 0$), $E\text{-}E_r = 21.2 + 0.6$ keV. The total gamma width has been measured to be $\Gamma_\gamma = (5.25 + 1.0) \times 10^{-4}$ eV (Alburger and Warburton 1966). The equation then reduces to:

$$S = 1.57 \times \theta_p^2 \text{ eV-barns} \; . \qquad (17)$$

If this quantity is divided by the value of 3.12 keV-barns given by Caughlan and Fowler (1962) for $S(E_p = 0)$, we obtain:

$$\frac{S}{3.12 \text{ keV-barns}} = 5.0 \times 10^{-4} \times \theta_p^2 \qquad (18)$$

An estimate of θ_p^2 can be made (Marion 1966) by comparing the excitation energy of the 6th excited state in ^{15}O with that of its analog in ^{15}N and by assuming that $\theta_n^2 = \theta_p^2$, where θ_n^2 is the neutron reduced width for the analog state. A value for θ_p^2 of about 0.06 is found by this method. This derivation is not very reliable for such light nuclei, but the result is consistent with the expectation that $\theta_p^2 \leq 1$. Even for $\theta_p^2 = 1$, the correction to the published value of $S(E_p = 0)$ arising from the contribution from the 6th excited state of ^{15}O is less than 0.1% and can safely be neglected in calculating the rate of the $^{14}N(p, \gamma)^{15}O$ reaction at stellar temperatures.

IV. A STUDY OF T = 3/2 STATES IN ^{13}C, ^{17}O, AND ^{21}Ne

A. Introduction to T = 3/2 States

The study of T = 3/2 states in light nuclei in this laboratory was initiated by Lauritsen and Barnes (Lynch, Griffiths, and Lauritsen 1965) in the study of $^{7}Li(^{3}He, p)^{9}Be(T = 3/2)$ and by Dietrich (1965) who studied $^{7}Li(^{3}He, n)^{9}B(T = 3/2)$. The $(^{3}He, n)$ work was extended to T = 3/2 states in ^{13}N and ^{17}F by Adelberger (1967). As part of a program to match the $(^{3}He, n)$ results in ^{13}N and ^{17}F and to extend the previous studies, this work is concerned with the search for T = 3/2 states in ^{13}C, ^{17}O, and ^{21}Ne using the $(^{3}He, p)$ and $(^{3}He, \alpha)$ reactions.

One of the aims of the present work was to determine precisely the excitation energies of the T = 3/2 states. The quadratic mass equation for isobaric multiplets has three unknown coefficients, and a T = 3/2 quartet with four masses is the smallest multiplet affording a test of the validity of the quadratic equation. The equation may be derived from 1^{st} order perturbation theory on the assumption that the forces splitting the masses of an isobaric multiplet are weak compared to the strong nuclear forces and transform under isospin rotations like the Coulomb force; it has the form (Wilkinson 1964 and 1966):

$$M(T, T_z) = a(T) + b(T)T_z + c(T)T_z^2$$

where $M(T, T_z)$ is the mass of the T_z member of the T-multiplet; a, b, and c are coefficients independent of T_z (their dependence on T has been made explicit in order to simplify some later discussion);

and $T_z \equiv (Z-N)/2 = Z - A/2$. The equation is expected to be valid to order of $\bar{Z}\alpha$ (Weinberg and Treiman 1959), where $\bar{Z}$ is the average value of Z in the multiplet and α is the fine-structure constant. A large deviation from this equation would indicate the possibility of a charge dependence in the strong nuclear force. However, because any deviation of the strong nuclear force from charge independence is expected to be small (e. g., from nucleon-nucleon scattering; Henley, 1966), it is necessary to measure the multiplet masses as accurately as possible in order to provide any significant test of the mass equation.

For the purpose of having an approximate formula with which to predict the expected mass of a $T = 3/2$ state, it is convenient to assume that only the Coulomb force and the neutron-proton mass difference cause the splitting in the isobaric multiplet and that the Coulomb effect can be approximated as a $KZ(Z-1)$ effect, with K depending mainly on A and assumed to be a constant in a given multiplet. Then the mass of a member of the multiplet can be written as:

$$M(T, T_z) = ZM_p + (A-Z)M_n - B + KZ(Z-1)$$

where B is the binding energy due to the strong forces and is assumed to be constant across the multiplet. This equation can be compared with the previous equation to give:

$$b(T) = K(A-1) - (M_n - M_p)$$

$$c(T) = K = \frac{b(T) + (M_n - M_p)}{A - 1} \quad .$$

In all of the cases to be studied here, the mass of the neutron-rich end member of the multiplet, M(3/2, -3/2), is known; thus, if one other mass or mass relation can be found, M(3/2, -1/2) may be solved for. A consequence of the quadratic mass equation is:

$$b(3/2) = M(3/2, 1/2) - M(3/2, -1/2)$$

and the approximation to be used in this paper for estimating unknown masses of T = 3/2 states is:

$$b(3/2) \tilde{=} b(1/2) = M(1/2, 1/2) - M(1/2, -1/2) \ ;$$

i.e., it is assumed that the splitting of the T = 1/2 multiplet is the same as that for the two inner members of the T = 3/2 quartet. This assumption is equivalent to evaluating K from the ground state mass difference of the $T_z = \pm 1/2$ nuclei. With these assumptions, the mass of the T = 3/2 state of interest in this work can be written as:

$$M(3/2, -1/2) = M(3/2, -3/2) - \frac{2(M_n - M_p)}{A - 1}$$

$$+ \frac{A-3}{A-1} [M(1/2, 1/2) - M(1/2, -1/2)] \ .$$

More than the approximate excitation energy of the T = 3/2 states must be known, unfortunately, to be able to identify the T = 3/2 states among the many T = 1/2 states likely to lie nearby. Fortunately the T = 3/2 states are expected to exhibit characteristics which depend on the isospin purity of the state or on the isospin symmetry across the multiplet, and these characteristics should assist in the identification of the state.

(1) In $T_z = \pm 1/2$ light nuclei with $A = 4n + 1$ ($n > 1$), the lowest $T = 3/2$ states are expected to be bound with respect to isospin-conserving particle decays. Although these states lie at excitation energies far above one or more particle-emission thresholds, the isospin inhibition on these decays suggests that the widths of the states should be much smaller than those of any nearby $T = 1/2$ states.

(2) Reaction cross-sections tend to decrease with increasing excitation energy as the structure of the states becomes more complicated and the wave functions of the reacting nuclei have only a small overlap with the wave function describing the state. The lower $T = 3/2$ states, however, are isospin analogs of the low-lying states in the nucleus with $T_z = -3/2$ and are expected to have relatively simple structures; the reaction cross-sections leading to these states are, consequently, expected to be relatively large, comparable with those to the low-lying $T = 1/2$ states and hopefully much larger than those to the $T = 1/2$ states in the region of excitation energy of the $T = 3/2$ states. Of the two reactions to be used in this work, the $(^3He, p)$ and $(^3He, \alpha)$ reactions, it is likely that the $(^3He, \alpha)$ reaction will have the smaller over-lap with complicated states. Because the $(^3He, p)$ reaction can sequentially transfer a neutron and proton or can transfer the two particles as either a ($T = 1$, $S = 0$) "excited deuteron" or a ($T = 0$, $S = 1$) deuteron, it is expected that this reaction can populate more complex states, and the distinction between cross-sections to $T = 1/2$ states and $T = 3/2$ states may not be as great with this reaction.

(3) Even when the magnitudes of the cross-sections to $T = 3/2$ states are not in themselves distinctive, they may be profitably compared with those from mirror reactions -- $(^3He, n)$, (t, p), and (t, α) -- to the corresponding analog states. It is expected that ratios of these

cross-sections will be very similar, and this comparison of cross-sections may be able to clarify the isospin assignment for a particular state.

The method adopted for the present study of T = 3/2 states was to examine ^{13}C, ^{17}O, and ^{21}Ne with the (^{3}He, p) and (^{3}He, α) reactions to see if any narrow states would appear near the excitation energies expected for the T = 3/2 states. Cross-sections to these states were then compared with those to any neighboring states and with cross-sections for mirror reactions to known or suspected analog states. On the basis of this information, isospin assignments were made, and any T = 3/2 states found were examined in greater detail.

B. T = 3/2 States in ^{13}C

1. Introduction

The study of T = 3/2 states presented in this work was begun with the hunt for a T = 3/2 state in ^{13}C near 15.16 MeV (predicted from the mass of ^{13}B). Targets of ^{11}B (enriched to 98.6%) on tantalum backings were used, and the $^{11}B(^{3}He, p)$ reaction was studied at several angles around and including 90^{o}, at an incident energy of 8 MeV. There were many proton groups in the 90^{o} spectrum (shown in the upper portion of Figure 26), but an examination of the known excited states of ^{14}N and ^{18}F (Ajzenberg-Selove and Lauritsen 1959) indicated that all of the observed groups could be adequately explained as resulting from the (^{3}He, p) reaction on the ^{12}C or ^{16}O contamination in the target. A search for a state in ^{13}C within 1 MeV either way from the predicted value proved entirely fruitless, and after painfully verifying that the (^{3}He, p)

reaction excited all of the listed states of ^{14}N and ^{18}F in the proton-energy region of interest, it was decided that something was either wrong with the theory and expectations or with the experiment. A visual examination of the target revealed that the ^{11}B layer had fallen off the tantalum backing. When a new ^{11}B target was positioned and the experiment repeated, a new and prominent proton group appeared in the 90^{o} spectrum, shown in the lower portion of Figure 26. The dramatic appearance of this group, which proved to correspond to the lowest T = 3/2 state in ^{13}C (at 15.10 MeV), was an exciting introduction to the presence of higher T-states and a pleasant fulfillment of the expectations concerning the appearance of T = 3/2 states in an excitation-energy region where many T = 1/2 states were expected. A further study at several angles failed to reveal the presence of any other states in ^{13}C within 500 keV excitation energy of the 15.10-MeV state whose proton groups stood out significantly above the background continuum of protons.

It is perhaps important to digress a moment and discuss the background which is a general feature of the spectra of T = 3/2 states at high excitation energies. One source of a smooth background of particles would be the feeding of a large number of broad T = 1/2 states whose particle groups overlapped and, thus, washed out any of the features characteristic of isolated states. Other possible sources include sequential decays in which the detected particle was not emitted first or many-particle break-ups. Because the T = 3/2 states in ^{13}C, ^{17}O, and ^{21}Ne are far above both neutron and α-particle thresholds, sequential decays and many-particle break-ups are energetically allowed. Thus, a possible difficulty in finding and examining weakly excited T = 3/2 states in these nuclei will be that they are superimposed on backgrounds which may be large enough to

mask their presence; and such backgrounds can be noted in all of the spectra to be presented in this work.

A search was made for T = 3/2 states at higher excitation energies. The isobar diagram in Figure 27 shows that these states are expected to lie at least 3.5 MeV above the 15.10 MeV state, on the basis of the known states of ^{13}B (Middleton and Pullen 1964). Figure 28 shows a ^{11}B(^{3}He, p) spectrum taken at 10^{o} at an incident energy of 12 MeV. Spectra from the (^{3}He, p) reaction on ^{12}C and ^{16}O are also included in this figure in order to indicate which groups probably do not correspond to states of ^{13}C. A state in ^{13}C at 19.12 MeV is clearly evident, and there is a doublet apparent at 18.67 MeV. There is perhaps some evidence for a state at 18.5 MeV, but it and another state expected nearby (see Figure 27) are likely to be only weakly excited in this reaction, on the basis of the analogous cross-sections in the ^{11}B(t, p)^{13}B reaction (Middleton and Pullen 1964), and their presence is masked by the background and by the contaminant groups.

An examination of the excitation-energy region from 18.4 MeV to 18.8 MeV (Figure 29) with a self-supporting ^{11}B target, which fortuitously had a reduced oxygen contamination, revealed that the 18.67-MeV doublet apparently is superimposed on a group from a moderately broad state of ^{13}C. The presence of this broad group made it very difficult to analyze the doublet, and reliable angular distributions could not be extracted for these states. The spectrum in Figure 29 also covers the expected position of the analogs of the first two excited states of ^{13}B, but the data fail to clarify whether the observed groups correspond to states of ^{13}C or to states of ^{18}F. The groups are much too weak to track kinematically, and their identification as states of ^{13}C is not justified on the basis of this work.

As part of the program to examine the T = 3/2 states as thoroughly as possible, the $^{14}C(^{3}He, \alpha)$ reaction to the lowest T = 3/2 state in ^{13}C was also examined, and an α-particle spectrum taken with this reaction at 10^{o} is shown in Figure 30. The incident energy was 15 MeV, and a gold-backed ^{14}C target was used. The upper spectrum in this figure is the result of the $(^{3}He, \alpha)$ reaction on a gold-backed ^{12}C target similar to the ^{14}C target, and this spectrum helps identify groups in the lower spectrum which probably result from ^{12}C and ^{16}O impurities in the ^{14}C target. The 15.10-MeV ^{13}C (T = 3/2) state is very prominent in this spectrum, and there is some indication of a weakly excited state in ^{13}C at a lower excitation energy. This reaction was not pursued further at this point for two reasons:

(1) The rather thick gold backing hurt the resolution and provided such intense elastic scattering of the beam that it was difficult to observe the reaction at slightly greater angles where elastically-scattered ^{3}He particles masked the α-particle groups in the counter array.

(2) The data from the $^{11}B(^{3}He, p)$ reaction to this state were sufficient for determining the excitation energy, spin, and parity of the state.

2. Excitation energies

The excitation energy of the lowest T = 3/2 state in ^{13}C at 15.10 MeV was measured relative to several different reactions:

(1) Spectra were taken at an incident energy of 8 MeV with tantalum-backed ^{11}B targets. The target thicknesses were measured by elastically scattering the beam at 90^{o} on the target backing (see Section C of Chapter II), and the spectra were calibrated relative to the high energy edge of the 90^{o} elastic scattering on the clean side of

the target backing. These measurements were part of initial experiments in which insufficient care had been taken to ensure that the magnetic field of the spectrometer was always properly cycled, and the uncertainty in the derived excitation energy is correspondingly large. As the data were calibrated relative to an edge rather than to a peak, an additional error may arise from the combining of these different kinds of data. A value of 15107 ± 6 keV was obtained from these measurements.

(2) The Q-value to the 15.10-MeV state was included in one part of the study of the bound states of ^{15}O (see Table V). The targets were very thin so that the uncertainty in the target thickness contributed little to the uncertainty in the ^{13}C Q-value. Because many reactions were used for the calibration (Table IV), the probable error in the spectrometer calibration constant was greatly reduced. The major uncertainty in the final Q-value arose mainly from the uncertainties in determining the N. M. R. frequency for the particle group -- the group was measured only three times in the data set. The value for the excitation energy from these measurements was 15104.5 ± 1.4 keV. There is a possible systematic error in this value because only one (^{3}He, p) reaction was used for the calibration and because the N. M. R. frequencies of the proton groups corresponding to this reaction were lower than those for all of the particle groups used for the calibration. This possible systematic error will be included later in the final determination of the uncertainty in the excitation energy.

(3) The thicknesses of self-supporting targets of ^{12}C and ^{11}B (the target with the reduced oxygen contamination) were measured with a ^{212}Po α-source (Figure 2), and proton spectra from the (^{3}He, p) reaction were taken with both targets at an incident

energy of 8 MeV and at angles of 0^{o}, 10^{o}, 20^{o}, 55^{o}, 90^{o}, and 130^{o}. The spectra covered proton energies corresponding to the following states: ^{13}C (15.10 MeV), ^{14}N (2.313 MeV), and ^{18}F (0.0 MeV). The results of this examination are listed in Table X. Each excitation energy is followed by an uncertainty derived, as described in Appendix I, from the uncertainty in the derived value for the incident energy and from the uncertainty in the N.M.R. frequency of the corresponding proton peak. Only the data from the boron target were used for the ^{13}C Q-value determination, though the data from the carbon target were used to check the derived value for the incident energy. The two derived values for the incident energy were 8017.7 ± 1.3 keV (boron target) and 8018.3 ± 1.3 keV (carbon target), and these values agree with the nominal value of 8008 ± 15 keV established by the 90^{o} beam-analyzing magnet. The high value at 55^{o} for $^{18}F(0)$ was not used in the calibration because the corresponding proton group was very weak and had been distorted by several unidentified groups. Finally, all of the 130^{o} values are low, possibly indicating some systematic error in that measurement. No correction was made for this possible error; the 130^{o} data were included in both the calibration data and in the ^{13}C Q-value data. If the data at each angle were kept separate and the ^{13}C Q-value were derived relative to the calibration reactions at each of the angles, the final result would differ by less than 0.1 keV from the result in Table X.

Because these eight separate ^{13}C Q-value determinations in Table X are accompanied by estimated probable errors, the question arises whether to take the average or the weighted average of the values (given at the bottom of the column). Following a suggestion by Birge (1932), the mean value of the probable errors, $\bar{e}$, and the

root mean square of the variance in the probable errors, RMS($e - \bar{e}$), were found. According to the same reference, the relative error in $\bar{e}$, if the probable errors have a normal distribution, should be $0.4761/\sqrt{N}$, where N is the number of measurements. The comparison in Table X of this predicted value with that derived from this set of probable errors indicates that the probable errors do have a normal distribution, and the measurements should, therefore, be considered as having equal weights. For this reason, the average value of the measurements of 15105.3 ± 0.6 keV was taken as the "best value". The statistical uncertainty assigned to this value compares favorably with the 0.6 keV probable error (internal) which is given with the weighted average value. In addition to this statistical uncertainty, there are uncertainties of a systematic nature arising from the spectrometer calibration (about 1 keV), from the target thickness (about 1 keV), and from the calibration reactions (about 0.5 keV). When these uncertainties are folded together, a value of 15105.3 ± 1.6 keV for the excitation energy is found for this set of measurements.

This value can now be combined with the two other values, where each value is weighted by the inverse square of the stated uncertainties. This procedure would indicate an internal error of 1.0 keV (and an external error of 0.4 keV), but it is possible that this analysis tends to underestimate the effect of certain systematic errors. All three Q-value determinations were made relative to reactions which produced particles with N. M. R. frequencies higher than those for the protons corresponding to the 15.10-MeV state in ^{13}C. In this case, the probable errors from the target thicknesses and the spectrometer calibration constant are systematic and should not be averaged out (Appendix I); the probable errors in the Q-value

of the reaction used for the calibration also should not be averaged out of the uncertainty in the ^{13}C Q-value. Because each of these possible sources of error could reasonably contribute about 1 keV to the probable error in the Q-value, a probable error of 3 keV is adopted (somewhat arbitrarily), and the final value for the excitation energy of the lowest T = 3/2 state in ^{13}C is 15104.9 ± 3 keV.

The higher T = 3/2 states were measured relative to the 15.10-MeV state in a series of experiments with self-supporting targets. The data were taken at an incident energy of 12 MeV and at angles from 0^{o} to 40^{o}. The major uncertainty in the excitation energy for the 19.12-MeV state came from the spectrometer calibration constant, since the particle energy for this state differed by about 4 MeV from that for the 15.10-MeV state. The doublet at 18.67 MeV was very difficult to resolve, and the uncertainties in the determination of the N.M.R. frequencies for the two groups dominated the final uncertainties in the excitation energies for the doublet states. The 19.12-MeV state had also been included in the ^{15}O study (Table V).

The results of all of the excitation-energy determinations are summarized in Table XI.

3. Particle angular distributions

Angular distributions for the 15.10-MeV state were taken at both 8-MeV and 12-MeV incident energy (Figures 31 and 32). The major difficulty in the analysis of the data for the angular distribution at 8 MeV was the presence in the spectra of numerous groups from the $^{16}O(^{3}He, p)^{18}F$ reaction. Data were extracted at some angles where groups for states in ^{18}F overlapped the group for the state in ^{13}C by taking data with an ^{16}O target and correcting for the ^{18}F

groups. The angular distribution was partially repeated at an incident energy of 12 MeV, and the distribution for the 19.12-MeV state (Figure 32) was measured at this incident energy out to an angle at which it became extremely difficult to recognize the weak group on the large background. Attempts were also made to obtain distributions for the 18.67-MeV doublet, but few meaningful results could be extracted because of the complexity of the spectra. The error bars in the angular distributions contain contributions from counting statistics, peak analysis, and the detector collection efficiencies. There is an additional 10% uncertainty in the absolute normalization of the angular distribution in Figure 31 due to uncertainties in the thickness and chemical composition of the targets. Similarly, there is an additional uncertainty of 20% in the absolute normalization of the angular distributions in Figure 32. The angular distributions for the 15.10-MeV state require L = 0, and the distribution for the 19.12-MeV state is best fitted with L = 2. The interpretation of these L-values depends on the states having T = 3/2 (see Appendix IV) and will be discussed later.

4. Width measurement

Because the 15.10-MeV state is bound with respect to isospin-conserving particle decays, it is expected to have a relatively small width, and special efforts were made to measure this width. A spectrum taken at 0^{o} at an incident energy of 8 MeV is shown in Figure 33 and, as the expected resolution agrees well with the observed resolution, the width of the state is probably less than 15 keV.

Two spectra were then taken at 140^{o} with tantalum-backed thin ^{11}B targets. The spectrum for the thinner target is shown in

Figure 34, and the results of the two measurements are given below:

Measured Resolution	Kinematic	Spectrometer	Target	Folded
8.0 ± 0.7	6.1	7.1	6.3	8.3
10.3 ± 1.0	7.6	7.1	9.6	10.2

where all values are in keV. The kinematic spread in energy resulted from the finite opening in the theta direction into the spectrometer. The resolution of the spectrometer was derived from the resolution observed for the high energy edge of the thick target yield of elastic scattering on clean tantalum. The target thickness was derived from the observed energy loss in the target of the elastically scattered beam. The resolution was taken to be 1/2 the base width of the triangle through the data points. The major sources of uncertainty in determining the resolution were the size of the background, an apparent shoulder on the low-energy side of the peak (observed in both spectra), and the statistical fluctuations in the data points.

An attempt was made to explain the observed resolution from the three discussed sources of energy spreading; all were considered to be strictly rectangular resolution functions with widths as given above, and these rectangles were directly folded together. The result of this folding for the thinner target is shown in Figure 34 as the continuous curve, and the resolution predicted from this simple folding process (last column above) appears to agree well with the observed resolution.

Then, in order to estimate what minimum width the state could have and still not effect the above calculations, various triangles were folded in with the previous quantities. A triangle with a width

(FWHM) of 4 keV changed the predicted resolution for the thinner target data from 8.3 keV to 9.1 keV, an effect large enough to be observed. Since the resolution predicted from the folding without the triangle agreed fairly well with the experimental resolution, the width of the state was taken to be on the order of or less than 4 ± 1 keV. When this number is converted to the center of mass, the limit on the width of the 15.10 MeV-state is: $\Gamma \leq 6$ keV.

The widths of the states in the 18.67-MeV doublet could not be extracted because of the large uncertainties in the group shapes in the complex spectra associated with those states. The 19.12-MeV state was observed at 10^{o} with a very thin ^{11}B target, and an upper limit on the width of the state of 15 keV could be set. The high background and the presence of proton groups from the $^{16}O(^{3}He, p)^{18}F$ reaction (see Figure 28) prevented a better estimate of the width of this state.

5. Conclusions

Both the $^{11}B(He, p)$ and $^{14}C(He, \alpha)$ reactions strongly populate an isolated state in ^{13}C at 15.10 MeV, very close to the excitation energy expected for the lowest $T = 3/2$ state in ^{13}C. The angular distribution for this state from the $(^{3}He, p)$ reaction requires $L = 0$, a value consistent with the spin and parity expected for the lowest $T = 3/2$ state in ^{13}C, and the width of the state is much less than would normally be expected for a state at this excitation energy. For these reasons, it is concluded that the 15.10-MeV state is the lowest $T = 3/2$ state in ^{13}C and that the stripping pattern observed must, therefore, be due to the transfer of a ($T = 1$, $S = 0$) "excited deuteron" (in order to conserve isospin; see Appendix IV), and this leads to an assignment of $J^{\pi} = 3/2^{-}$ for this state.

The doublet at 18.67 MeV and the 19.12-MeV state are likely also to be T = 3/2 states on the basis of their having relatively small widths and being populated by the (^{3}He, p) reaction at excitation energies near those where higher T = 3/2 states are expected. Their cross-sections relative to that for the 15.10-MeV state agree well with the relative cross-sections from the ^{11}B(t, p) reaction to the 3rd, 4th, and 5th excited states of ^{13}B (Middleton and Pullen 1964); and they agree well with the results of the ^{11}B(^{3}He, n) reaction to T = 3/2 states in ^{13}N (Adelberger 1967). For these reasons these states are also identified as T = 3/2 states. A T = 3/2 doublet was expected near 18.45 MeV, but a careful search failed to reveal the unambiguous presence of these states. This is consistent with the ^{11}B(t, p) results which found only very weak transitions to these states and with the ^{11}B(^{3}He, n) results which also failed to show the presence of these states.

An isobar diagram has been constructed in Figure 27 on the basis of the above information, linking several states across the multiplet. The state in ^{13}N at 18.44 MeV has been matched with the 3rd and 4th excited states of ^{13}B on the basis of the comparison of the results of the ^{11}B(^{3}He, p) and the ^{11}B(^{3}He, n) reactions.

The lowest T = 3/2 state in ^{13}C has also been observed in the ^{15}N(p, ^{3}He) reaction (Cerny et al. 1966 and Ball and Cerny 1966). In addition, the state has been observed as a compound-nucleus resonance in the ^{9}Be + α reaction (Miller 1966). (The excitation energies from these references are listed at the bottom of Table XI.) Miller set an upper limit of 7 keV on the width of the state and measured a small gamma branch to the ground state and to the first three (unresolved) excited states, confirming the conclusion of the present work that the state has a very small width for particle emission.

C. T = 3/2 States in ^{17}O

1. Introduction

The lowest T = 3/2 state in ^{17}O is expected to lie at an excitation energy of 11.00 MeV (predicted from the mass of ^{17}N), and the $^{18}O(^3He, \alpha)$ and $^{15}N(^3He, p)$ reactions were used to study ^{17}O from an excitation energy of about 10 MeV up to about 14.5 MeV. Spectra from the $^{18}O(^3He, \alpha)$ reaction taken at 10^o and 15^o are shown in Figure 35; the data were taken at an incident energy of 10 MeV with an ^{18}O-oxidized 1000-Å nickel target. There are seven groups from ^{17}O evident in the $(^3He, \alpha)$ spectrum; the other groups, resulting from the ^{12}C and ^{16}O contamination in the target, are marked according to the final nucleus. The 12.99-MeV group, which is just a shoulder on the 12.95-MeV group, is clearly defined at larger angles where it eventually becomes larger than the 12.95-MeV group. The first state of ^{17}O below the 11.08-MeV state observed in the $(^3He, \alpha)$ reaction had a width greater than 100 keV and an excitation of 10.5 ± 0.1 MeV. Because the 11.08-MeV state is very near the excitation energy expected for the lowest T = 3/2 state and because the excitation energies of the six other states relative to the 11.08-MeV state (see Figure 36) agree well with the excitation energies of the known excited states of ^{17}N (Ajzenberg-Selove and Lauritsen 1959), it is assumed that all of these states are T = 3/2 states.

Spectra from the $^{15}N(^3He, p)$ reaction at 10^o and 30^o are shown in Figure 37; the data were taken at an incident energy of 12 MeV with the gas target. The ^{15}N gas (enriched to better than 99%) was at a pressure of about 9.5 cm (Hg). It is interesting to note that the $^{15}N(^3He, p)$ reaction to the 12.95-MeV state has such a small

cross-section that the proton group for this state could not be separated from the background; the proton group for the 13.64-MeV state was also very weak. The very broad and strong proton group in the (^{3}He, p) spectrum results from the p(^{3}He, p)^{3}He reaction on hydrogen in the gas target; it is broad because of the extremely large kinematic shift with angle of this reaction. In addition to the T = 3/2 states noted in the ^{18}O(^{3}He, α) spectra, many additional states of ^{17}O are apparent in the ^{15}N(^{3}He, p) spectra in Figure 37; however, because they do not correspond to states seen in the ^{18}O(^{3}He, α) reaction, because they are weaker by an order of magnitude in the ^{15}N(^{3}He, p) reaction than the states already assumed to be T = 3/2 states, and because they would not be easily accounted for as analogs of states of ^{17}N, these states were assumed to be T = 1/2 states, and their investigation has been deferred to a later study.

2. Excitation energies

Since the resolution achievable with the gas cell was considerably poorer than that with the self-supporting solid targets, and since the (^{3}He, α) data contained groups from the ^{16}O(^{3}He, α) reaction to use for the Q-value calibration, the ^{18}O(^{3}He, α) reaction was used to obtain the excitation energies of the T = 3/2 states. All of the Q-values for the ^{16}O(^{3}He, α) reaction which were used as calibrations in this study were determined in the earlier study of the bound states of ^{15}O (Table IX), and differ from those which would be calculated from the mass tables of Mattauch, Thiele, and Wapstra (1965). Whenever possible, the ^{16}O(^{3}He, d)^{17}F and ^{16}O(^{3}He, p)^{18}F reactions were also used as calibration reactions.

The ^{17}O states at excitation energies of 12.47, 12.95, and 12.99 MeV were examined relative primarily to the 2nd excited state of ^{15}O, a state with a small uncertainty in its Q-value and for which the α-particle group is very close in energy to all three of these states of ^{17}O. The 13.64-MeV state was measured relative to the 3rd excited state of ^{15}O; the doublet at 14.2 MeV was measured relative to both the 3rd excited state of ^{15}O and to the 4th and 5th excited states. The group for the 11.08-MeV state of ^{17}O is not very close to those of either the ground or 1st excited state of ^{15}O, and the uncertainty in its Q-value was increased by the lack of a very close $^{16}O(^3He, \alpha)$ calibration reaction. It was possible, however, to use both the $^{16}O(^3He, p)$ and $^{16}O(^3He, d)$ reactions for calibration reactions. The $^{12}C(^3He, \alpha)$ reaction was not used as a calibration because of the uncertainty in the position of the ^{12}C in the nickel-oxide targets.

There is some question whether the ^{16}O and the ^{18}O have the same distribution in the nickel target, with respect to target-thickness corrections. Because of the way the targets were oxidized with ^{18}O, it seems reasonable to assume that the ^{18}O content was symmetrically distributed, but the distribution of ^{16}O, which was a contaminant in the nickel foils before they were heated in the ^{18}O atmosphere, may not have been symmetric in the foils. It was assumed that identical target-thickness corrections could be used for the ^{16}O and the ^{18}O data, as long as a transmission geometry was used, for the following reasons:

(1) The error in an ^{17}O Q-value resulting from a non-symmetric ^{16}O distribution in the target is largely cancelled out, when the target is used in transmission geometry, by the nearly equal energy losses in the target of the incident ^3He particles and the outgoing α particles. For a 1000-Å nickel-oxide target, the possible

error is less than 5 keV for angles less than 50^{o}.

(2) A comparison of the results for the 13.64-MeV state relative to the 3rd excited state of ^{15}O was made using a doubled nickel-oxide target (which should have a symmetric ^{16}O distribution -- see page 6) with a thickness of approximately 2500-Å and using a 1000-Å nickel-oxide target (single), both in transmission geometry. For the extreme case of the ^{16}O being a surface layer on only one side of the 1000-Å target, the results should have differed by about 5 keV, and no such difference was apparent in the comparison. Data with the 1000-Å target were also taken with the target rotated 180^{o}, and no apparent shift in the results from these data was detected, although an effect of approximately 6 to 8 keV would have been expected for a surface layer of ^{16}O on just one side of the target.

(3) There appeared to be no noticeable difference between the results obtained using the $^{16}O(^{3}He, \alpha)$, $^{16}O(^{3}He, d)$ and $^{16}O(^{3}He, p)$ reactions, even though the radical difference in the energy losses in the target of the outgoing particles should have greatly distorted the results if the target had had a non-symmetric ^{16}O distribution.

The results for the ^{17}O excitation energies calculated from the $^{18}O(^{3}He, \alpha)$ data are summarized in Table XII. The following items contributed to the final uncertainties in the excitations:

(1) The $^{16}O(^{3}He, \alpha)^{15}O$ Q-values -- about 1.5 keV

(2) Target thickness -- about 0.5 keV

(3) Location of ^{16}O in the targets -- about 2 keV

(4) Spectrometer calibration -- about 1 keV.

The remaining uncertainties, particularly for the 14.2-MeV doublet, arose from uncertainties in the N.M.R. frequencies determined for the groups.

The $^{15}N(^{3}He, p)$ gas-target data were analyzed using the parameters for the nickel windows which are discussed in Appendix I and in Section C on the excitation energies in ^{21}Ne. These parameters were good enough to determine the excitation energies from this data to about 20 keV, and the results (Table XII) confirm that only the states of ^{17}O at 11.08, 12.47, and 12.99 MeV were strongly populated in the $^{15}N(^{3}He, p)$ reaction.

3. Particle angular distributions

Angular distributions for the three T = 3/2 states which were strongly populated in the $^{15}N(He, p)$ reaction were taken at an incident energy of 12 MeV (an effective incident energy of 11.86 MeV after correcting for energy losses in the entrance foil and the target gas). The data, taken at angles from 5^{o} to 50^{o}, were corrected for the changing effective volume of the gas target. These distributions are shown in Figure 38. The error bars indicate chiefly the uncertainty in the area analysis of the peaks. In addition to this uncertainty there is an uncertainty in the absolute normalization of approximately 20%, arising from the gas pressure measurement and the effective volume correction. The apparently low points at 5^{o} in the two L = 2 distributions may have been affected by poor beam-current integration at this extreme forward angle -- a significant number of recoiling particles may have been able to pass through the colimating slits and affect the beam-current integration. The distribution for the 11.08-MeV state clearly requires L = 0, as expected for the lowest T = 3/2 state. The distributions for the states 12.47 and the 12.99 MeV are much broader than the L = 0 distribution and are best fitted with L = 2. Results from the $^{18}O(^{3}He, \alpha)$ angular distributions (to be discussed below) confirm

L = 2 for the distribution for the 12.47-MeV state but do not clarify the situation for the 12.99-MeV state. Because the distribution for the 12.99-MeV state has the same shape as the L = 2 distribution for the 12.47-MeV state and because the distribution is best fitted with L = 2, an assignment of L = 2 is made for the distribution for the 12.99-MeV state. Similar data were taken at an incident energy of 9 MeV, and they confirm the L = 0 assignment to the distribution for the 11.08-MeV state. At this lower energy the variation with angle of the L = 2 distributions was too small to permit an L-value assignment, but the two distributions again had identical shapes.

Data for the $^{18}O(^{3}He, \alpha)$ angular distributions, shown in Figure 39, were taken at incident energies of 10 and 12 MeV. The error bars indicate chiefly the uncertainty in the determined area of the peaks. Since the angular distributions were derived using NiO-target data, it was necessary to measure the ^{18}O content of these targets; however, the ^{18}O content of the NiO targets could not be inferred from energy loss measurements alone because the precise chemical composition of these targets was not known. Consequently, the absolute normalization for the distributions was established by comparing reaction yields using $Ni^{18}O$ transmission targets with equivalent reaction yields using the gas target filled with ^{18}O enriched to better than 99%. The results indicated that the 1000-Å nickel targets were roughly 75% oxidized - the ratio of ^{18}O to ^{16}O in these targets was about 5 to 1, indicating that 1000-Å nickel foils have a minimum ^{16}O content of 10 or 15% of that of a totally oxidized foil. (The same comparison method was used to check the normalization of the $^{16}O(^{3}He, \alpha)$ angular distributions, which had been established by energy-loss measurements with SiO targets, and there was agreement within the assigned uncertainties.)

The uncertainty in the absolute normalization of the $^{18}O(^3He, \alpha)$ angular distributions is approximately 20%; this uncertainty arose almost equally from the pressure measurement, from the effective volume correction, from the current integration, and from the determined yields -- the background correction to the yields was most uncertain for the gas-target data.

The angular distributions for the states at 11.08 and 12.47 MeV are best fitted with $\ell_n = 1$. The distributions for the 12.95-MeV state could not be extended past 25^o experimentally because of interference from groups for the 1^{st} and 2^{nd} excited states of ^{15}O and for the 1^{st} excited state of ^{11}C, but a unique assignment of $\ell_n = 0$ can be assigned to these distributions because they are so strongly forward peaked. The distributions for the 13.64-MeV state were fitted with $\ell_n = 2$.

The angular distribution for the 12.99-MeV state was very difficult to obtain for the following reasons:

(1) The cross-section for forming this state at 10-MeV incident energy was small.

(2) The state lies within 50 keV of the strongly forward peaked 12.95-MeV state, making the data difficult to analyze at the forward angles.

(3) Contaminant groups from states of ^{11}C and ^{15}O obliterated the group from this state at angles larger than 30^o.

(4) The state has a comparably small cross-section at 12-MeV incident energy, prohibiting any clear check of the 10-MeV incident-energy results.

The angular distribution for this state is given in Figure 40. There are five sets of data incorporated into this figure; three of the sets were taken with the 16-counter array, and two of the sets were

taken with a position-sensitive counter (PSC). The PSC spans about 0.5 MHz at 29 MHz and was set so as to simultaneously study the five groups centered at 28.8 MHz in the upper spectrum of Figure 41. Because there was not room in Figure 40 to indicate all the error bars, uncertainties have been indicated for only some of the data. The least difficulty (and uncertainty) was experienced with the points at 25° and 30°; at these (C.M.) angles the α group for the state was reasonably distinct. The major difficulty generally was in determining the background correction to the yield. The 15° spectrum in Figure 35 shows that the ratio of the peak to the background is only about 2 to 1. In a higher-resolution spectrum shown in the upper portion of Figure 41, this ratio is improved slightly, but the uncertainty in the background correction is still large because of the fluctuations in the background. (The data in Figure 41 correspond to the letter n in Figure 40; those of Figure 35 correspond to the letter s.)

The ends of the distributions are very uncertain because of the interference of other groups. The 10° spectrum in Figure 35 shows the distorting effect at forward angles of the 12.95-MeV state of ^{17}O, whose distribution peaks strongly at forward angles. The 30° spectrum in Figure 41 indicates the difficulties at larger angles; it is clear from a comparison of the 15° spectrum with the 30° spectrum that the ^{15}O and ^{11}C groups will totally obscure the ^{17}O 12.99-MeV group at only slightly larger angles. Both the high and low points at 36° (30° in the lab) in Figure 40 have probably been distorted by these interfering groups.

The poor agreement of the data sets with each other is mainly an indication of the difficulties of estimating the background under the weak particle group. The trend of the data is actually better defined

than would be indicated by the sample error bars, for, while there were large uncertainties in the background corrections, the background was estimated in a systematic way within each data set and should not have strongly affected the actual shape of the distribution. The dotted line in Figure 40 is the author's conception of the trend of the data -- the distribution appears to peak near 30^{o} and to be dropping off on both sides of this angle.

On the assumption that the 12.99-MeV has T = 3/2 and that L = 2 for the $^{15}N(^{3}He, p)$ angular distribution to this state (see above), the ℓ-value for a direct reaction pick-up in the $^{18}O(^{3}He, \alpha)$ would be limited to $\ell_n = 1$ or $\ell_n = 3$. The arrows at the top of Figure 40 indicate the positions predicted by the distorted-wave theory for the first maxima for $\ell_n = 1$ and $\ell_n = 2$; the entire $\ell_n = 3$ curve is displayed in the figure. The nature of the distribution appears to exclude an $\ell_n = 1$ assignment. The trend of the data, as indicated by the dotted line, is only poorly explained by the theory with $\ell_n = 3$. It is possible that the theory, utilizing the parameters discussed in Appendix IV, incorrectly predicts the position of the maxima for the $^{18}O(^{3}He, \alpha)$ angular distributions; an examination of the distributions in the lower portion of Figure 39 suggests that the theoretical distributions are shifted from the experimental data to larger angles. If this is so, then the description of the data in Figure 40 by an $\ell_n = 3$ angular distribution would be improved. However, because of the elusive nature of the data for this distribution and because of its apparently slow variation with angles, an assignment of $\ell_n = 3$ to the distribution for the 12.99-MeV state must be considered tentative.

Angular distributions for the 14.2-MeV doublet were not extracted because of the small cross-sections to these states and because their particle groups overlapped and made the determination of their yields very uncertain.

The results of the analysis of the ^{17}O angular distributions are summarized in Table XIII.

4. Width measurements

Because of the poorer resolution of the gas-target data, the data from the $^{18}O(^3He, \alpha)$ reaction on the oxided, 1000-Å nickel foil have been used to estimate the widths of the T = 3/2 states in ^{17}O. However, in order to minimize the effects of the target thickness on the resolution, only incident energies of at least 10 MeV were used, and the energy resolution of the counter apertures (with 1/16 inch slits) was of the order of 20 keV. A comparison of the widths of the α-particle groups for the T = 3/2 states with the widths of the α-particle groups for the bound states of ^{15}O and ^{11}C indicates that all the T = 3/2 states in ^{17}O below the 14.2-MeV doublet have widths less than 20 keV. An upper limit of 40 keV for the widths of the states of 14.2 MeV can be set from this data; the difficulties in analyzing this weak doublet prevent a better estimate of their widths.

5. Conclusions

The state at 11.08 MeV in ^{17}O is identified as the lowest T = 3/2 state because:

(1) It is only 80 keV above the excitation energy predicted for the lowest T = 3/2 state, and the width of the state is less than 20 keV, in spite of its high excitation energy.

(2) It was the only narrow state within 1 MeV of the predicted excitation which has a measurable cross-section in the $^{18}O(^3He, \alpha)$ reaction, and the state has a relatively large cross-section in the $^{15}N(^3He, p)$ reaction.

(3) The angular distribution ℓ-values for the two reactions leading to this state agree with the expected spin and parity of the lowest T = 3/2 state.

Based upon the assignment of T = 3/2 to the 11.08-MeV state, the remaining states can be recognized as T = 3/2 states because:

(1) Their excitation energies relative to the 11.08-MeV state agree well with the excitation energies of the known states of ^{17}N (see Figure 36).

(2) The states below an excitation energy of 13.76 MeV--the energy of the lowest, isospin-allowed particle-emission threshold --have widths less than 20 keV, expected for T = 3/2 states which are bound to isospin-conserving particle decays. (The doublet at 14.2 MeV is unbound by over 400 keV to ^{16}N + p, but the states still have widths less than 40 keV.)

(3) Only these states are measurably excited in the ^{18}O(^{3}He,α) reaction. That is, no obviously T = 1/2 states at these excitation energies are measurably excited in this reaction, and, on the basis of this apparently selective nature of the reaction, T = 3/2 can be assigned to these states. The ^{15}N(^{3}He, p) reaction which does measurably excite some T = 1/2 states in this excitation region populates some of the states suspected to have T = 3/2 with strengths an order of magnitude greater than those for the T = 1/2 states.

Although there is no ^{15}N(t, p) work with which to compare the ^{15}N(^{3}He, p) data, the ^{15}N(^{3}He, n) reaction to T = 3/2 states in ^{17}F has been studied by Adelberger (1967). This reaction strongly populates three T = 3/2 states in ^{17}F, but no T = 1/2 states are measurably excited. The two lowest T = 3/2 states have L = 0 and L = 2 angular distributions, respectively; Adelburger was unable to make an L-value assignment for the highest state, but its distribution

was very similar to the L = 2 distribution. The results of the $^{15}N(^3He, p)$ and $^{15}N(^3He, n)$ reactions to the T = 3/2 states are in complete agreement, both as to relative cross-section, L-values, and relative excitation energies. The only apparent difference between the results of the two reactions is that the $^{15}N(^3He, n)$ reaction did not measurably populate T = 1/2 states near the T = 3/2 states -- presumably a reflection of the more complicated nature of the $(^3He, p)$ reaction. To 1st order, the $(^3He, p)$ "direct" reaction may proceed via the transfer of either a (T = 1, S = 0) or (T = 0, S = 1) neutron-proton pair; whereas the $(^3He, n)$ reaction is restricted to a (T = 1, S = 0) two-neutron pair.

An apparent j-dependence can be seen in the ℓ_n = 1 distributions to the states at 11.08 and 12.47 MeV, with the distribution for the 1/2$^-$ state (11.08 MeV) shifted to smaller angles. A similar effect was noted earlier for the ℓ_n = 2 distribution seen in the $^{16}O(^3He, \alpha)$ reaction.

A summary of the analysis of the spins and parities of the ^{17}O T = 3/2 states is given in Table XII.

D. T = 3/2 States in ^{21}Ne

1. Introduction

The T = 3/2 states of ^{21}Ne were looked for with the $^{19}F(^3He, p)$ and $^{22}Ne(^3He, \alpha)$ reactions. Unfortunately, the $^{19}F(^3He, p)$ reaction appears to populate T = 1/2 states just as strongly as it does the T = 3/2 states, making it very difficult to identify the T = 3/2 states. Spectra taken at 0^o and 20^o in the $(^3He, p)$ reaction are shown in Figure 42; the data were taken at an incident energy of 10 MeV on a carbon-backed CaF_2 target. The lowest T = 3/2 state is expected to

lie at an excitation energy of 8.79 MeV (based on the mass of ^{21}F). The results of the ^{19}F(t, p) reaction (Horvat 1964) indicate that the lowest T = 3/2 state should be populated by a weak L = 2 transition, and it is not at all clear which of the several states near 8.80 MeV is the lowest T = 3/2 state. The 1st excited T = 3/2 state (near 9.07 MeV) should be populated by a strong L = 0 transition, but, unfortunately, there are two, strong L = 0 transitions to states near the expected excitation energy -- at 9.060 and 9.137 MeV -- and either of these states could be the T = 3/2 state. (It should be noted in Figure 42 that the two states near 9.1 MeV have been divided in the 0^{o} spectrum by a factor of 6.) The ^{19}F(t, p) results further indicate that the (^{3}He, p) cross-sections to higher T = 3/2 states should be expected to be small, and the (^{3}He, p) investigation was, consequently, not extended to higher excitation energies.

The ^{22}Ne(^{3}He, α) reaction was studied at an incident energy of 12 MeV using a gas target; a 10^{o} spectrum which extends from the ground state of ^{21}Ne up to an excitation energy of about 12 MeV is shown in Figure 43. Beginning at an excitation energy of 8.86 MeV, very close to the expected position of the lowest T = 3/2 state, several states are populated with strengths comparable to those of the lowest states T = 1/2 of ^{21}Ne. The excitation energies of these states, relative to that of the 8.86-MeV state agree well with the excitation energies of the known states of ^{21}F (Figure 44), and it assumed, therefore, that the states at 8.86, 9.14, 9.96, 10.60, and 10.90 MeV have T = 3/2. The states at 10.60 and 10.90 MeV may, in fact, be doublets as they match up with known doublets in ^{21}F, as shown in Figure 44, but there was no direct evidence in the present work to support such a conclusion. Besides the states assumed to have T = 3/2, there are several states above 8.86 MeV which are weakly populated in

the $^{22}Ne(^{3}He,\alpha)$ reaction -- for example, the state at 9.48 MeV -- but, because these states are weakly populated and do not match up with any ^{21}F states, they were assumed to be T = 1/2 states. Spectra in Figure 45 taken at 5^{o} and 15^{o} in the $^{22}Ne(^{3}He,\alpha)$ reaction show additional details of the excitation-energy region near the T = 3/2 states.

2. Excitation energies

The $^{19}F(^{3}He, p)$ reaction was not used to extract precise excitation energies for the T = 3/2 states for two reasons.

(1) The excitation energies of states of ^{21}Ne up to 9.3 MeV were studied in this reaction with high resolution by Hinds and Middleton (1959). They quote uncertainties of 10 keV for most of the states, and it was felt that it would be difficult to improve sufficiently on their numbers to justify a detailed study of the excitation energies with this reaction.

(2) The $^{19}F(^{3}He, p)$ reaction populates the lowest T = 3/2 state so weakly that it would be very difficult to extract a good excitation energy for this state from the very complicated proton spectra.

Instead, it was decided to use the $^{22}Ne(^{3}He,\alpha)$ gas-target data for deriving the excitation energies, even though these data have poorer resolution. Because the T = 3/2 states were very strong in the data, the corresponding groups were relatively easy to analyze, and, because many reactions which could be used for calibrations were observed in the same data, the objections to the poorer resolution of the data were largely overcome.

The excitation energies were derived relative to the $(^{3}He, p)$, $(^{3}He, d)$, and $(^{3}He,\alpha)$ reactions on the ^{22}Ne and on a small ^{16}O contamination in the gas target. The calibration reactions used are

listed in Table XV, and the actual procedure used in extracting the desired excitation energies is described in Appendix I. The $^{16}O(^{3}He, \alpha)$ reaction again played an important role in this calibration process because the 6.173-MeV state of ^{15}O stood out clearly in the data (Figures 43 and 45) and helped to bracket the T = 3/2 states between calibration reactions. This calibration procedure appeared to be able to reproduce the many Q-values used for the calibration to better than 3 keV, and it was assumed, therefore, that the overall uncertainty in this process for deriving excitations was 3 keV. The root-mean-square deviation of the excitation-energy determinations for the three lowest T = 3/2 states was somewhat less than 6 keV, and this was taken as the random probable error in a determination; this error arises mainly from the uncertainty in the N. M. R. frequencies determined for the particle groups. Since 7 or 8 determinations were made for each of the excitation energies, the probable error in the final energy was less than 3 keV. This was then added onto the approximately 3-keV systematic uncertainty arising from the calibration procedure to give an overall uncertainty of 6 keV in the excitation energies of the three lowest T = 3/2 states in ^{21}Ne. The uncertainties in the excitation energies for the states at 10.60 and 10.90 MeV are larger because these states are weaker in this reaction than are the three lowest T = 3/2 states--the N. M. R. frequencies for the corresponding particle groups were, consequently, more uncertain -- because fewer determinations were made, because contaminant groups affected the particle groups (particularly for the 10.60-MeV state), and because the overall resolution was poorer for these states -- the lower energy α particles associated with these states lose much more energy getting out of the gas target than those associated with the lower T = 3/2 states.

The excitation energies for the two lowest T = 3/2 states are compared in Table XIII with the results of the $^{19}F(^{3}He, p)$ reaction (Hinds and Middleton 1959), and this comparison clears up the ambiguity as to which states populated by the $^{19}F(^{3}He, p)$ reaction have T = 3/2. The very good agreement on the excitation energy for the state at 9.14 MeV is gratifying as the analysis of the gas-target data, particularly for the poorer resolution $(^{3}He, \alpha)$ reactions, was fairly involved. The discrepancy noted in the excitation energy for the T = 3/2 state at 8.86 MeV is likely due to the very weak yield of this state in the $^{19}F(^{3}He, p)$ reaction. The state, besides being weak, is within 88 keV of the 8.768-MeV state, which shows up very strongly in the $(^{3}He, p)$ reaction (see Figure 42) and which possibly distorts the group for the 8.86-MeV state. All of these proton groups are superimposed on a background which contains possible contributions from many-body reactions and broad states of ^{21}Ne. For these reasons, it is felt that the 16 ± 12 keV discrepancy between the results from the two reactions for the excitation energy of the state should not be considered significant to the gas-target result.

3. Particle angular distributions

The angular distributions from the $^{19}F(^{3}He, p)$ reaction to the two lowest T = 3/2 states were taken at an incident energy of 10 MeV, and these distributions are shown in Figure 46. The error bars for the 9.14-MeV distribution are mainly from counting statistics, while those for the 8.86-MeV distribution are dominated by the uncertainty in the background correction. The proton spectra were unfolded using the excitation energies listed by Hinds and Middleton (1959) for the states in this excitation-energy region. The difficulties in this unfolding process for the weak 8.86-MeV state can be seen in the

spectra in Figure 42. The absolute normalization was deduced from the measured energy loss of the incident particles in the target material assuming that the material was CaF_2. Energy losses in the CaF_2 were measured at 90^o and at 140^o in the elastic scattering of the incident particles on the carbon backing as described in Section C of Chapter II. The uncertainties in the measurements add an additional uncertainty of about 10% to the absolute normalization of the distributions in Figure 46. The distribution for the 9.14-MeV state clearly requires L = 0. The experimental distribution for the 8.86-MeV state has apparently been distorted at the forward angles by its proximity to the strongly forward-peaked 8.768-MeV state and by the relatively high background. In particular, the two points of the distribution at angles less than 8^o appear to be unusually high. The distribution is reasonably well fitted only by L = 2, although the theory does not explain the forward-peaked part of the distribution; it is probable that the discrepancy is experimental in origin. Because the theoretical DWBA distribution did not fit the L = 2 distribution for the 8.86-MeV state very well, particular as to the position of the maximum at 40^o, the distribution was examined with a PWBA theory, also (see Appendix IV). With a cut-off radius of 4.75f the theory clearly identifies both the L = 0 and the L = 2 distributions.

The angular distributions from the $^{22}Ne(^3He, \alpha)$ reaction were taken at an incident energy of 12 MeV (an effective energy of 11.86 MeV after correcting for energy losses in the entrance foil and the target gas), and these distributions are shown in Figure 47. The error bars arise mainly from counting statistics and from uncertainties in the background correction. A further uncertainty of about 20% in the absolute normalization arises from the uncertainties in the gas pressure and the effective volume correction. The distributions for

the states at 9.14 and 9.96 MeV are assigned $\ell_n = 0$ and $\ell_n = 1$, respectively, on the basis of the good agreement of the theoretical distributions with the experimental distributions. The distributions for the states at 10.60 and 10.90 MeV are assigned $\ell_n = 2$ and $\ell_n = 1$ or 2, respectively, but these assignments are tentative because the distributions for these states show only a weak variation with angle and because both of these states may be unresolved doublets.

The distribution for the 8.86-MeV state has its maximum at an angle which corresponds best to an $\ell_n = 1$ distribution, but the distribution is distinctly broader than the $\ell_n = 1$ distribution for the 9.96-MeV state. Even though an assignment of $\ell_n = 1$ is favored for the 8.86-MeV distribution, an assignment of $\ell_n = 2$ cannot be excluded, because the shape and width of the distribution is so different from those of the $\ell_n = 1$ distribution for the 9.96-MeV state.

The results of the analysis of the angular distributions are summarized in Table XIII.

4. Width measurements

The results of the $^{19}F(^3He, p)$ reaction place upper limits on the widths of the states at 8.86 and 9.14-MeV states of 40 keV and 25 keV, respectively. The poorer-resolution data from the $^{22}Ne(^3He, \alpha)$ reaction limit the width of the 9.96-MeV state to about 60 keV and the states at 10.60 and 10.90 MeV to about 80 keV.

5. Conclusions

In view of the distinctive nature of the $^{22}Ne(^3He, \alpha)$ reaction in the excitation region where the T = 3/2 states are expected, the states, beginning at an excitation energy of 8.86 MeV, whose cross-

sections were so large are considered to be T = 3/2 states. The strongly selective nature of the (^{3}He, α) reaction for T = 3/2 states was already noted in ^{13}C and ^{17}O, and it provides strong evidence for the T = 3/2 assignment in this case. The agreement of the excitation energy of the 8.86-MeV state with the predicted value for the lowest T = 3/2 state and the excellent agreement of the relative excitation energies of the other states with those of the known excited states of ^{21}F serve further to confirm the assignment of T = 3/2 to these states. Finally, the close agreement of the relative cross-sections of the ^{19}F(^{3}He, p) reaction to the two lowest "T = 3/2 states" of ^{21}Ne with the analogous cross-sections of the ^{19}F(t, p) reaction to the two lowest states of ^{21}F indicates an assignment of T = 3/2 to the ^{21}Ne states. For these reasons, the five states in ^{21}Ne listed in Table XIII are assigned T = 3/2.

With this assignment, the L-values for the ^{19}F(^{3}He, p) angular distributions to these states can be interpreted as the transfer of a (T = 1, S = 0) "excited deuteron", and j-values can be deduced from the adopted L-values (see Appendix IV). The conclusions drawn concerning the spins and parities of the T = 3/2 states in ^{21}Ne are listed in Table XIII. The fact that the ℓ-values must be the same for the two reactions leading to the same T = 3/2 state requires that $\ell_n = 2$ for the 8.86-MeV state. The large shift to smaller angles of the $\ell_n = 2$ distribution for this state might be interpreted as the same sort of j-dependence effect noticed in the (^{3}He, α) distributions to states of ^{15}O and ^{17}O. If this is the case, since the lowest T = 3/2 state in ^{21}Ne is expected to have $J^\pi = 5/2^+$, it is interesting to note that the distribution is shifted toward smaller angles, when in fact the $\ell_n = 2$ distributions for the two $5/2^+$ bound states of ^{15}O were shifted to larger angles.

The results of the $^{19}F(^{3}He, p)$ measurements can be compared with the work of McDonald and Adelberger (1968) with the $^{19}F(^{3}He, n)$ reaction. They observed a strong L = 0 transition to a state at 9.221 MeV and a very weak transition to a state at 8.990 MeV; both states were identified as T = 3/2 states, and no other narrow states were observed. The results of the $^{19}F(t, p)$, $^{19}F(^{3}He,p)$, and the $^{19}F(^{3}He, n)$ reactions to the two lowest T = 3/2 states in mass-21 are strikingly similar and reflect the expected isospin symmetry in this group of reactions.

The T = 3/2 states at 8.86, 9.14, and 9.96 MeV have also been observed by Butler et al. (1968) in the $^{22}Ne(d, t)$ reaction, and their values for the excitation energies differ significantly (Table XIII) from the values of either this work or that of Hinds and Middleton (1959). There is good agreement, however, on the spins and parities of the states.

V. CONCLUSIONS

A. J-dependence in Angular Distributions

There is rather impressive evidence that the angular distribution of the outgoing particles in a wide variety of direct reactions depends on the total angular momentum, J, of the final state as well as on the transferred orbital angular momentum, ℓ. A summary of the more recent evidence for these effects is given by Glashausser and Rickey (1967). For a given ℓ-value, the distributions for the lower j-value often reach their first maximum at a more forward angle and decrease more abruptly from this maximum than the distributions for the higher j-value. In addition, the cross-section at back angles relative to the forward-angle cross-section is often significantly different for the two distributions. Even when there is no apparent phase difference between the two distributions, the variations with angle for the lower j-value distributions are often much more pronounced than for the higher j-value distributions. These j-dependence effects appear to depend rather strongly on the incident energy; the effects often largely disappear at certain incident energies, particularly at high incident energies.

Glashausser and Rickey found little strong evidence for j-dependence in the two lowest $\ell_n = 1$ distributions measured in the $^{12}C(p, d)^{11}C$ reaction at an incident energy of 27.5 MeV, but there were noticeable effects in the two lowest $\ell_n = 2$ distributions measured in the $^{32}S(p, d)^{31}S$ reaction at an incident energy of 28 MeV. Of these $\ell_n = 2$ distributions, the $3/2^+$ distribution rose to the forward maximum at a smaller angle, decreased more abruptly, and had more structure than the $5/2^+$ distribution. Angular distributions with $\ell_n = 3$ measured

in the $^{56}Fe(He,\alpha)^{55}Fe$ reaction at incident energies of 30 and 40 MeV were fairly structureless, but there were noticeable phase differences between the $5/2^-$ and $7/2^-$ distributions.

Measurements of the two lowest $\ell_n = 1$ distributions seen in the $^{16}O(^3He,\alpha)^{15}O$ reaction at an incident energy of 18 MeV have been reported recently (Max-Planck Institut für Kernphysik 1966). The results indicate that the $1/2^-$ distribution rises to its forward maxima at smaller angles and shows more structure than the $3/2^-$ distribution.

The j-dependence effects noted previously in this work in the $\ell_n = 2$ distributions and in the $\ell_n = 1$ distributions for the $^{16}O(^3He,\alpha)^{15}O$ reaction appear to agree with the results summarized above for other reactions. In both cases, the lower j-value distributions reach their first and second maxima before the corresponding higher j-value distributions. Because the data for these reactions cover a limited angle range (less than 100^o), no conclusion can be drawn about the behavior of the distributions at back angles. There appears also to be no unambiguous conclusion to be drawn from these data about the large-angle structure of the distributions. For example, the two $5/2^+$, $\ell_n = 2$ distributions for ^{15}O (Figure 11), which are both shifted from the theoretical prediction by about the same amount, exhibit very different structures, particularly as concerns the 2^{nd} maximum near 65^o. The 2^{nd} and 3^{rd} maxima of the two $\ell_n = 1$ distributions from the $^{16}O(^3He,\alpha)^{15}O$ reaction (Figure 9) are shifted slightly to lower angles for the $1/2^-$ distribution and to higher angles for the $3/2^+$ distribution, in apparent agreement with the expected effects of j-dependence; the Q-value difference in the two reactions, however, affects the distributions enough that a firm conclusion as to the presence of j-dependence effects cannot be drawn. The two $\ell_n = 1$ distributions for the T = 3/2 distributions in the $^{18}O(^3He,\alpha)^{17}O$

reaction shows an apparent j-dependence (see Figure 39) with the maxima in the distribution for the $1/2^-$ state shifted to smaller angles with respect to those for the $3/2^-$ state. This shift is in agreement with previously noted j-dependence effects.

Finally, the apparent shift to lower angles of the first maximum of the $\ell_n = 2$ distribution for the $^{22}Ne(^3He,\alpha)^{21}Ne$ reaction (Figure 47) might be due in part to a j-dependence effect, but (as noted on page 70), if the state has $J^\pi = 5/2^+$, as is expected for the lowest $T = 3/2$ state, the maximum is shifted in angle in the opposite direction from what would be expected on the basis of the other results. It would be very useful to extend this distribution to larger angles and to measure it at different incident energies in order to understand the shape of the distribution as well as possible. If a $3/2^+$ state could be found at some nearby excitation energy, it would be interesting and useful to compare the two $\ell_n = 2$ distributions in order to see if the observed shift in the $5/2^+$ distribution was in fact a j-dependence effect.

The recent interest in j-dependence effects centers on their usefulness in determining the spins of excited states. Glashausser and Rickey (1967), however, were not able to explain adequately the effects which they observed, and, until the mechanism responsible for j-dependence is better understood, spin assignments based on j-dependence effects should be regarded as tentative. In some cases where many transitions have been experimentally well studied, spin assignments based on j-dependence effects may be considered as more reliable. It is hoped that further study of j-dependence effects such as noted in this work will help to make j-dependence a useful empirical spectroscopic tool, although the "wrong-way" shift of the ^{21}Ne, $5/2^+$, angular distribution is a warning that purely empirical rules should be treated with great caution.

B. Quadratic Mass Equation

The general quadratic mass equation discussed in Section A of Chapter IV can be tested with the now completed mass-13, mass-17, and mass-21 quartets. For these quartets, the masses of the proton-rich end members have been measured, though not with a precision comparable to that achieved for the other members of the quartet. Because of the large uncertainty in the mass of the proton-rich end member, the mass equation is normally used to predict this mass from the three other masses, and this prediction is then compared directly with the experimental measurement. The quadratic mass equation predicts for a T = 3/2 quartet that:

$$M(\tfrac{3}{2}, \tfrac{3}{2}) = M(\tfrac{3}{2}, -\tfrac{3}{2}) + 3\,[\,M(\tfrac{3}{2}, \tfrac{1}{2}) - M(\tfrac{3}{2}, -\tfrac{1}{2})\,]\,. \qquad (25)$$

The predictions from this formula are compared in Table XIV with the masses for the ground states of ^{13}O, ^{17}Ne, and ^{21}Mg and the 1st excited state of ^{21}Mg. The mass table values of Mattauch, Thiele, and Wapstra (1965) were used for most of the ground state masses; the results of this work were used for the T = 3/2 states in ^{13}C, ^{17}O, and ^{21}Ne. The sources for the remaining masses were: ^{13}N and ^{17}F (Adelberger 1967); ^{21}Na (McDonald et al. 1968); ^{21}F (Horvat 1964 and Hinds et al. 1962); ^{13}O (Cerny et al. 1966); ^{17}Ne (Esterlund et al. 1967); and ^{21}Mg (Butler et al. 1967).

The results show agreement for ^{13}O and ^{17}Ne, but the predictions for ^{21}Mg are significantly outside the experimental uncertainties, and a deviation from the mass equation is indicated. Because the quadratic equation is only a first-order approximation, it is necessary to see if these deviations exceed the deviations which

might reasonably be expected from the next order in the approximation. This is most easily done by finding the coefficients in the fit of a cubic equation (with a dT_z^3 term), as deviations from the quadratic equation are expected to be such that $|d/c| \lesssim \bar{Z}\alpha$, where $\bar{Z}$ is the average value of Z in the multiplet and α is the fine-structure constant. It is seen in the last two columns of Table XIV that the deviations for the mass-21 quartet are indeed significantly larger than expected. As a comparison, the results for the mass-9 quartet (Barnes et al. 1967) are included in the table. All of the members of this quartet have been measured with comparable and fairly high precision, and, while this quartet also shows a deviation from the equation, the deviation is well within the range of expected deviations from the quadratic equation.

The masses of the ground state and the 1st excited state of ^{21}Mg were measured (Butler et al. 1968) in the ^{24}Mg(^{3}He, ^{6}He)^{21}Mg reaction. The measurement was particularly difficult because of the very small cross-section for this reaction, and, in addition, the negative Q-value for this reaction necessitated the use of a high incident energy. The experimental resolution was consequently not very high. The T = 3/2 states of ^{21}Ne were measured as described in the same report, in the ^{22}Ne(d, t)^{21}Ne reaction with the same apparatus used for the ^{21}Mg measurements. The cross-sections were reasonably large in this reaction, and these excitation-energy measurements had the additional advantage of including the ground state and assorted lower excited states, all of whose Q-values are rather accurately known, which could be used as calibrations. The reported excitation energies for the T = 3/2 states in ^{21}Ne are systematically higher, differing by about twice the quoted probable errors, than the values of both the present work and the work of Hinds and Middleton (1959); these values are listed in Table XIII. This suggests that the measure-

ment of ^{21}Mg, with the very small cross-section and with no nearby calibration, could be in error by considerably more than the quoted uncertainty. In particular, the nearly identical deviations from the quadratic mass equation for both the mass-21 quartets suggest a systematic error in the ^{21}Mg measurements, and it would be very useful if these measurements could be repeated. The measurements of the other masses of the quartet were of inherently higher precision, and all of these measurements have been checked by different reactions and/or different experimenters. Until further measurements on the ^{21}Mg mass are made, no clear conclusion can be drawn concerning "large" deviations from the quadratic mass equation, but it is clear from the mass-9 results that "small" deviations from the equation must be expected.

C. Extending the Study of T = 3/2 States

It would appear from the present work that, as A increases, the (^{3}He, p) reaction may become less useful for identifying T = 3/2 states directly. This trend is suggested by the ^{15}N(^{3}He, p)^{17}O spectrum shown in Figure 37 where some T = 1/2 states were noted and is indicated especially by the ^{19}F(^{3}He, p)^{21}Ne spectrum shown in Figure 42 where numerous narrow T = 1/2 states are excited in the region of the T = 3/2 states, masking the identity of the T = 3/2 states. One reason appears to be that as A increases, the T = 3/2 states lie at lower excitation energies; nearby T = 1/2 states then have smaller widths because they are less unstable to particle emission. In addition, the (^{3}He, p) reaction is able to excite many of these narrow T = 1/2 states making it difficult to identify the T = 3/2 states simply on the basis of cross-sections. The (^{3}He, α) reaction has proven to

be much more selective, and it is expected that it will continue to accentuate the difference between T = 1/2 and T = 3/2 states in much higher mass nuclei than will the (^{3}He, p) reaction. Eventually, with both reactions, there will have to be a much more detailed comparison of the results of the reactions with the results of the mirror (t, p) and (t, α) reactions which lead to the $T_z = -3/2$ nuclei in order to make T assignments.

The predictions of the approximate mass equation (derived in Section A of Chapter IV), which was used to predict the mass M(3/2, -1/2) from the known mass M(3/2, -3/2), differed from the measured values for the lowest T = 3/2 states in ^{13}C, ^{17}O, and ^{21}Ne by 52, -80, and -60 keV, respectively. This equation can apparently predict the mass of an unknown T = 3/2 state to better than 100 keV and should be useful in limiting the number of candidates for T = 3/2 assignments in future work.

The Coulomb barrier will eventually be a limiting factor in this search for T = 3/2 states. In order to have reasonable cross-sections, higher incident energies will be necessary. This higher energy will produce more energetic outgoing particles and will, consequently, often result in data with poorer energy resolution, and it may not be possible to resolve the various excited states of interest. It might be hoped that, because of the required higher incident energies, the reaction mechanisms would become more selective in isospin as a compensation for the poorer energy-resolution data.

Much of the initial work on locating T = 3/2 states in light nuclei has been completed; many T = 3/2 states have been identified, their excitation energies have been measured, and spin and parity assignments have been made to a large number of these new states. Since most of these states can emit heavy particles through isospin-

nonconserving channels only, a comparison of the γ-decay modes (isospin allowed) of the states with their particle-decay modes should reveal much concerning the isospin purity and structure of these states.

A study by Adelberger et al.(1968) on some of the particle-decay modes of the lowest T = 3/2 states in ^{13}C and ^{13}N has already indicated an apparent isospin asymmetry in the heavy-particle decay of these two states. The present author is currently participating in a study of further particle-decay modes and the γ-decay modes of the ^{13}C T = 3/2 state to clarify the nature of this asymmetry. Higher isospin states are also being studied as compound-nuclear resonances in reactions which are isospin forbidden in at least the incoming channel.

From all of these studies it is hoped that it will become possible to understand much of the structure of the T = 3/2 states.

APPENDIX I

PROBABLE ERRORS IN Q-VALUES DETERMINED FROM RELATIVE MEASUREMENTS

The purpose of this appendix is to present a method for deriving a set of nuclear reaction Q-values relative to another set of nuclear reaction Q-values from one set of data covering all the reactions. The error in the final set of Q-values will be discussed in some detail, and estimates will be made of the probable errors in these Q-values arising from uncertainties in the experimental data and from uncertainties in the Q-values of the reactions used for the calibration.

A fully relativistic equation $G_i(E_1, E_{3i}, \theta)$ to calculate the Q-value Q_i will be discussed in Appendix II. The explicit variables in this equation are: E_1, the incident energy; E_3, the energy of the detected outgoing particle; and θ, the reaction angle. The subscript i on the function and on E_3 identify the particular reaction; there is no subscript on E_1 because it is the same for all reactions to be compared. There is an implicit dependence on the target thickness T, on the spectrometer calibration constant K, and on the N. M. R. frequency F for the detected particle group. Both the incident energy and outgoing energy must be corrected for energy losses in the target, and E_3 depends on K and F in the following way (non-relativistic):

$$E_3 = K \frac{Z^2}{M} M_p F^2 .$$

Since the incident energy is common to all of the reactions, all of these calculations of Q-values relative to calibration-reaction

Q-values first derive the incident energy using the calibration-reaction data and then use that incident energy to derive Q-values using the other reaction data. With a known Q-value, Q_i, an incident energy E_1 is found such that $Q_i = G_i(E_1, E_{3i}, \theta)$, and the desired Q-value, Q_j is then taken to be equal to $G_j(E_1, E_{3j}, \theta)$. If there are several calibration reactions, E_1 is taken as the weighted average of the values derived from the different calibration-reaction data. The basis for this weighting will be discussed shortly.

In order to discuss both the "true" errors and the probable errors in a calculated Q-value, it will be assumed that the experimentally measured value (primed) of a quantity X differs from the "true" value (unprimed) by only a small amount:

$$\delta X = X' - X$$

where δX is the error in X', the measured value of X. With this notation, the first step of the Q-value calculation (outlined above) is to derive E_1' from the i^{th} reaction data--$Q_i' = G_i(E_1', E_{3i}', \theta')$--and Q_j' is then defined to be $G_j(E_1', E_{3j}', \theta')$. What is of interest, of course, is the error in Q_j'.

$$\delta Q_j = Q_j' - Q_j = G_j(E_1', E_{3j}', \theta') - G_j(E_1, E_{3j}, \theta)$$

$$= \frac{\partial G_j}{\partial E_1}(\delta E_1 + \frac{\partial E_1}{\partial T_j}\delta T) + \frac{\partial G_j}{\partial E_3}\left(\frac{\partial E_{3j}}{\partial F}\delta F_j + \frac{\partial E_{3j}}{\partial K}\delta K + \frac{\partial E_{3j}}{\partial T}\delta T_j\right)$$

$$+ \frac{\partial G_j}{\partial \theta}\delta\theta ,$$

where T, K, and F are defined on the previous page. A similar equation can be written for δQ_i, and the equation can be solved for δE_1. When δE_1 is substituted for in the equation for δQ_j, the error in Q_j' becomes:

$$\delta Q_j = \rho \delta Q_i + \frac{\partial G_j}{\partial E_1}\left[\frac{\partial E_1}{\partial T}\delta T_j - \frac{\partial E_1}{\partial T}\delta T_i\right] + \left[\frac{\partial G_j}{\partial E_3}\frac{\partial E_{3j}}{\partial F}\delta F_j - \rho \frac{\partial G_i}{\partial E_3}\frac{\partial E_{3i}}{\partial F}\delta F_i\right]$$

$$+ \left[\frac{\partial G_j}{\partial E_3}\frac{\partial E_{3j}}{\partial K} - \rho \frac{\partial G_i}{\partial E_3}\frac{\partial E_{3i}}{\partial K}\right]\delta K + \left[\frac{\partial G_j}{\partial E_3}\frac{\partial E_{3j}}{\partial T}\delta T_j - \rho \frac{\partial G_i}{\partial E_3}\frac{\partial E_{3i}}{\partial T}\delta T_i\right]$$

$$+ \left[\frac{\partial G_j}{\partial \theta} - \rho \frac{\partial G_i}{\partial \theta}\right]\delta\theta$$

$$\rho = \frac{\partial G_j}{\partial E_1}\left(\frac{\partial G_i}{\partial E_1}\right)^{-1} .$$

The partial derivatives of G are given as:

$$\frac{\partial G}{\partial E_1} = -1 + \frac{M_1}{M_4}\left(1 - \sqrt{\frac{M_3 E_3}{M_1 E_1}}\cos\theta\right)$$

$$\frac{\partial G}{\partial E_3} = 1 + \frac{M_3}{M_4}\left(1 - \sqrt{\frac{M_1 E_1}{M_3 E_3}}\cos\theta\right)$$

$$\frac{\partial G}{\partial \theta} = \frac{2\sqrt{M_1 M_3 E_1 E_3}}{M_4}\sin\theta .$$

In the following discussion, ΔX is the probable error in the measurement of X and is hopefully a realistic assessment of δX, the true error. For most of the reactions studied in the present work, $\partial G/\partial E_3$ and $\partial G/\partial E_1$ were not very different for the various reactions and will be assumed, for the sake of simplicity, to be independent of the reaction considered; this implies $\rho = 1$. With this assumption, the various contributions to the error in a Q-value will be examined in some detail.

Calibration-reaction error: $\rho\delta Q_i$.

This term reflects the desirability of finding calibration reactions with as precisely known Q-values as possible. In most of the measurements of the present work, ρ was close to 1, and the probable error in a derived Q-value could obviously not be less than ΔQ_i. A way to reduce significantly this contribution to the probable error is to include as many calibration reactions with well-measured Q-values as possible or to pick reactions with $\delta Q = 0$. This error is identically zero when only the difference between two Q-value is determined -- generally for the same reaction. For elastic scattering reactions, $\delta Q = 0$, and, if the scattering is on the same target material used by the reaction to be examined, this method of calibration can be very useful.

One must exercise care in using calibration reactions leading to excited states; these different reactions may have a systematic error in their Q-values, if the excitation energies were measured relative to the energy of the ground state, since any error in the ground-state Q-value carries over into all of the excited-state Q-values.

Target-thickness (incident) error: $\frac{\partial G_j}{\partial E_1}\left\{\frac{\partial E_1}{\partial T}\delta T_j - \frac{\partial E_1}{\partial T}\delta T_i\right\}$.

If the reactions to be compared use the same material in the target or, when different materials are used (e. g., in reactions on the ^{16}O and ^{18}O in a NiO target), if the different materials have the same average distribution in the target, then $\frac{\partial E_1}{\partial T_i}\delta T_i = \frac{\partial E_1}{\partial T_j}\delta T_j$, and this contribution to the probable error vanishes identically, regardless of any uncertainty in the measurement of the target thickness. All of the measurements of this work were assumed to satisfy this requirement on the distribution of the target materials, and this source of error in a Q-value was consequently neglected.

In the case of tantalum-backed boron targets, only the exposed boron surface can oxidize, and the average distributions of the oxygen and the boron in the target are not the same. Regardless of how well the target thickness is determined, these distributions of the materials in the target must be known in order to calculate correctly a Q-value relative to a Q-value for a reaction on the other target material. Because of the difficulties in accurately measuring the distributions of different materials in a target, such cases were not included in the measurements of the present study.

Target-thickness (exiting) error: $\left[\frac{\partial G_j}{\partial E_3}\frac{\partial E_3}{\partial T}\delta T_j - \rho\frac{\partial G_i}{\partial E_3}\frac{\partial E_{3i}}{\partial T}\delta T_i\right]$.

Assuming that the same target-thickness correction is to be made for all of the reactions (see above), this term is approximately equal to $\frac{1}{2}\frac{\partial G}{\partial E_3}\left[\text{loss}_j - \text{loss}_i\right]\frac{\delta T}{T}$ where "loss" is the energy loss of the exiting particle in traversing the entire target. The probable error in the Q-value from the target correction can be reduced by: (1) using very thin targets so that the energy loss in the target is small; (2) comparing reaction for which the respective reaction particles have comparable

energy losses in the target so that there is the maximum cancellation in the error term; (3) determining the target thickness as well as possible so that $\Delta T/T$ is small.

In the present study, thin targets were used, and the probable error in the target thickness was typically 10% or less. Consequently, even when comparing reactions emitting protons to those emitting α particles, the contribution to the probable error in a Q-value arising from the target correction was less than 2 keV and was typically less than 0.3 keV when there was any significant cancellation in the error term.

$$\text{Spectrometer-calibration error: } \left[\frac{\partial G_j}{\partial E_3} \frac{\partial E_{3j}}{\partial K} - \rho \frac{\partial G_i}{\partial E_3} \frac{\partial E_{3i}}{\partial K} \right] \delta K.$$

This term is given approximately by $\frac{\partial G}{\partial E_3} [E_{3j} - E_{3i}] \frac{\delta K}{K}$ since $\frac{\partial E_3}{\partial K} = \frac{E_3}{K}$.

The spectrometer was calibrated with a ^{212}Po α source (8.785 MeV) in the position of the beam spot on the target; this α group was focused on the center of counter 8 at an N. M. R. frequency of about 27703 kHz, and these spectrometer-calibration measurements tended to vary by less than 2 kHz. The spectrometer calibration for nuclear reactions depends critically on the correct vertical position of the beam spot, as an error of 0.01 inch in this position can change the calibration by 2.8 kHz. Since the beam spot was typically a square 0.06 inches high, fluctuations in the beam-current density across the spot, variations in the target thickness, or an error in the position of the beam-defining slits could possibly change the calibration by as much as 3 kHz. The calibration frequency was, therefore, assumed to be 27703 $\pm$ 4 kHz, and this implies that $\Delta K/K \tilde{=} 2 \times 4/27703 = 3 \times 10^{-4}$.

The spectrometer-calibration error term is obviously smallest when the particle-energy difference is small. If the spectrometer has been properly cycled, the probable error in the calibration should be approximately 3×10^{-4}; consequently, even for an energy difference as large as 5 MeV, the probable contribution to the error in the Q-value should only be about 2 keV, and, for energy differences of 1 MeV, the probable error from this term should be a small fraction of 1 keV. A method used in the present study for minimizing the error in K will be discussed later.

Angle error: $\left[\frac{\partial G_j}{\partial \theta} - \rho \frac{\partial G_i}{\partial \theta} \right] \delta\theta$.

This term is approximately equal to $2\sqrt{M_1 E_1}\left[\frac{\sqrt{M_{3j} E_{3j}}}{M_{4j}} - \frac{\sqrt{M_{3i} E_{3i}}}{M_{4i}} \right] \sin\theta \, \delta\theta$

or $2\sqrt{K M_p M_1 E_1} \left[\frac{Z_{3j} F_j}{M_{4j}} - \frac{Z_{3i} F_i}{M_{4i}} \right] \sin\theta \, \delta\theta$ where the last form follows from the relation between E_3 and F. There is the most internal cancellation in this term for similar reactions with a small particle-energy difference; the cancellation was least in the present study for α-emitting reactions compared to proton-emitting reactions.

The spectrometer is positioned with reference to a large protractor fixed to the floor under the spectrometer. The protractor is graduated in degrees, and there is an accompanying vernier which is graduated in tenths of a degree. With care, one can reproducibly position the spectrometer to about 0.02°. The zero of the scale was established by measuring the angle setting at which the incident beam passed directly into the spectrometer, and the uncertainty in this measurement was less than 0.05°.

Besides the possible errors in the protractor settings, the reaction angle can be significantly affected by: (1) the position of the

beam spot on the target with respect to the center of the scattering chamber; (2) the positioning of the two theta-defining slits in the spectrometer; (3) and the variation of the reaction yield across the theta opening. The beam spot might not be centered chiefly because the target holder can be misaligned and because the target (especially self-supporting targets) can be displaced from center due to the thickness of the target frame. As the thickness of the target frames was always 0.01 inches or less and as the misalignment of the target holder appeared to be less than the thickness of the target frame -- roughly established by rotating the target rod and watching the position, with respect to the line of sight up the beam tube, of the supposedly centered, target-holder surface -- a reasonable upper limit on the distance the beam spot might be off-center appeared to be 0.015 inches. Since the angle-defining slits are 14 inches away from the center of the scattering chamber, this suggests a maximum probable error from this source of $\frac{0.015 \times 57.3}{14} = 0.06^{o}$. The theta-defining slits were always opened symmetrically from the settings used for the determination of the zero of the protractor scale, and the uncertainties in these settings were assumed to be negligible.

Because the reaction yield can vary significantly across even the small theta opening of the spectrometer, it is necessary to see how this variation can affect the Q-value. The non-relativistic equation for the Q-value depends on θ through a linear term in $\cos\theta$ only, and the average value of $\cos\theta$, weighted by the yield, should be used in the Q-value determination. Assume that, over a small angular spread, the yield is linear in the angle: $Y(\theta) = a + b\theta$ and that the theta opening is centered at θ with a width of 2ϵ .

$$\langle \cos\theta \rangle = \frac{\int_{\theta-\epsilon}^{\theta+\epsilon} (a + b\theta)\cos\theta \, d\theta}{\int_{\theta-\epsilon}^{\theta+\epsilon} (a + b\theta) d\theta} = \frac{\cos\theta \sin\epsilon}{\epsilon} + \frac{b \sin\theta}{a+b\theta} \frac{(\epsilon \cos\epsilon - \sin\epsilon)}{\epsilon} .$$

The first term results from a constant yield across the finite opening, and this value for the average value of $\cos\theta$ was used in the Q-value calculations -- this correction is discussed from a slightly different point of view in the next appendix. If the 2^{nd} term is expanded in powers of ϵ,

$$2^{nd} \text{ term} = \frac{-b \sin\theta}{a + b\theta} \left[\frac{\epsilon^2}{6} + O(\epsilon^4) \right] \approx \frac{-(Y_2 - Y_1)}{Y_2 + Y_1} \frac{\epsilon}{6} \sin\theta$$

where Y_1 and Y_2 are the reaction yields at the ends of the theta opening. This term implies a correction to the angle of

$$\delta\theta = \frac{Y_2 - Y_1}{Y_2 + Y_1} \frac{\epsilon}{6}$$

where ϵ is in radians.

The theta slits were usually opened to a full opening of 1^o to 1.5^o -- the gas target data were taken with an opening of about 2^o. The reaction which probably would have required the largest yield-variation correction to the angle was the $^{16}O(^3He, \alpha)$ reaction to the 3^{rd} excited state of ^{15}O at 6.17 MeV (see Figure 9). At about 20^o, the percentage change in the yield over the 1^o full opening was about 10%, and this gives an angle correction of

$$\delta\theta = \frac{0.1}{2} \frac{0.5^o}{6} = 0.004^o$$

and, since $\frac{\partial Q}{\partial \theta}$ ($\theta = 20^{o}$) $\approx$ 28 keV/degree, this leaves an error in the Q-value of

$$\delta Q \approx 0.11 \text{ keV} .$$

Since usually the percentage change in the yield across the theta opening was considerably smaller than 10% or was of this order of magnitude only at forward angles, where $\partial Q/\partial \theta$ is small, the error involved in neglecting the yield variation should have been very small and was neglected in the present study. The theta opening for the gas-target measurements was about twice as large, but the error incurred in neglecting the yield variation was still assumed to be negligibly small compared to the other uncertainties.

The systematic probable error in the reaction angle could be as large as 0.07^{o} from the combination of the target-position error and the protractor-zero error, but actual results of reaction measurements seem to indicate that the systematic error was probably much smaller. At the same time, these results confirm a random probable error which is of the order of 0.02^{o}; thus, an overall probable error of about 0.05^{o} in the reaction angle seems to be a reasonable assumption. Since many of the reactions which were compared -- particularly in the ^{15}O energy measurements -- produced significant cancellations in the error term, the contribution of the angle-error term to those Q-value measurements was very small.

N. M. R.-frequency error: $\left[\frac{\partial G_j}{\partial E_3} \frac{\partial E_3}{\partial F} \delta F_j - \frac{\partial G_i}{\partial E_3} \frac{\partial E_{3i}}{\partial F} \delta F_i \right]$.

This term arises mainly from the uncertainty in the precise shape of the particle group; the method used for analyzing the peaks and assessing the probable error in the frequencies is discussed in Section

A of Chapter II. This uncertainty arises largely from counting statistics and from the combining of data from different counters in the array. The N. M. R. frequencies of most of the groups studied in the present work were uncertain to less than 5 kHz, and this includes an uncertainty of about 2 kHz in the measurement of the N. M. R. - frequency setting for the counter array. When very close attention was given to the N. M. R. -frequency determination, the variation in the results of the measurements indicated, generally, a probable error of no more than 3 kHz, since the frequency position of a peak could normally be reproduced to 2 kHz.

This error term cannot really have much internal cancellation because δF_i and δF_j are independent random errors. If there is some part of these errors which is systematic -- if the particle groups were analyzed in some incorrect but consistent manner -- then this systematic part of the error could largely cancel out for small particle-energy differences.

The errors in the target correction and spectrometer calibration do not average out in a series of measurements because these errors depend, roughly, on an $(E_j - E_i)$ factor, and this factor usually does not change sign in a set of measurements. One way of partially cancelling the effect of these errors is to find a set of calibration reactions whose particle energies bracket those of the reactions of interest, for, in that case, the errors make a more random contribution to the error in the Q-value. The probable error in T was estimated according to the way in which T had been measured (see Section C of Chapter II). There were two ways of assessing and reducing the probable error in K:

(1) The derived value of E_1 was compared to the value of E_1 expected from the field setting of the 90^o beam-analyzing magnet. If these values differed significantly, K was changed, if possible, so

as to reduce the difference.

(2) With several calibration reactions, K was varied slightly so as to give the best agreement, in a least squares sense, for the various values of E_1.

With K adjusted in this manner, the square of the probable error in E_1 was taken to be:

$$\Delta^2 E_1 \equiv \left(\frac{\partial G}{\partial E_1}\right)^{-2} \left[\Delta^2 Q + \left(\frac{\partial G}{\partial E_3}\right)^2 \left(\frac{\partial E_3}{\partial F}\right)^2 \Delta^2 F\right]$$

$$+ \left[\left(\frac{\partial E_1}{\partial T}\right)^2 + \left(\frac{\partial G}{\partial E_1}\right)^{-2} \left(\frac{\partial G}{\partial E_3}\right)^2 \left(\frac{\partial E_3}{\partial T}\right)^2\right] \Delta^2 T \,.$$

Note that the dependence on K has been left out of this equation. The value of E_1 used in the final Q-value determination was then:

$$E_1 = \Sigma\, w_i E_{1i} / \Sigma\, w_i \qquad\qquad \Delta E_1 = (\Sigma\, w_i)^{-1/2}$$

where $w_i = 1/\Delta^2 E_{1i}$ and ΔE_1 is roughly the internal error in E_1. When several calibration reactions were used, it was always the case that the external error in E_1 was less than this internal error.

A lower limit on the square of the probable error in the derived Q-value was taken to be:

$$\Delta^2 Q = \left[\frac{\partial G}{\partial E_1} \Delta E_1\right]^2 + \left[\frac{\partial G}{\partial E_3} \frac{\partial E_3}{\partial F} \Delta F\right]^2 .$$

This probable error was assumed to be representative of the true error because the major contribution to the uncertainty in a single Q-value determination arises chiefly from the uncertainty in the particle-group frequency for that particular reaction -- the 2nd term above. The first term, which reflects the uncertainty in the calibration, was generally smaller. Thus, when comparing several derived values (i. e., at different angles) for a Q-value, this probable error could be used in the weighting of the various values since it represented principally the uncertainty in the particle-group frequency -- usually the major uncertainty -- and not the uncertainty in the calibration.

This probable error may be too small for a single Q-value determination because the systematic contributions of the target error, spectrometer-calibration error, and the calibration-reaction Q-value error have been averaged out; but it may, on the other hand, overestimate the uncertainty in a separation measurement where the systematic errors can largely cancel out. This particular form for the probable error in the final Q-value was chosen partly for its simplicity and partly because it was easy to translate into a computer program. Obviously, a careful re-translation must be made of the result of this probable-error calculation because this estimate of the probable error is, as noted above, better for some measurements or kinds of measurements than for others.

Gas Target Calibration

The calibration of the gas-target data for the $^{22}Ne(^{3}He,\alpha)^{21}Ne$ reaction was performed in a somewhat different manner. The calibration reactions were used, along with the measured value of the gas

pressure and the incident energy (given by the 90^{o} beam-analyzing magnet), to determine the thickness of the entrance and exit windows of the gas cell. The quantity of physical interest is the energy of the incident particles as they traverse the center of the active volume; this quantity is common to all of the measured reactions taking place within the gas target. The aperture system which determined the active volume in the cylindrical gas target was constructed and positioned so that the center of the active volume coincided with the center of the gas target for all the angles which were used. The incident particles always passed through the same nickel window ($\sim$ 6000 Å) and along the same path length in the gas, so that the effective incident energy was the same at all angles and was equal to the beam energy corrected for the energy loss in the nickel entrance window and in the gas up to the center of the gas target. Since the outgoing particles considered included α particles, deuterons, and protons, a reasonably good determination could be made of the 10000-Å (nominal) nickel exit window, because so many significantly different energy losses were associated with these different particles. (The reactions and the respective energy losses in the exit window are given in Table XV.)

The determination of the thicknesses of the two windows was made by fitting (by least squares) the incident energies derived from the reactions to the incident energy indicated by the N. M. R. frequency of the 90^{o} beam analyzing magnet, and the two window thicknesses were varied to give the best fit to this incident energy. The value of 10514 ± 129 Å derived for the exit window agreed well with the nominal value for the nickel foil.

Because of the complexity of the analysis, it was too difficult to derive directly the probable error in the calibration procedure.

Instead the calibration-reaction Q-values were rederived, using the derived window thicknesses, and the probable error in the procedure was estimated from the overall success of reproducing these Q-values. Uncertainties had been assigned to the N. M. R. frequencies for the particle groups in the window-thickness determination, but these uncertainties were ignored in the rederivation, making the agreement between the input values and the derived values not as good as it might have been. In the third column of Table XV are given the deviations of the output values from the input values, and the uncertainty given is just the root-mean-square deviation from the average. On the average it appears that this procedure is good to about 3 keV, and this 3-keV uncertainty was added directly to the statistical uncertainty in the average value of the several measurements of a Q-value in order to give the final uncertainty in the Q-value.

It is interesting that the 1% uncertainty in the thickness of the exit foil means about a 2.5-keV uncertainty in the α-particle energy for the T = 3/2 states in the ^{21}Ne reached with the ^{22}Ne(^{3}He, α) reaction. (The energy losses in the exit window for the various calibration reaction are given in column 4 of Table XV.) And this is well within the 3-keV uncertainty assigned for this calibration procedure.

As a further check of this procedure, data that were taken with ^{20}Ne in the gas target were processed in the same manner as above. There were fewer well-known calibration reactions (Table XVI), but the results are in good agreement with the ^{22}Ne results. The exit window was measured to be 10399 ± 181 Å, and the overall ability of the procedure to reproduce the Q-values was again about 3 keV.

APPENDIX II

RELATIVISTIC KINEMATICS EQUATIONS

Because the 61-cm-radius magnetic spectrometer is capable of precise analysis of protons and α particles up to energies above 20 MeV, it is usually necessary to use fully relativistic equations when dealing with data from the spectrometer.

The fully relativistic equation for a particle with charge Z and momentum P in a magnetic field of strength B is:

$$P = \frac{ZRB}{c}$$

where R is the radius of curvature. The magnetic field in the spectrometer is proportional to the frequency F of an N. M. R. measuring probe, and this proportionality may be used to obtain a relationship between the N. M. R. frequency and the relativistic energy.

$$E_o \equiv \frac{P^2}{2M} = \left(\frac{R^2B^2}{c^2}\right)\frac{Z^2}{2M} = K(1 + \Delta K)\,\frac{Z^2M_p}{M}\,F^2$$

where E_o is the non-relativistic energy, ΔK is a small frequency-dependent correction (McNally 1966) to the proportionality constant K, and the factor Z^2M_p/M has been isolated so that K is the same for all particles. Since $(E + Mc^2)^2 = P^2c^2 + M^2c^4$, the equation for E can be written:

$$E = Mc^2 \left[\left(1 + \frac{2E_o}{Mc^2}\right)^{1/2} - 1 \right] \cong E_o + \frac{1}{2} \frac{E_o^2}{Mc^2} + \frac{1}{2} \frac{E_o^3}{M^2c^4} \quad .$$

The following equations form the basis for relativistic kinematics:

$$P_1 = P_3 \cos\theta + P_4 \cos\phi$$

$$P_3 \sin\theta = P_4 \sin\phi$$

$$W_1 + M_2 = W_3 + W_4$$

$$W^2 = P^2 + M^2 = (E + M)^2$$

where c has been set equal to 1; W, E, and P are the total energy, kinetic energy, and momentum, respectively. The angles θ and ϕ are lab angles, and the rest of the notation is standard. These equations can be solved to give the reaction Q-value:

$$M_4^2 = M_1^2 + M_2^2 + M_3^2 + 2M_2(W_1 - W_3) - 2W_1W_3 + 2P_1P_3 \cos\theta$$

$$Q \equiv M_1 + M_2 - M_3 - M_4$$

$$= M_1 + M_2 - M_3 - \left[M_1^2 + M_2^2 + M_3^2 + 2M_2(W_1 - W_3) - 2W_1W_3 + 2P_1P_3\cos\theta \right]^{\frac{1}{2}}$$

$$= (M_1 + M_2 - M_3)\left[1 - \left(1 + 2\,\frac{E_1(M_2 - M_3) - E_3(M_2 + M_1) - E_1E_3 + P_1P_3\cos\theta}{(M_1 + M_2 - M_3)^2}\right)^{\frac{1}{2}} \right]$$

The solution for E_3 may be written in the following way:

$$E_3 = \frac{M_3 P_1^2 \cos^2\theta - \alpha\beta \pm \cos\theta\, P_1(\beta^2 - 2\alpha\beta M_3 + M_3^2 P_1^2 \cos\theta)^{1/2}}{\alpha^2 - \cos^2\theta\, P_1^2}$$

$$\alpha = E_1 + M_1 + M_2 \qquad \beta = E_1(M_3 - M_2) - Q(\frac{Q}{2} + M_4) \ .$$

Because the equation for M_4^2 is unchanged if the indices 1 and 3 are interchanged and M_2 is set equal to $-M_2$, the equation for E_1 can be gotten from the equation for E_3 by simply interchanging the 1 and 3 indices throughout and replacing M_2 by $-M_2$. Although Q depends on the masses, it is not necessary to worry about how Q would be changed by this transformation because the 2nd term of β can be shown to be independent of this transformation.

(1) Note that M_4 equals the ground state mass of the nucleus plus any excitation energy.

(2) Use the plus sign in the equation for E_3 for the normal solution for E_3. If E_3 is double valued at a certain angle, the minus sign corresponds to the lower energy solution. The corresponding solution(s) for E_1 always uses the opposite sign.

(3) The mass (in MeV) in all these equations was taken to be:

$$M(A, Z) = \text{mass excess} + 931.478A - 0.511006Z$$

where the values for the physical constants were taken from Cohen and DuMond (1964) and where the values for the mass excesses (unless otherwise noted) were taken from the mass tables of Mattauch, Thiele, and Wapstra (1965).

The opening into the spectrometer can cover several square degrees, and the value of the reaction-angle θ varies across this opening. The opening is a rectangle which is $2\Delta\theta$ wide by $2\Delta\phi$ high and centered at θ_s, the angle indicated on the protractor scale for the position of the spectrometer. The following relation holds between the angle θ and the angles θ' and ϕ' which describes a point in the rectangular opening:

$$\cos\theta = \cos\theta' \cos\phi' .$$

The angle ϕ' is measured perpendicularly to the horizontal plane defined by the incident particles and the exiting particles. The angle θ is measured about the vertical axis and is equivalent to the spectrometer angle. The non-relativistic equation for the Q-value can be shown to depend on θ through a linear term in $\cos\theta$ only. Consequently, if the yield of a nuclear reaction is assumed to be constant across the spectrometer openings (see Appendix I), the Q-value for that reaction should be calculated using the value of $\cos\theta$ averaged over the opening:

$$\langle\cos\theta\rangle = \frac{1}{(2\Delta\theta)(2\Delta\phi)} \int_{\theta_s-\Delta\theta}^{\theta_s+\Delta\theta} \int_{-\Delta\phi}^{\Delta\phi} \cos\theta' \cos\phi' \, d\phi' \, d\theta'$$

$$= \cos\theta_s \frac{\sin\Delta\theta}{\Delta\theta} \frac{\sin\Delta\phi}{\Delta\phi} .$$

APPENDIX III

The calculation of yields from data collected with the 16-counter array is fairly involved and subject to some uncertainties. The yield for a particle group measured by a magnetic spectrometer is

$$Y = \int \lambda(F)\, dF \tag{42}$$

where the integral is taken over the particle group and $\lambda(F)$ is the number of counts per unit frequency at each point on the peak. For a counter with an aperture which defines the frequency (momentum) resolution of the system,

$$\lambda(F) = \frac{N(F)}{KF} \tag{43}$$

where KF is the frequency resolution of the aperture and N(F) is the number of detected particles with magnetic rigidity corresponding to the N. M. R. frequency, F. The resolution of the aperture is equal to the frequency multiplied by K, a constant which depends mainly on the size of the aperture and its position in the focal plane (Groce 1963 and McNally 1966).

The data from the counter array consist of the number of particles detected in each of the 16 counters. It is seldom that a particle group is entirely within the momentum span of a single counter, so that there has to be some way of combining all the data into a simple spectrum from which the yields and other information can be obtained directly. To do this, the data from each counter

must be corrected to take into account the different collection efficiencies of the counters, and the N. M. R. frequency for each counter must be determined. The frequency F_i of the i^{th} counter is defined with respect to the N. M. R. frequency setting F_s for the magnetic spectrometer:

$$F_i = F_s X_i \tag{44}$$

where the X_i are measured constants which are independent of frequency (McNally 1966). Because the 8^{th} counter is near the center of the focal plane of the spectrometer, it is customary to calibrate the spectrometer so that $X_8 = 1$. The reciprocal collection efficiencies for the array counters are defined as the ratio of yields measured by counter 8 and the i^{th} counter, where the yield measurements are taken at the same frequency on a spectrum which is linear in the frequency:

$$\epsilon_i \equiv \frac{N_8(F)}{N_i(F)} ,$$

and the number of counts N_i for the i^{th} counter to be combined with the other counter data into the overall spectrum is then:

$$N_i' = N_i \epsilon_i .$$

The reciprocal efficiency factors were found by McNally to be independent of frequency, to the accuracy of his measurements, and a few sets of these factors are given in Table XVII; the uncertainty in the determinations was about 5%.

The reciprocal efficiency factors generally increase from one end of the array to the other, with the exception of the 2nd counter which probably has a smaller active area than the other counters, and this increase can be reasonably well explained by the expected change in resolution from one end of the array to the other. For example, since the 1st counter is at a radius of about 22.4 inches and the 16th counter is at a radius of about 25.8 inches, a difference in resolution from one end of the array to the other of approximately 15% would be expected. This is about the difference that is observed in the factors, though differences in the aperture widths and detector active areas cause slight variations.

By using the previous definition of K, the resolution constants K_i for the several counters can be directly related to the reciprocal efficiency factors.

$$\frac{K_8}{K_i} = \frac{K_8 \, F \, \lambda(F)}{K_i \, F \, \lambda(F)} = \frac{N_8(F)}{N_i(F)} = \epsilon_i$$

$$K_i \, \epsilon_i = K_8 \equiv K$$

where $\lambda(F)$ is a spectrum which is at most linear in F. Since K is a constant, this relation enables one to obtain the yield of a particle group directly from the corrected spectrum.

$$\lambda(F) = \frac{N_i(F)}{K_i F} = \frac{N_i(F) \, \epsilon_i}{K_i \, \epsilon_i \, F} = \frac{N_i'(F)}{K \, F} \, .$$

The reciprocal efficiency factors have cancelled out of the last expression, and the yield becomes

$$Y = \int \lambda(F)\, dF = \int \frac{N'(F)}{K F}\, dF$$

where $N'(F)$ is taken directly from the combined spectrum. In most cases, F changes so little over a narrow peak that it can be considered a constant.

$$Y \simeq \frac{1}{KF} \int N'(F)\, dF = \frac{\text{Area Under Peak}}{KF} .$$

This is the reason for the interest in describing peaks by triangles (see Section A of Chapter II), for the simple formula for the area of a triangle is easy to work with.

APPENDIX IV

Angular distributions from both the (^{3}He, p) and (^{3}He, α) reactions were measured in this work, and a discussion of these reactions is necessary before any conclusions can be drawn from the analysis of the distributions.

The (^{3}He, α) distributions were analyzed assuming that the reaction proceeded by a direct-reaction pick-up of a neutron. The selection rules for this one-step process can be summarized as

$$\Delta\vec{T} = 1/2$$

$$\Delta\pi = (-1)^{\ell}$$

$$s = 1/2$$

$$\Delta\vec{J} = \vec{\ell} + \vec{s}$$

where ℓ is the orbital angular momentum of the transferred neutron. Since the spin of the target was zero ($J_i = 0$) for all of the (^{3}He, α) reactions of this work, the last rule can be simplified to $J_f = \ell \pm 1/2$.

The (^{3}He, p) reaction was assumed to proceed by a direct-reaction stripping of a neutron-proton pair. In order to obtain simple selection rules, it was necessary to assume further that the transferred pair were in their lowest state of relative motion; i.e., in an s-state. Since the s-wave purity of ^{3}He is quite good, this assumption seems reasonable. This point has been discussed in some detail by Adelberger (1967) and by Glendenning (1961). The selection rules can then be divided into two groups depending on whether the transferred pair are in a singlet or triplet isospin state:

$\Delta\vec{T} = 1$	$\Delta\vec{T} = 0$
$\vec{S} = 0$	$\vec{S} = 1$
$\Delta\vec{J} = \vec{L}$	$\Delta J = \vec{L} + \vec{S}$
$\Delta\pi = (-1)^L$	$\Delta\pi = (-1)^L$

where $\vec{S}$ is the spin of the transferred pair and $\vec{L}$ is the total, orbital angular momentum transferred by this pair to the target nucleus.

The $(^3He, p)$ reaction could reach the T = 3/2 states of this study only by transferring one unit of isospin, so that only the selection rules grouped under $\Delta\vec{T} = 1$ will be considered here. Consequently, as soon as a state was established as having T = 3/2, the selection rule $\Delta\vec{J} = \vec{L}$ could be used to limit the possible choices of spin for the state.

The quantum of orbital angular momentum which is transferred in the reaction must be determined before the selection rules can be used to determine the significance of a particular distribution, and a detailed theory of direct-reaction processes is necessary in order to determine this quantum number. In general, it was sufficient to analyze the experimental distributions using simply a DWBA theory, but in two cases it was decided to extend the analysis by including the predictions from a PWBA theory.

The simplest theory of direct reactions uses the Plane Wave Born Approximation (PWBA), and the theory predicts that the dominant contribution to the angular variation (see Banerjee 1960) is

$$\frac{d\sigma}{d\Omega} \propto j_\ell^2 (K R_o)$$

where K is the angular momentum transfer and R_o is an integration cutoff which should be of the order of the sum of the radii of the interacting nuclei. K can be written as the sum of the two center-of-mass momenta,

$$\vec{K} = \vec{K}_{^3He} - \frac{A_T}{A_F}\vec{K}_p \qquad (^3He, p)$$

$$\vec{K} = -\vec{K}_{^3He} + \frac{3}{4}\vec{K}_\alpha \qquad (^3He, \alpha)$$

where A_T and A_F are the mass numbers of the target and final nuclei, respectively.

This very simple form for the angular variation of the differential cross-section predicted by the PWBA theory depends on the assumption that the ^3He nucleus is a point cluster of nucleons; for the $(^3He, p)$ reaction, the further assumption must be made that the transferred nucleon pair are transferred as a lump; i.e., that the transfer is not made in two steps. (See Glendenning 1961 and Newns 1960 for a detailed discussion of these assumptions, particularly for the double-stripping process.) The PWBA theory was used for only two cases in this report for which the DWBA theory could not easily be modified to give better agreement with the experimental data.

The Distorted Wave Born Approximation (DWBA) theory of the direct reaction takes a more sophisticated approach to the evaluation of the transition amplitude by replacing the total wave function in the transition matrix by a wave function which describes the asymptotic behavior of the elastic scattering, usually the dominant process. Generally, optical potentials describing the elastic scattering in the

initial and final channels are introduced, and the wave functions which satisfy the elastic scattering in the asymptotic region are extrapolated into the interior region of strong interaction. A detailed discussion of this approach is given by Satchler (1966), and a similar discussion is also included in the description by Bassel, Drisko, and Satchler (1962) of the zero-range DWBA code JULIE used in this work. A special discussion is given by Adelberger (1967) of the application of this code to the double-stripping process; on the basis of his discussion, the transferred particles in the (^{3}He, p) reaction were assumed, in the present work, to be in a relative s-state, and the work of Balashov and Eltekov (1960) was used in determining the proper radial quantum number for the bound-state wave function calculated by the DWBA code.

Unfortunately, some of the sophistication of the DWBA approach had to be abandoned because optical potentials for the elastic scattering in the incoming and outgoing channels were not available for each of the reactions studied; consequently, it was decided to pick one set of potentials which would give fairly good results for all of the cases studied. The optical potentials for the ^{3}He and α particles were of the form:

$$U(r) = -Vf(x) - iWf(x')$$

$$f(x) = (1 + e^{x})^{-1}$$

$$x = \frac{r - r_o A^{1/3}}{a} \qquad x' = \frac{r - r_o' A^{1/3}}{a'} \quad .$$

The parameters for the ^{3}He and α potentials were taken from an analysis of the ^{19}F(^{3}He, α)^{18}F reaction by Matous, Herling, and

Wolicki (1966) and are listed below. This ^{3}He potential was also used in the present study for all of the (^{3}He, p) reactions.

	V (MeV)	W (MeV)	r_o (f)	a (f)	r_o' (f)	a' (f)	V_{SO} (MeV)	W' (MeV)
^{3}He	183.3	23.2	1.05	0.829	1.81	0.592	--	--
α	65.0	16.5	1.58	0.52	1.58	0.52	--	--
p	64.3	0	1.2	0.65	1.25	0.47	8	44

The proton potential for the (^{3}He, p) reactions was taken initially from an analysis by Glover and Jones (1966) of the (t, p) reaction, but it was found that this potential gave quite poor results. It was necessary to include a surface-absorption term in the potential in order to improve the fits significantly, and the proton potential finally used had the following form:

$$U(r) = -Vf(x) + iW' \frac{d}{dx'} f(x') + \left(\frac{\hbar}{m_\pi c}\right)^2 V_{SO} \frac{1}{x} \frac{d}{dx} f(x) \vec{\ell} \cdot \vec{\sigma} .$$

The parameters for this potential (listed in the table above) was taken from the work of Lee et al. (1964). The theory is fairly sensitive to the depth of the surface-absorption potential, and the fits could be improved by using a different potential depth for each nucleus -- particularly since the proton potential was extracted from reactions in the mass-40 region -- however, it was decided that such a parameter search was beyond the scope of this paper, and the potential depth was not varied.

The potential for the bound state wave function was of the form:

$$U(r) = V_C - V_o f(x)$$

where V_C is the Coulomb potential between a uniformly charged sphere (the core) and the bound particle. The Coulomb radius and the radius and diffusity of the binding potential were taken to be 1.25, 1.25, and 0.65 (times $A^{1/3}f$), respectively, and V_o was varied by the DWBA code until a solution giving the correct binding energy was found.

APPENDIX V

THEORY OF PARTICLE-GAMMA ANGULAR CORRELATIONS

The particular form of the theory of particle-gamma angular correlations used in the present work has been presented by Litherland and Ferguson (1961) and further discussed by Poletti and Warburton (1965). For the geometry used here (discussed in Section D of Chapter II), severe restrictions are placed on the complexity of the correlation which make the analysis of the experimental data relatively simple.

We are concerned with the emission of γ rays from a nuclear state which has been aligned by a nuclear reaction of the form $X(h_1, h_2)Y$. The quantization axis is chosen along the beam direction in this work since the outgoing particles are detected at 0^o. Since both the target and the beam are unpolarized, the nuclear state should be unpolarized; i.e., the positive and negative magnetic substates are symmetrically populated.

If we consider the cases where the aligned state with spin a (and magnetic substates m_a) decays to a state with spin b, and where the state b subsequently decays to a state with spin c, then the angular distributions of the γ rays can be expressed as

$$W(\theta_{ab})_{a\to b} = \sum_k \rho_k(a)\, F_k(abX_{ab})\, Q_k\, P_k\,(\cos\theta_{ab})$$

and (where the first γ ray is unobserved)

$$W(\theta_{bc})_{b\to c} = \sum_k \rho_k(a)\, U_k(abX_{ab})\, F_k(bcX_{bc})\, Q_k\, P_k(\cos\theta_{bc}),$$

where θ is the angle between the direction of emission of the γ rays and the beam direction. $P_k(\cos\theta)$ is a Legendre polynomial and k takes on even values from 0 to 2a. The Q_k are attenuation coefficients for the γ-ray detector, and these coefficients were interpolated for this study from tables given by Ferguson (1965). The $\rho_k(a)$ are statistical tensors which describe the alignment of the initial state, and the $F_k(abX_{ab})$ depend specifically on the γ-ray decay and are independent of the nuclear alignment. The $U_k(abX_{ab})$ are coefficients which link the alignment of the second state (b) to that of the first state through the first γ decay.

There are $(2a + 1)$ population parameters, $P(m_a)$, associated with the magnetic substates of a, but $P(m_a) = P(-m_a)$ because the state a is unpolarized, and this fact is built into the equation for $\rho_k(a)$:

$$\rho_k(a) = \sum_{m_a \geq 0} \rho_k(a, m_a)\, P(m_a)$$

$$\rho_k(a, m_a) = (2 - \delta_{m_a 0}) \frac{(a\ m_a\ a - a \mid k\ 0)}{(a\ m_a\ a - a \mid 0\ 0)} .$$

For the $^{16}O(^3He, \alpha)^{15}O$ reaction with the α-particles detected at 0^o, the magnetic substates of the final state (a) in the ^{15}O nucleus are limited to $|m_a| \leq J_{^3He}$, since the incoming and outgoing channels have no projection of orbital angular momentum along the beam direction and since only the ^3He particle, for which $J = 1/2$, has a non-zero spin. Consequently, $m_a = \pm 1/2$, and $\rho_k(a) = \rho_k(a, 1/2)P(1/2)$.

If we assume that only the two, lowest, allowed multipolarities contribute to the γ decay, $F_k(abX)$ and $U_k(abX)$ are given by

$$F_k(abX) = \frac{F_k(LLba) - (-)^{\sigma} 2XF_k(LL'ba) + X^2F_k(L'L'ba)}{1 + X^2}$$

$$U_k(abX) = \frac{U_k(La\,b) + X^2U(L'ab)}{1 + X^2},$$

where

$$L = \min(1, |b - a|)$$

$$L' = L + 1$$

$$X_{ab} = \frac{\langle b\|L + 1\|a\rangle}{\langle b\|L\|a\rangle}$$

$$F_k(LL'ba) = (-)^{b-a-1}\,[(2L + 1)(2L' + 1)(2a + 1)]^{1/2}$$

$$\times\ (L1L'-1|k\,0)\,W(a\,a\,LL';\ k\,b)$$

$$U_k(La\ b) = \frac{W(a\,b\,a\,b;\ Lk)}{W(a\,b\,a\,b;\ L\,0)}\ .$$

X_{ab} is the multipole-mixing parameter, and $W(a\,b\,a\,b;\ Lk)$ is the Racah coefficient. The exponent σ in $F_k(a\,b\,X)$ is 0 for an ML, EL + 1 mixture and 1 for an EL, ML + 1 mixture. In this study σ was always taken to be 0 regardless of the known or suspected nature of the transition.

The unknown quantities in the equation for the $^{16}O(^{3}He, \alpha\gamma)^{15}O^{*}$ α-γ angular correlations are the population parameter and the multipole mixing(s); P(1/2) factors out of the equation for the correlation so that W(θ) is proportional to it, but W(θ) has a non-linear dependence on the mixing parameter(s).

REFERENCES

Adelberger, E. G. 1967, Ph.D. Thesis, Caltech (unpublished).

Adelberger, E. G. and C. A. Barnes 1966, Phys. Lett. 23, 474.

Adelberger, E. G., C. L. Cocke, and C. N. Davids 1968, submitted to Phys. Rev. Letts.

Ajzenberg-Selove, F. and T. Lauritsen 1968, Submitted to Nuc. Phys.

Ajzenberg-Selove, F. and T. Lauritsen 1959, Nuc. Phys. 11, 1.

Alburger, D. E. and E. K. Warburton 1966, Phys. Rev. 152, 914.

Balashov, V. V. and V. A. Eltekov 1960, Nuc. Phys. 16, 423.

Ball, G. C. and J. Cerny 1966, Phys. Lett. 21, 551.

Banerjee, M. K. 1960, Nuclear Spectroscopy, Part B, Edited by F. Ajzenberg-Selove, Academic Press Inc., New York, P. 695F.

Barnes, C. A., E. G. Adelberger, D. C. Hensley and A. B. McDonald 1966, Proceedings of the Gatlinburg Conference of 1966, Page 261, Academic Press, New York (1967).

Bassel, R. H., D. H. Drisko, and G. R. Satchler 1962, Oak Ridge National Laboratory Report Ornl-3240 (unpublished).

Birge, R. T. 1932, Phys. Rev. 40, 207.

Brown, A. B., C. W. Snyder, W. A. Fowler, and C. C. Lauritsen 1951, Phys. Rev. 82, 159.

Butler, G. W., J. Cerny, S. W. Cosper, and R. L. McGrath 1968, Phys. Rev. 166, 1096.

Caughlan, G. R. and W. A. Fowler 1962, Ap. J. 136, 453.

Cerny, J., R. H. Pehl, G. Butler, D. G. Gleming, C. Maples, and C. Detraz 1966, Phys. Lett. 20, 35.

Chasman, C., K. W. Jones, R. A. Ristinen, and D. E. Alburger 1967, Phys. Rev. 159, 830.

Cohen, E. R. and J. W. M. DuMond 1964, Proceedings of the Second International Conference on Nuclidic Masses and Related Constants, Springer-Verlag, Vienna, Austria, P. 152.

Demirlioglu, D. and W. Whaling 1962, Up-to-date graphs for "The Energy Loss of Charged Particles in Matter" by W. Whaling 1958, Handbuch der Physik 34, 193 (unpublished).

Dietrich, F. S. 1965, Nuc. Phys. 69, 49.

Douglas, R. A., B. R. Gasten, and A. Mukerji 1956, Can. J. Phys. 34, 1097.

Earwaker, L. G. and J. H. Montague 1968, Nuc. Phys. A109, 507.

Endt, P. M. and C. van der Leun 1967, Nuc. Phys. 105, 1.

Esterlund, R. A., R. McPherson, A. M. Poskanzer, and P. L. Reeder 1967, Phys. Rev. 156, 1094.

Evans, A. E. 1967, Phys. Rev. 155, 1047.

Ferguson, A. J. 1965, Angular Correlation Methods in Gamma-ray Spectroscopy, North-Holland Publishing Co., Amsterdam, Table VII(a), P. 196.

Gallmann, A., F. Haas, and N. Balaux 1966, Phys. Rev. 151, 735.

Gill, R. D., J. S. Lopes, B. C. Robertson, R. A. I. Bell, and H. J. Rose 1966, Nuc. Phys. 84, 683.

Glashausser, C. and M. E. Rickey 1967, Phys. Rev. 154, 1033.

Glendenning, N. K. 1961, Nuc. Phys. 29, 109.

Glover, R. N. and A. D. W. Jones 1966, Nuc. Phys. 81, 268.

Goosman, D. R. 1967, Ph.D. Thesis, Caltech (unpublished).

Gorodetzky, S., R. M. Freeman, A. Gallmann, and F. Haas 1966, Phys. Rev. 149, 801.

Groce, D. E. 1963, Ph.D. Thesis, Caltech (unpublished).

Hay, H. J. and D. C. Kean 1967, Nuc. Phys. 98, 330.

Henley, E. M. 1966, Isobaric Spin in Nuclear Physics, Edited by J. D. Fox and D. Robson, Academic Press, New York, P. 3.

Hensley, D. C. 1967, Ap. J. 147, 818.

Hinds, S., H. Marchant, and R. Middleton 1962, Nuc. Phys. 31, 118.

Hinds, S. and R. Middleton 1959, Proc. Phys. Soc. 74, 799.

Horvat, P. 1964, Nuc. Phys. 52, 410.

Lauritsen, T. and F. Ajzenberg-Selove 1966, Nuc. Phys. 78, 1.

Lee, L. L., J. P. Schiffer, B. Zeidman, G. R. Satchler, R. M. Drisko, and R. H. Bassel 1964, Phys. Rev. 136, B971.

Litherland, A. E. and A. J. Ferguson 1961, Can. J. Phys. 39, 788.

Litherland, A. E., R. Batchelor, A. J. Ferguson, and H. E. Gove 1961, Canad. Journ. Phys. 39, 276.

Lopes, J. S., O. Haeusser, H. J. Rose, A. R. Poletti, and M. F. Thomas 1966, Nuc. Phys. 76, 223.

Lynch, B., G. M. Griffiths, and T. Lauritsen 1965, Nuc. Phys. 65, 641.

McDonald, A. B. and E. G. Adelberger 1968, Phys. Lett. 26B, 380.

McDonald, A. B., J. R. Patterson, and H. Winkler 1968, Bull. Am. Phys. Soc. 13, 652.

McNally, J. H. 1966, Ph.D. Thesis, Caltech (unpublished).

Marion, J. B. 1966, Rev. Mod. Phys. 38, 660.

Marion, J. B. and W. A. Fowler 1957, Ap. J. 125, 221.

Matous, G. M., G. H. Herling, and E. A. Wolicki 1966, Phys. Rev. 152, 908.

Mattauch, J. 1960, Proceedings of the Conference on Nuclidic Masses, Edited by H. E. Duckworth, University of Toronto Press, P. 3.

Mattauch, J. H. E., W. Thiele, and A. H. Wapstra 1965, Nuc. Phys. 67, 1.

Max-Planck Institut für Kernphysik 1966, Jahresbericht, P. 27.

Middleton, R. and D. J. Pullen 1964, Nuc. Phys. 51, 50.

Miller, R. G. and G. W. Kavanagh 1966, Bull. Am. Phys. Soc. 11, 315.

Moss, C. E. 1968, Ph.D. Thesis, Caltech (unpublished).

Newns, H. C. 1960, Proc. Phys. Soc. 76, 489.

Pixley, R. E. 1957, Ph.D. Thesis, Caltech (unpublished).

Poletti, A. R. and E. K. Warburton 1965, Phys. Rev. 137, 595.

Povh, B. and D. F. Hebbard 1959, Phys. Rev. 115, 608.

Rinsvelt, H. van and P. B. Smith 1964, Physica 30, 59.

Rolland, W. W. 1963, Ph.D. Thesis, Duke University (unpublished).

Satchler, G. R. 1966, Nuclear Structure Physics, Volume VIII C, University of Colorado Press, Boulder, P. 73.

Smith, P. B. 1964, Canad. J. Phys. 42, 1101.

Tangen, R. 1946, Det. Kgl. Norske Videnskabers Selskabs Skriffer, No. 1.

Wapstra, A. H., G. J. Nijgh, and R. van Lieshout 1959, Nuclear Spectroscopy Tables, North Holland Pub. Co., Amsterdam.

Warburton, E. K., J. W. Olness, and D. E. Adelburger 1965, Phys. Rev. 140, 1202.

Weinberg, S. and S. B. Treiman 1959, Phys. Rev. 116, 465.

Wilkinson, D. H. 1960, Nuclear Spectroscopy, Part B, Edited by F. Ajzenberg-Selove, Academic Press Inc., New York, P. 852F.

Wilkinson, D. H. 1964, Phys. Rev. Lett. 13, 571.

Wilkinson, D. H. 1966, Isobaric Spin in Nuclear Physics, Edited by J. D. Fox and D. Robson, Academic Press, New York, P. 30.

TABLE I

Separation Measurements in ^{15}O

These excitation-energy separations in ^{15}O were measured with the $^{16}O(^{3}He, \alpha)$ reaction. A brief description in the various experiments is given in the lower part of the table. See pages 13 through 21.

TABLE I

SEPARATION MEASUREMENTS IN ^{15}O
(keV)

Separation	A	B	C	D	E	F	Weighted Average
(7-6)	280.8 ± 3.8	279.8 ± 3.5	281.0 ± 1.2	280.5 ± 1.3			280.7 ± 0.9
(7-5)	696.6 ± 4.6	696.1 ± 4.0	696.4 ± 1.7				696.4 ± 1.5
(7-4)	764.8 ± 4.6	762.0 ± 4.0	763.6 ± 1.7				763.5 ± 1.5
(6-5)	416.0 ± 1.7	416.5 ± 3.5	415.3 ± 1.1		415.4 ± 3.0		415.6 ± 0.9
(6-4)	483.6 ± 1.6	482.4 ± 3.5	482.5 ± 1.1		483.9 ± 3.0		482.9 ± 0.9
(5-4)	67.6 ± 1.6	65.9 ± 4.0	67.1 ± 1.5		68.5 ± 3.0	69.1 ± 4.2	67.5 ± 1.0

EXPERIMENTAL PROCEDURE

Experiment	Target	Incident Energy	Angles (degrees)
A	NiO	12 MeV	10, 15, 20, 25, 30, 35, 40, 50, 60, 70
B	SiO	12 MeV	30, 50, 70, 60, 40
C	WO_3	12 MeV	50, 60, 70, 80, 50, 65, 55
D	SiO	8 MeV	30, 20, 15, 40, 45, 20, 25
E	NiO	12 MeV	10, 45
F	$Ni^{18}O$	10 MeV	10, 15, 20

TABLE II

Separation Measurements in ^{15}O

These excitation-energy separations in ^{15}O were measured with the $^{16}O(^{3}He, \alpha)$ reaction. A brief description of the various experiments is given in the lower part of the table. Recent γ-ray energy measurements of some of the energy separations are listed in the last column, for comparison. See pages 13 through 21.

TABLE II

SEPARATION MEASUREMENTS IN ^{15}O

(keV)

Separation	A	B	C	D	E	Weighted Average	Gamma-Ray Energies
(6-3)	1103.2 ± 2.0				1104.9 ± 3.5	1103.6 ± 1.7	
(6-2)	2034.9 ± 2.1				2035.4 ± 3.5	2035.0 ± 1.8	2034.7 ± 0.3[a]
(5-3)	687.3 ± 2.0		688.5 ± 4.2		689.5 ± 3.4	688.0 ± 1.6	
(5-2)	1619.1 ± 2.0		1621.2 ± 4.2		1620.1 ± 3.4	1619.6 ± 1.6	1618.5 ± 0.8[a]
(3-2)	931.8 ± 2.0	931.2 ± 2.3	931.8 ± 2.6	931.2 ± 2.4	930.5 ± 3.4	931.4 ± 1.1	
(3-1)	991.5 ± 2.1	991.1 ± 2.3		993.0 ± 3.5	992.9 ± 3.4	991.8 ± 1.3	
(2-1)	59.4 ± 1.7	60.0 ± 2.4		62.2 ± 3.5	62.7 ± 3.4	60.3 ± 1.2	
(3-0)	6172.9 ± 4.5	6172.3 ± 2.0		6170.6 ± 5.0	6171.2 ± 4.3	6172.1 ± 1.6	6180.0 ± 4.0[b]
(2-0)	5240.9 ± 4.5	5241.0 ± 2.6		5239.4 ± 5.0	5242.2 ± 4.4	5241.0 ± 1.9	5241.5 ± 0.5[c]
(1-0)	5181.3 ± 4.5	5181.0 ± 2.6		5177.4 ± 5.5	5179.9 ± 4.4	5180.4 ± 1.9	

[a] Alburger and Warburton (1966)

[b] Warburton, Olness, and Alburger (1965)

[c] Chasman et al. (1967)

EXPERIMENTAL PROCEDURE

Experiment	Target	Incident Energy	Angles (degrees)
A	NiO	12 MeV	10, 15, 20, 25, 30, 35, 40, 50, 60, 70
B	Boron	12 MeV	10, 15, 10
C	$Ni^{18}O$	10 MeV	10, 15, 20
D	NiO	10 MeV	10, 15, 20, 10
E	NiO	12 MeV	10, 45

TABLE III

^{15}O Q-Values Relative to the Mass-Table Value for the Ground-State Q-Value

The Q-values in this table are for the $^{16}O(^{3}He, \alpha)$ reaction to states of ^{15}O and are given relative to the mass-table[a)] value of 4910.14 keV for the ground-state Q-value. A brief description of the various experiments is given in the lower part of the table. Recent γ-ray energy measurements of some of the corresponding excitation energies are listed in the last column, for comparison. See pages 13 through 21.

TABLE III

^{15}O Q-VALUES RELATIVE TO THE MASS-TABLE[a] VALUE FOR THE GROUND-STATE Q-VALUE
(keV)

State	A	B	C	Weighted Average	Gamma-Ray Energies
7	7553.0 ± 3.3				
6	7272.2 ± 2.0				7276.2 ± 0.6[b, c]
5	6856.3 ± 3.4				6860.0 ± 1.0[b, c]
4	6788.1 ± 3.4				
3	6168.8 ± 3.0	6167.55 ± 1.3	6167.7 ± 3.0	6167.8 ± 1.1	6180.0 ± 4.0[d]
2	5237.6 ± 3.6	5236.45 ± 1.8	5236.6 ± 3.0	5236.6 ± 1.4	5241.5 ± 0.5[c]
1	5176.7 ± 4.3	5176.5 ± 2.6	5174.9 ± 4.5	5176.2 ± 2.0	
0		-4.74 ± 1.3	-2.9 ± 4.5	-4.60 ± 1.2	

[a] Mattauch, Thiele, and Wapstra (1965)

[b] Alburger and Warburton (1966)

[c] Chasman et al. (1967)

[d] Warburton, Olness, and Alburger (1965)

EXPERIMENTAL PROCEDURE

Experiment	Target	Incident Energy	Angles (degrees)
A	NiO	12 MeV	50
B	Boron	12 MeV	10, 15, 10
C	NiO	10 MeV	10, 15, 20, 10

TABLE IV

Calibration Reactions for the ^{15}O Q-Value Determinations Using Boron Targets

The reactions listed in this table were used to determine the ^{15}O Q-values for the $^{16}O(^{3}He, \alpha)$ reaction from the data taken on thin boron targets; the measurements were performed at an incident energy of 12 MeV and at angles of 10^{o} and 15^{o}. The calibration Q-values are listed in the second column according to the excitation energy in the residual nucleus. The last column lists, as a check of internal consistency, the values for the calibration reactions as they were determined from the data. (See Appendix I for a discussion of the method used for determining Q-values.) All ground-state mass excesses were taken from the mass tables of Mattauch, Thiele, and Wapstra (1965). See pages 18 and 19.

TABLE IV

CALIBRATION REACTIONS FOR THE ^{15}O Q-VALUE DETERMINATIONS USING BORON TARGETS

Reaction	Excitation Energies	
	Calibration (keV)	Experimental (keV)
$^{16}O(^{3}He, d)^{17}F$ [a]	0.0 ± 0.5	0.3 ± 0.7
$^{16}O(^{3}He, p)^{18}F$ [a]	0.0 ± 0.8	1.8 ± 2.0
$^{11}B(^{3}He, d)^{12}C$ [b]	16106.2 ± 0.5	16106.2 ± 0.6
$^{11}B(^{3}He, \alpha)^{10}B$ [c]	0.0 ± 0.5	-1.9 ± 3.9
	717.3 ± 1.0	719.3 ± 5.3
	1740.0 ± 2.0	1740.2 ± 5.3
	2154.0 ± 3.0	2152.4 ± 5.2
	3585.0 ± 4.0	3585.6 ± 1.8
	4774.0 ± 3.0	4772.5 ± 1.8
	5114.0 ± 4.0	5111.5 ± 3.4
	5166.0 ± 4.0	5164.9 ± 2.1
	7479.0 ± 2.0	7475.7 ± 3.3

a) Mattauch, Thiele, and Wapstra (1965)
b) Ajzenberg-Selove and Lauritsen (1959)
c) Lauritsen and Ajzenberg-Selove (1966)

TABLE V

Additional Q-Value Determinations From
the Boron-Target Data

The first column of this table lists various reactions which, in addition to the $^{16}O(^{3}He, \alpha)$ reaction and those listed in Table IV, were included in the boron-target data but whose Q-values were not precisely enough known for their inclusion as calibration reactions for the ^{15}O Q-value determinations. (See pages 18 and 19.) The large discrepancy between the measurements of the present work and the previous values for the $^{11}B(^{3}He, t)^{11}C$ reaction is discussed on page 19.

TABLE V

ADDITIONAL Q-VALUE DETERMINATIONS FROM THE BORON-TARGET DATA

Reaction	Excitation Energies Present Work (keV)	Previous Work (keV)	Reference
$^{12}C(^{3}He,\alpha)^{11}C$	0.9 ± 2.1	0.0 ± 1.2	a
	1999.3 ± 2.5	1995.0 ± 3.0	a
$^{11}B(^{3}He,t)^{11}C$	4320.7 ± 0.5	4305.0 ± 6.0	a
	4807.2 ± 0.7	4794.0 ± 6.0	a
$^{10}B(^{3}He,d)^{11}C$	6483.4 ± 0.7	6480.0 ± 6.0	a
	8421.4 ± 3.0	8420.0 ± 4.0	a
$^{11}B(^{3}He,d)^{12}C$	12711.5 ± 1.6	12713.0 ± 6.0	a
	15109.9 ± 0.7	15109.0 ± 4.0	a
$^{11}B(^{3}He,p)^{13}C$	15104.5 ± 1.4		
	19122.3 ± 3.0		
$^{16}O(^{3}He,p)^{18}F$	3724.0 ± 3.0	3725.0 ± 10.0	b

a) Lauritsen and Ajzenberg-Selove (1968)

b) Ajzenberg-Selove and Lauritsen (1959)

TABLE VI

Corrections to the Ground-State Mass Excess of ^{15}O

This table lists the corrections to the ground-state mass of ^{15}O which would be necessary to bring the γ-ray energy measurements and the Q-value measurements for the $^{16}O(^{3}He, \alpha)^{15}O$ reaction (see Table III) into agreement; the disagreement between these measurements is discussed on pages 16ff. The first seven entries in the table are the "excitation energies" derived by comparing the measured Q-values for the $^{16}O(^{3}He, \alpha)^{15}O$ reaction with the mass-table value for the Q-value to the ground state. The corresponding corrections to the mass excess of ^{15}O are obtained by comparing these energies with the γ-ray energies as discussed on pages 20 and 21. The last three corrections are obtained by comparing the energy separations and the appropriate γ-ray energies with the "excitation energy" for the 7th excited state of ^{15}O (7552.32 ± 0.4 keV) obtained by adding E_r to the mass-table value for the energy of the $^{14}N + p$ threshold in ^{15}O. (See pages 15 and 16 for a discussion of E_r.)

The application of this mass-excess correction to the energy scheme for ^{15}O is discussed on pages 19 and 20.

TABLE VI

CORRECTIONS TO THE GROUND-STATE MASS EXCESS[a] OF ^{15}O

State	Excitation Energy (keV)	ΔM (keV)
6	7272.2 ± 2.0	-4.0 ± 2.1
5	6856.3 ± 3.4	-3.7 ± 3.5
4	6788.1 ± 3.4	-4.9 ± 3.5
3	6167.8 ± 1.1	-4.95 ± 1.4
2	5236.6 ± 1.4	-4.9 ± 1.5
1	5176.2 ± 2.0	-5.0 ± 2.4
0	-4.60 ± 1.2	-4.6 ± 1.2

Separation	Energy (keV)	
(7-6)	280.7 ± 0.9	-4.6 ± 1.2
(7-5)	696.4 ± 1.5	-4.1 ± 1.8
(7-4)	763.5 ± 1.5	-4.2 ± 1.8

ΔM_{WA} = -4.58 keV

e_{int} = 0.53 keV

e_{ext} = 0.21 keV

[a] Mattauch, Thiele, and Wapstra (1965)

TABLE VII

Coefficients for Legendre Polynomial Fits to
^{15}O Angular-Correlation Data

The first column of this table indicates the various γ-ray transitions which were measured. The notation "(2-0)" indicates the γ-ray decay of the 2nd excited state to the ground state; the notation 5-(2-0) indicates the same γ-ray decay but where it follows the γ-ray decay of the 5th excited state to the 2nd excited state. The a_2 and a_4 coefficients obtained from a least-squares adjustment of an expansion in Legendre polynomials to the data are given in the 2nd and 3rd columns of the table; and the same coefficients obtained by fitting the data with the theoretical expansion discussed in Appendix V are given in the next two columns. The a_4 coefficient must be zero for an initial spin of 3/2, and a possible a_6 coefficient for the angular correlation for the 6th excited state (spin 7/2) is predicted to be zero. The angular-correlation data and the subsequent theoretical fits are shown in Figure 13. (See pages 23 through 28.)

TABLE VII

COEFFICIENTS FOR LEGENDRE POLYNOMIAL FITS TO ^{15}O ANGULAR-CORRELATION DATA

Transition	a_2	a_4	a_2 (theory)	a_4 (theory)	χ^2	J_a	J_b
(2-0)	0.377 ± 0.04	-0.509 ± 0.06	0.447	-0.547	3.87	5/2	1/2
(3-0)	-0.112 ± 0.025		-0.112		0.18	3/2	1/2
(4-0)	-0.298 ± 0.023		-0.298		1.22	3/2	1/2
(5-2)	0.358 ± 0.069	-0.210 ± 0.094	0.420	0.0	1.77	5/2	5/2
5-(2-0)	0.316 ± 0.037	0.191 ± 0.050	0.294	0.078	2.61	5/2	1/2
(6-2)	-0.374 ± 0.081	0.087 ± 0.132	-0.402	0.001	0.05	7/2	5/2
6-(2-0)	0.384 ± 0.069	-0.321 ± 0.093	0.407	-0.339	0.23	5/2	1/2

TABLE VIII

Mixing Parameters for Gamma-Ray Transitions in ^{15}O

The multipole-mixing parameters derived in the present work for the various γ-ray transitions in ^{15}O are given in column A; the notation "(2-0)" indicates the γ-ray transition from the 2^{nd} excited state of ^{15}O to the ground state. (The angular-correlation data are shown in Figure 13, and the theoretical fits to the data are presented in the same figure and in Table VII.) For several cases the solution for the mixing parameter was double-valued, and both solutions have been included. The parameter σ defined in Appendix V, which is related to the phase of the multipole mixing, was set equal to zero in the analysis of all of the angular correlations. For comparison, results from other measurements are included in the table.

The multipole-mixing parameters were derived from the angular-correlation data following a method of analysis outlined by Smith (1964), and the uncertainties in the parameters have been adjusted to take into account the value of χ^2 for the theoretical fit following a recommendation of Wapstra et al. (1959). (See pages 23 through 28.)

TABLE VIII

MIXING PARAMETERS FOR GAMMA-RAY TRANSITIONS IN ^{15}O

Transition	A	B	C	D	E	F
(2-0)	0.11 ± 0.09	0.13 ± 0.05	$0.0^{+0.12}_{-0.05}$	$0.035^{+0.11}_{-0.04}$		
	2.11 ± 0.5		$2.9^{+1.8}_{-0.9}$	$2.5^{+0.3}_{-0.6}$		
(3-0)	-0.203 ± 0.014	-0.17 ± 0.02		$-0.19^{+0.04}_{-0.07}$	-0.17 ± 0.01	0.12 ± 2.3
	2.984 ± 0.135			$2.9^{+1.1}_{-0.5}$	2.7 ± 0.1	-2.3 ± 0.2
(4-0)	-0.095 ± 0.02	-0.10 ± 0.02				0.108 ± 0.03
	2.185 ± 0.09	2.2 ± 0.4				-2.1 ± 0.2
(5-2)	-0.006 ± 0.10	-0.04 ± 0.03	$0.05^{+0.7}_{-0.1}$			
(6-2)	0.043 ± 0.04					

A) Present work. (Phase convention for the mixing parameters: $\sigma = 0$. See Appendix V.)
B) Gill et al. (1966)
C) Gallmann et al. (1966)
D) Gorodetzky et al. (1966)
E) Lopes et al. (1966)
F) Povh and Hebbard (1959) (The sign convention for this work is opposite to the sign convention for the other results.)

TABLE IX

Summary of Results for ^{15}O

The assignment of excitation energies to the states of ^{15}O is discussed on page 29, and the energies assigned to the four quantities listed in the lower part of the table are discussed on pages 29 and 30. The dependence of these energies on the measured energy for the γ ray de-exciting the 2nd excited state of ^{15}O should be carefully noted (see page 21 and page 30).

The ℓ-value assignments to the particle angular distributions from the $^{16}O(^{3}He, \alpha)^{15}O$ reaction are discussed on pages 21 through 23. Spins and parities were assigned to the states of ^{15}O on the basis of these ℓ-values and the results of the α-γ angular correlations discussed on pages 26 through 28. (See also pages 30 and 31.)

TABLE IX

SUMMARY OF RESULTS FOR ^{15}O

State	Excitation Energy (keV)	J^{π}	ℓ_n
0	0.0	$1/2^-$	1
1	5181.2 ± 1.3	$1/2^+$	0
2	5241.5 ± 0.5	$5/2^+$	2
3	6172.8 ± 1.0	$3/2^-$	1
4	6793.0 ± 0.9	$3/2^+$	2
5	6860.0 ± 1.0	$5/2^+$	2
6	7276.2 ± 0.6	$7/2^+$	(4)
7	7556.9 ± 0.7		

^{14}N + p threshold	7297.4 ± 0.6 keV
^{15}O Mass Excess	2855.3 ± 0.6 keV
(threshold - 6)	21.2 ± 0.6 keV
$^{16}O + {}^{3}He - \alpha - {}^{15}O$	4914.7 ± 0.6 keV

TABLE X

Measurement of the Excitation Energy
of the Lowest T = 3/2 State of ^{13}C

These measurements of the excitation energy of the lowest T = 3/2 state in ^{13}C were made using the $^{11}B(^{3}He, p)$ reaction and an incident energy of 8 MeV. The Q-value for this reaction was calculated relative to the Q-values for the $^{16}O(^{3}He, p)^{18}F$ and $^{12}C(^{3}He, p)^{14}N(1)$ reactions on the ^{16}O and ^{12}C present as contaminants in the boron target. The consistency of the measurements was checked by including data taken at each angle using a carbon target.

The internal and external probable errors of the ^{13}C excitation-energy measurements are given in the lower part of the table; $\bar{e}$ is the average value of the probable errors assigned to the ^{13}C excitation-energy measurements.

See pages 44 through 46.

TABLE X

MEASUREMENT OF THE EXCITATION ENERGY
OF THE LOWEST T = 3/2 STATE IN ^{13}C

	Boron Target			Carbon Target	
Angle	$^{13}C(T=3/2)$ (keV)	$^{18}F(0)$ (keV)	$^{14}N(1)$[a] (keV)	$^{14}N(1)$[a] (keV)	$^{14}N(0)$ (keV)
0^o	15106.5 ± 1.5	-1.1 ± 1.8		2314.5 ± 1.8	
	15107.8 ± 1.5				
10^o	15106.6 ± 2.2	0.4 ± 2.9	2313.7 ± 2.3	2311.4 ± 1.8	
	15105.0 ± 1.8				
20^o	15103.7 ± 1.5		2312.9 ± 2.3	2311.4 ± 1.8	
55^o	15105.8 ± 1.8	(9.6)		2314.8 ± 1.7	
90^o	15105.0 ± 1.4	1.6 ± 2.2		2314.3 ± 1.7	
130^o	15102.0 ± 1.3	-1.3 ± 2.2		2309.8 ± 2.8	-1.3 ± 1.7
Average	15105.3 ± 0.6	-0.1 ± 1.0	2313.3 ± 0.3	2312.8 ± 0.8	
Weighted Average	15105.1 ± 0.6	-0.2 ± 1.1	2313.3 ± 1.6	2313.3 ± 0.8	

e_{int} = 0.6 keV $\quad \bar{e}$ = 1.62 keV

e_{ext} = 0.6 keV $\quad$ RMS$(e - \bar{e})/\bar{e}$ = 0.27 keV/$\bar{e}$ = 17%

a) Ex = 2312.9 ± 0.1 keV Chasman et al. (1967).

TABLE XI

SUMMARY OF RESULTS FOR
T = 3/2 STATES IN ^{13}C

Excitation Energy (keV)	L (^{3}He, p)	J^π	Width (keV)
15104.9 ± 3	0	$3/2^-$	≤ 6
18655.0 ± 10			
18692.0 ± 15			
19121.5 ± 5	2	$\leq 7/2^-$	≤ 15

Other Measurements of the Excitation Energy of the Lowest T = 3/2 State in ^{13}C

15114 ± 5 keV	Miller (1966)
15103 ± 45 keV	Cerny et al. (1966)
15108 ± 14 keV	Ball and Cerny (1966)

TABLE XII

SUMMARY OF RESULTS FOR
T = 3/2 STATES IN ^{17}O

Excitation Energy (keV) ($^3He, \alpha$)	Excitation Energy (keV) ($^3He, p$)	ℓ_n ($^3He, \alpha$)	L ($^3He, p$)	J^π	Width (keV)
11076 ± 4	11070 ± 20	1	0	$1/2^-$	≤ 20
12467 ± 4	12470 ± 20	1	2	$3/2^-$	≤ 20
12947 ± 5		0		$1/2^+$	≤ 20
12994 ± 5	13007 ± 20	3, (2)	2	$5/2^-$	≤ 20
13636 ± 4		2		$3/2^+$, $5/2^+$	≤ 20
14210 ± 10					≤ 40
14243 ± 10					≤ 40

TABLE XIII

SUMMARY OF RESULTS FOR
$T = 3/2$ STATES IN ^{21}Ne

Excitation Energy (keV) (a)	Excitation Energy (keV) (b)	Excitation Energy (keV) (c)	ℓ_n ($^3He, \alpha$)	L ($^3He, p$)	J^π	Width (keV)
8856 ± 6	8840 ± 10	8920 ± 40	1, 2	2	$3/2^+, 5/2^+$	≤ 40
9139 ± 6	9136 ± 10	9210 ± 40	0	0	$1/2^+$	≤ 25
9962 ± 6		10040 ± 40	1		$1/2^-, 3/2^-$	≤ 60
10602 ± 10			(2)			≤ 80
10901 ± 10			(1, 2)			≤ 80

a) Present work

b) Hinds and Middleton (1959)

c) Butler et al. (1968)

TABLE XIV

Comparison of Predictions of the Quadratic Mass Equation with Experimental Measurements

The quadratic mass equation (see pages 36 and 37) can be used to predict the mass of the proton-rich end member from the masses of the three other members of the T = 3/2 isospin quartet; the measured value and the predicted value for the mass excess of the proton-rich end members of various completed T = 3/2 quartets are given in the 2^{nd} and 3^{rd} columns, respectively. The significance of these comparisons and of the last two columns of the table is discussed on pages 75ff.

TABLE XIV

COMPARISON OF PREDICTIONS OF THE QUADRATIC MASS EQUATION WITH EXPERIMENTAL MEASUREMENTS

Nuclide	Mass Excess (keV) Experimental	Predicted	d (keV)	$c\alpha\overline{Z}$ (keV)
^{9}C	28916 ± 5	28959.5 ±29	- 7.2 ± 4.9	8.7 ± 0.2
^{13}O	23110 ± 70	23116 ±22	- 0.5 ± 12.2	12.2 ± 0.8
^{17}Ne	16470 ±250	16511 ±31	- 6.8 ± 42.0	14.3 ± 3.8
$^{21}Mg(0)$	10620 ±120	10940 ±38	-53.3 ± 21.0	12.7 ± 2.3
$^{21}Mg(1)$	10840 ±124	11099 ±39	-43.2 ± 21.6	12.1 ± 2.4

TABLE XV

Gas-Target Calibration Reactions (^{22}Ne)

These reactions were used, along with the measured value of the gas pressure and the incident energy, to determine the thicknesses of the entrance and exit windows of the gas target; the derived thicknesses are given in the lower part of the table. The ^{16}O was present as a small contamination in the ^{22}Ne gas. For additional details, see pages 92ff of Appendix I.

TABLE XV

GAS-TARGET CALIBRATION REACTIONS (^{22}Ne)

Reaction	Calibration Excitation Energy (keV)	Deviation (keV)	Energy Loss in Exit Window (keV)	Reference
$^{22}Ne(^{3}He, \alpha)^{21}Ne$	0.0 ± 1.5	0.6 ± 3.7	171	a
	350.0 ± 10	-1.6 ± 1.4	175	b
	1736.0 ± 10	3.7 ± 5.3	182	b
	2789.0 ± 10	-2.6 ± 3.6	190	b
$^{16}O(^{3}He, \alpha)^{15}O$	0.0 ± 0.7	0.7 ± 0.7	209	c
	6172.8 ± 1.1	-2.1 ± 4.1	283	c
$^{22}Ne(^{3}He, p)^{24}Na$	1346.7 ± 3.5	-4.8 ± 2.9	17	d
	1885.4 ± 3.5	-4.7 ± 1.3	17	d
	3409.0 ± 8	1.2 ± 4.6	18	d
$^{16}O(^{3}He, p)^{18}F$	0.0 ± 0.8	-0.5 ± 5.5	21	a
$^{22}Ne(^{3}He, d)^{23}Na$	3679.0 ± 5	1.6 ± 3.3	41	e
	3915.0 ± 5	1.9 ± 1.6	42	e
	5378.0 ± 5	1.7 ± 1.8	47	e
	5738.0 ± 9	4.3 ± 3.6	48	e
	6304.0 ± 6	1.8 ± 3.8	50	e
$^{16}O(^{3}He, d)^{17}F$	0.0 ± 0.5	1.5 ± 2.3	60	a
	Entrance Window	6397 ± 74 Å Nickel		
	Exit Window	10447 ± 129 Å Nickel		

a) Mattauch, Thiele, and Wapstra (1965)

b) Hinds and Middleton (1959)

c) Present work; see Table IX.

d) Endt and van der Leun (1967)

e) Hay and Kean (1967)

TABLE XVI

Gas-Target Calibration Reactions (^{20}Ne)

These reactions were used, along with the measured value of the gas pressure and the incident energy, to determine the thicknesses of the entrance and exit windows of the gas target; the derived thicknesses are given in the lower part of the table. The ^{16}O was present as a small contamination in the ^{20}Ne gas. These window thicknesses were derived in order to check the thicknesses derived from data taken with ^{22}Ne as the target gas (see Table XV). For additional details, see pages 92ff of Appendix I.

TABLE XVI

GAS-TARGET CALIBRATION REACTIONS (^{20}Ne)

Reaction	Calibration Excitation Energy (keV)	Deviation (keV)	Energy Loss in Exit Window (keV)	Reference
^{20}Ne(^{3}He, d)^{21}Na	0.0 ± 8	0.7 ± 2.5	50	a
	338.0 ± 8	-5.3 ± 5.9	52	b
^{16}O(^{3}He, d)^{17}F	0.0 ± 0.5	0.7 ± 2.9	60	a
^{20}Ne(^{3}He, α)^{19}Ne	0.0 ± 1.6	-2.6 ± 3.9	217	a
^{16}O(^{3}He, α)^{15}O	0.0 ± 0.7	2.0 ± 6.3	208	c
^{20}Ne(^{3}He, p)^{22}Na	0.0 ± 2.7	3.7 ± 1.0	17	a
	890.9 ± 3	-2.6 ± 0.8	18	b
	1528.0 ± 3	-2.6 ± 1.3	18	b
	1936.0 ± 3	2.7 ± 2.0	19	b
	2571.5 ± 3	-1.9 ± 0.7	20	b
	2969.0 ± 3	0.9 ± 2.3	20	b
	3949.0 ± 5	1.4 ± 1.6	21	b
^{16}O(^{3}He, p)^{18}F	0.0 ± 0.8	0.3 ± 3.8	21	a

Entrance Window	6464 ± 87 Å	Nickel
Exit Window	10325 ± 181 Å	Nickel

a) Mattauch, Thiele, and Wapstra (1965)

b) Endt and van der Leun (1967)

c) Present work; see Table IX.

TABLE XVII

RECIPROCAL COLLECTION-EFFICIENCY FACTORS
FOR THE 16-COUNTER ARRAY
(per cent)

θ/ϕ[a]	4/15	4/8	1/15	
Counter				
1	94	94	91	93
2	114	114	111	110
3	100	97	95	96
4	97	96	94	95
5	101	98	94	97
6	103	100	97	100
7	101	101	98	100
8[b]	100	100	100	100
9	106	104	103	103
10	106	105	103	104
11	112	108	106	106
12	105	104	105	108
13	110	108	106	107
14	110	109	107	111
15	111	110	109	113
16	103	102	106	108

a) Settings equal to 1/2 of the θ and ϕ slit openings in the arbitrary units marked on the spectrometer box.

b) Equal to 100 by definition.

(For additional details, see Appendix III.)

FIGURE 1

Spectra of the elastic scattering of ^{3}He particles on the gold backing of a ^{14}C target, with the target turned at 45^{o} to the beam. The upper spectrum was taken with the target positioned so that the ^{3}He particles had to pass through the ^{14}C layer both before and after scattering on the gold backing. See Sections A and C of Chapter II for additional details.

FIGURE 1

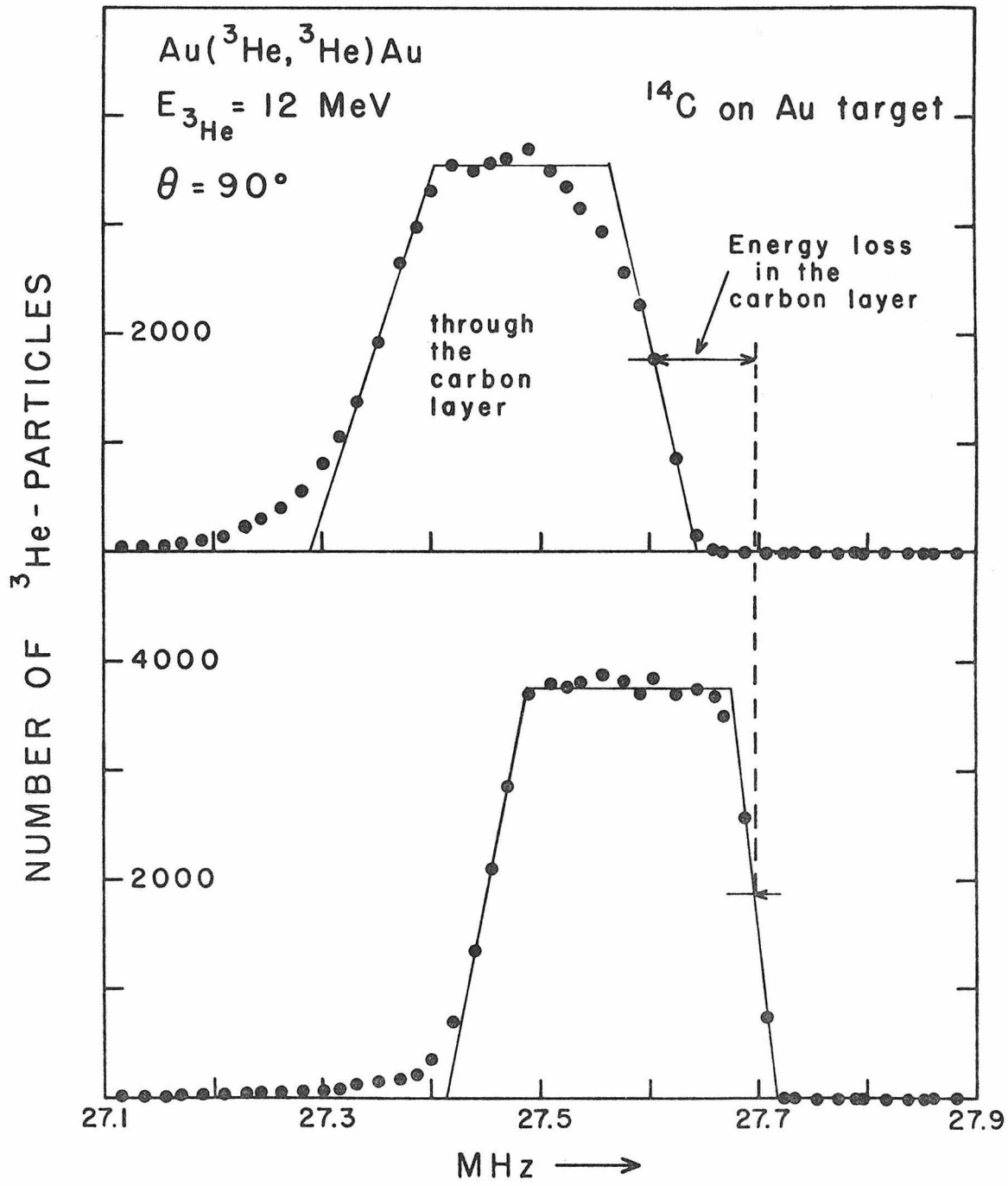
Au(3He, 3He)Au
E3He = 12 MeV
θ = 90°
14C on Au target
Energy loss in the carbon layer
through the carbon layer
2000
4000
2000
NUMBER OF 3He-PARTICLES
27.1
27.3
27.5
27.7
27.9
MHz

FIGURE 2

The lower spectrum shows the 8.785-MeV α-particle group from a ^{212}Po α source. The low-energy tail is probably an indication of ^{212}Po atoms buried in the stainless-steel rod on which the ^{212}Po atoms had been accumulated. The upper spectra show α particles from the same α source which have passed through thin self-supporting targets. See Sections A and C of Chapter II for additional details.

FIGURE 2

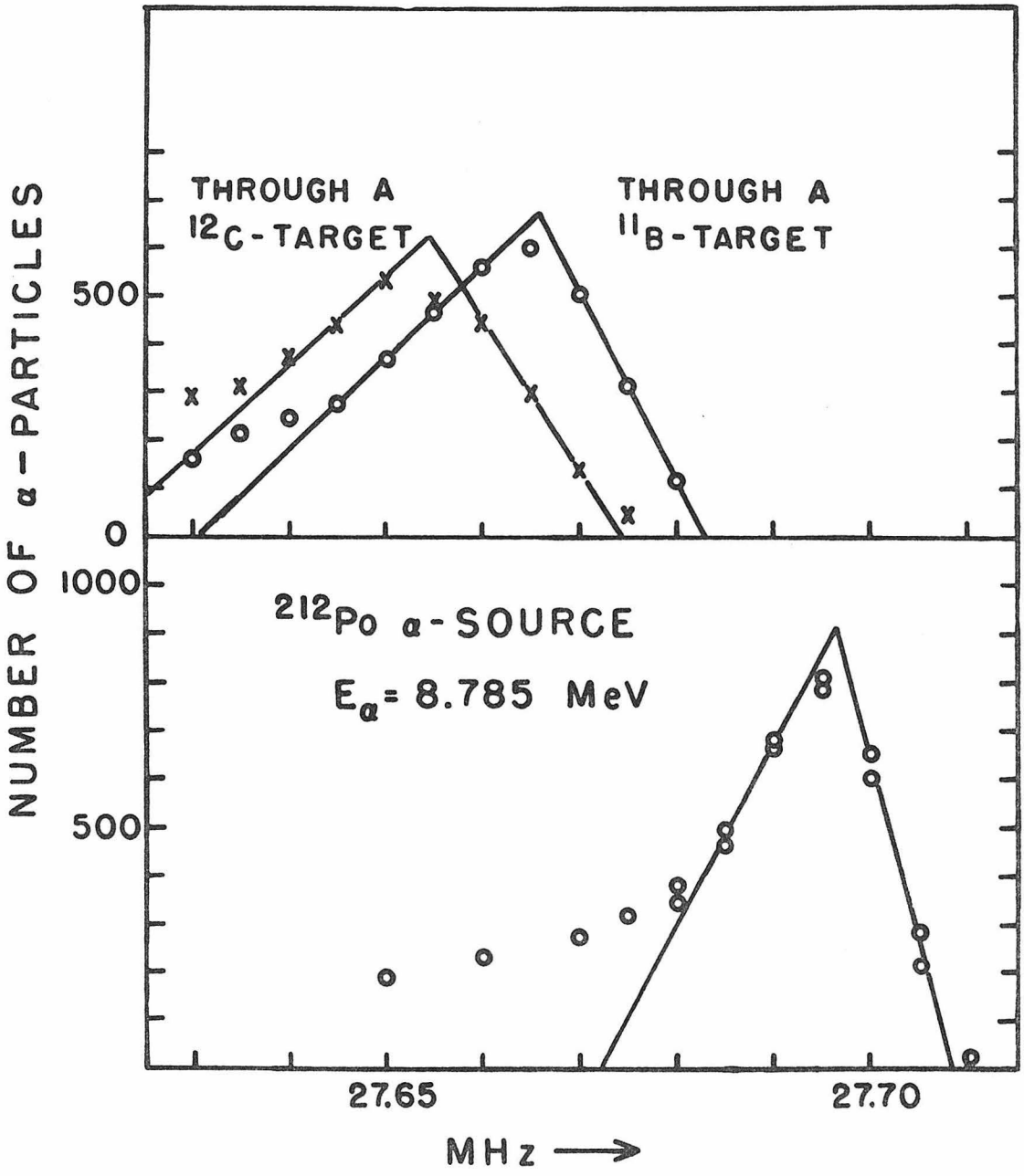
THROUGH A
^{12}C-TARGET
THROUGH A
^{11}B-TARGET
NUMBER OF α-PARTICLES
500
0
1000
500
^{212}Po α-SOURCE
E_α = 8.785 MeV
27.65
27.70
MHz

FIGURE 3

Spectra of the elastic scattering of ^{3}He particles on the ^{12}C and ^{16}O in a carbon-backed WO_3 target. The energy losses of the ^{3}He particles in the carbon backing and in the WO_3 target can be obtained from the observed shifts of the peaks in the middle and lowest spectra, respectively. See Section C of Chapter II for additional details concerning the significance of these spectra in the measurement of targets.

FIGURE 3

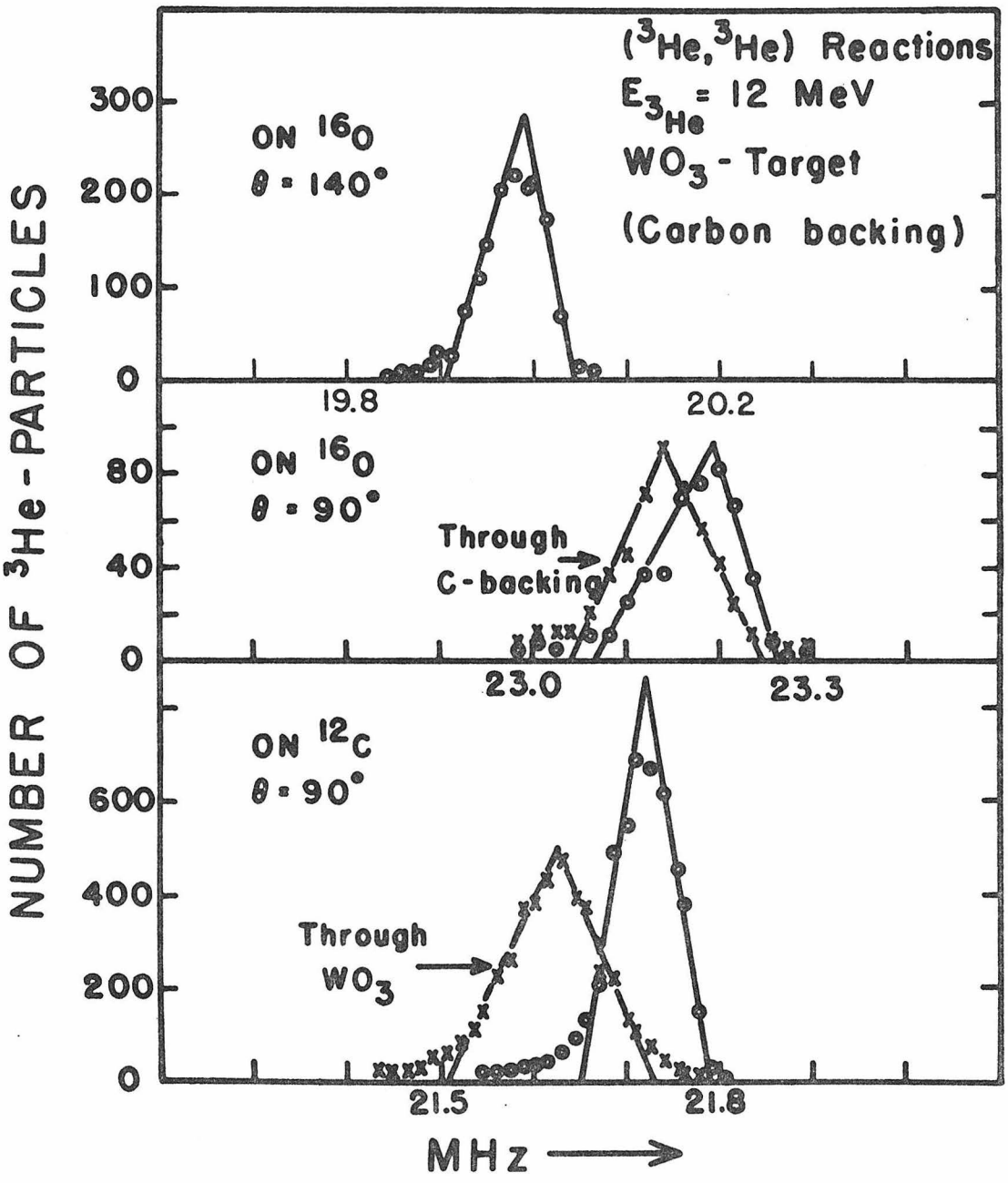
(3He,3He) Reactions
E3He = 12 MeV
WO3 - Target
(Carbon backing)
ON 16O
θ = 140°
ON 16O
θ = 90°
Through
C-backing
ON 12C
θ = 90°
Through
WO3
NUMBER OF 3He-PARTICLES
MHz
300
200
100
0
80
40
0
600
400
200
0
19.8
20.2
23.0
23.3
21.5
21.8

FIGURE 4

An energy-level diagram for ^{15}O taken from the report of Warburton, Olness, and Alburger (1965). All energies are in keV.

FIGURE 4

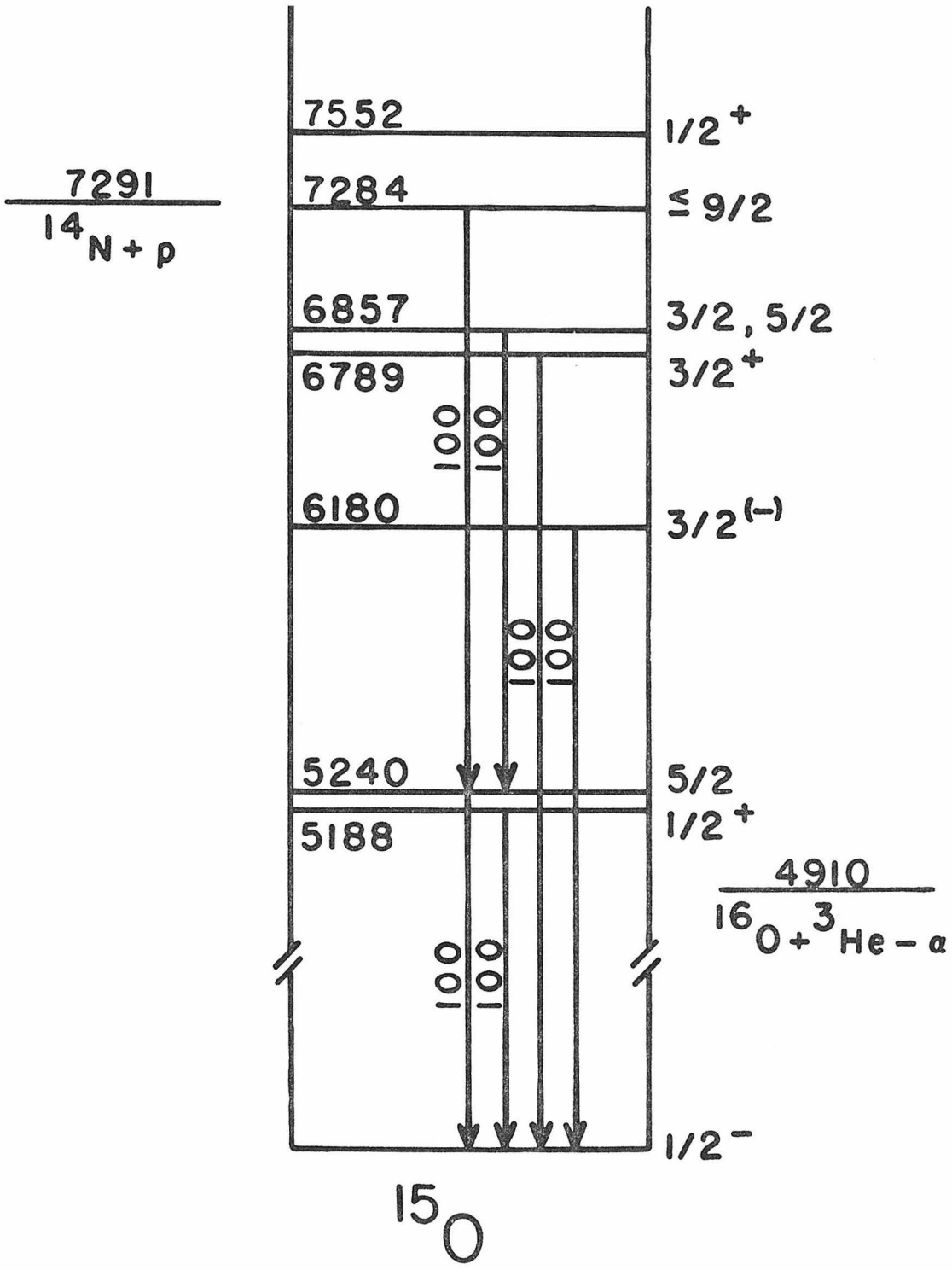
7552
1/2+
7291
14N + p
7284
≤ 9/2
6857
3/2, 5/2
6789
3/2+
6180
3/2(-)
5240
5/2
5188
1/2+
4910
16O + 3He - α
1/2-
15O

FIGURE 5

An α-particle spectrum from the (^{3}He, α) reaction on a SiO target. Groups corresponding to states in ^{15}O are identified by the excitation energies in MeV; other groups are marked according to the final nucleus. The distortion in the spectrum near 26.25 MHz is a result of the large yield at that frequency of ^{3}He particles from the ^{16}O(^{3}He, ^{3}He)^{16}O reaction; the ^{3}He group was so large that it was impossible to correctly separate the ^{3}He and α particles in the array detectors. See pages 13ff for additional details.

FIGURE 5

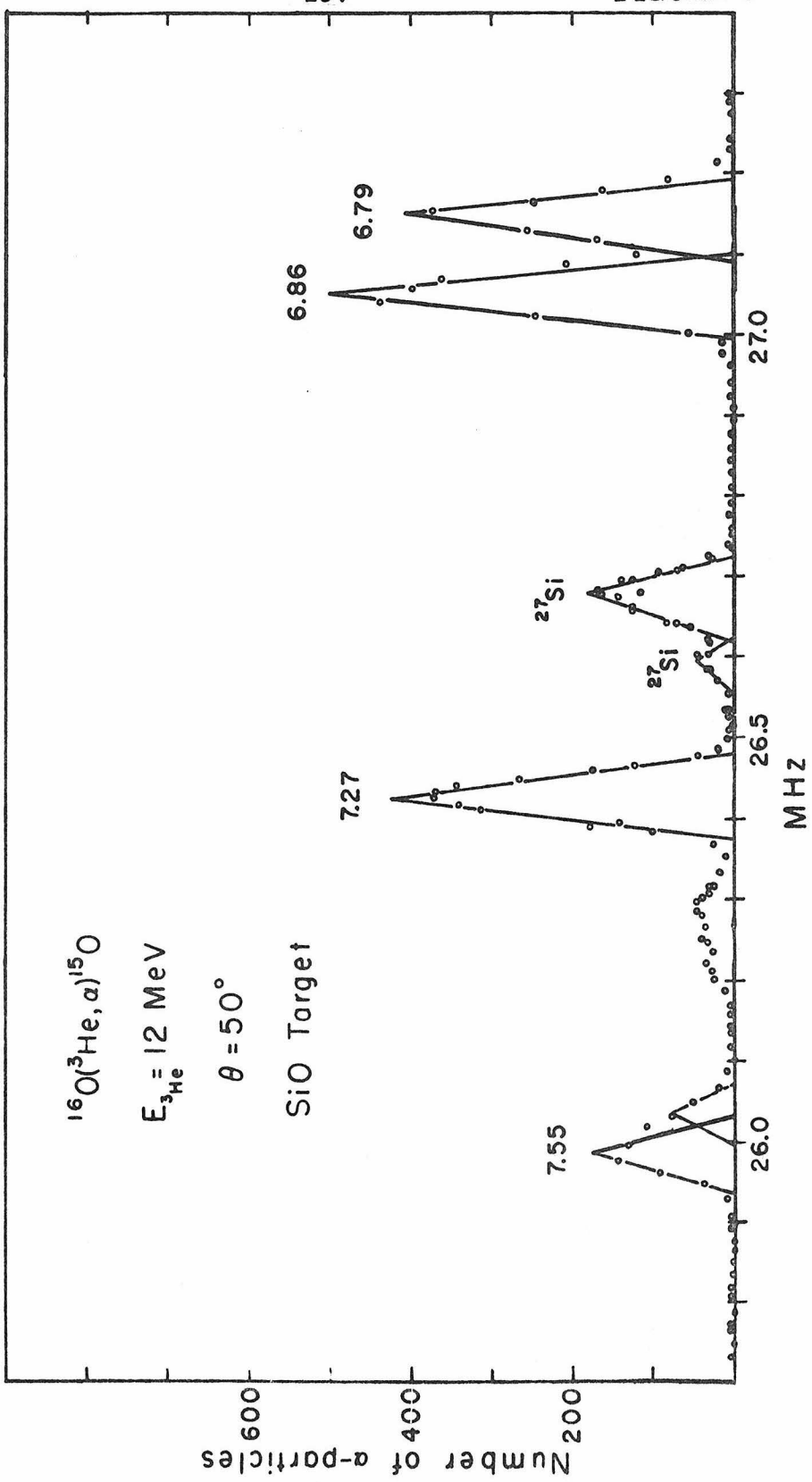
$^{16}O(^3He,\alpha)^{15}O$
$E_{^3He} = 12$ MeV
$\theta = 50°$
SiO Target
7.55
7.27
6.86
6.79
^{27}Si
^{27}Si
26.0
26.5
27.0
MHz
Number of α-particles
200
400
600

FIGURE 6

An α-particle spectrum from the $^{16}O(^{3}He, \alpha)$ reaction on a carbon-backed WO_3 target. Groups corresponding to states in ^{15}O are identified by the excitation energies in MeV. The gap in the spectrum at 26.25 MHz results from the intense elastic scattering of the beam on ^{16}O in the target (see the discussion for Figure 5). For additional details, see page 14.

FIGURE 6

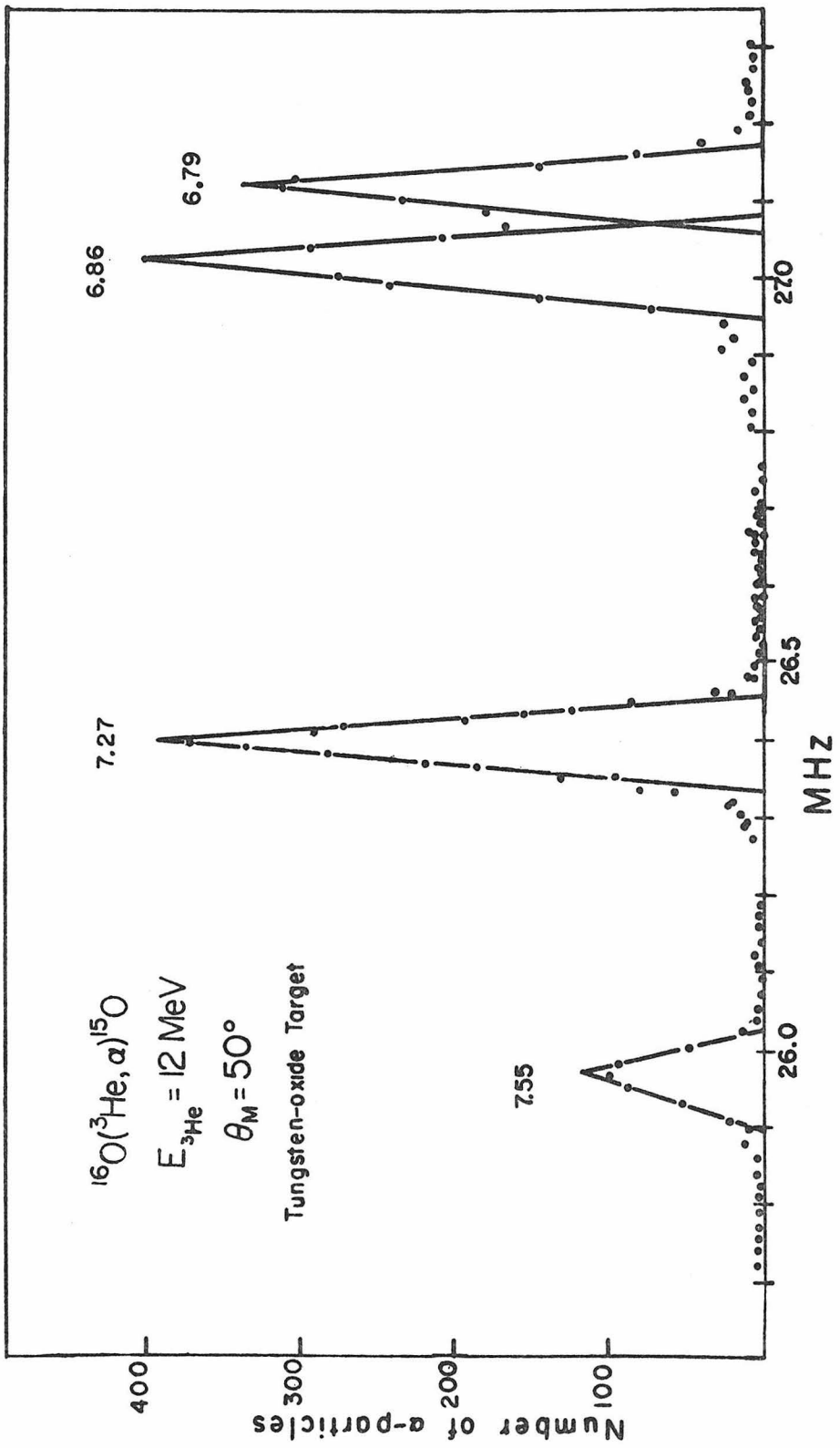
$^{16}O(^3He, \alpha)^{15}O$
$E_{^3He} = 12$ MeV
$\theta_M = 50°$
Tungsten-oxide Target
7.55
7.27
6.86
6.79
26.0
26.5
27.0
MHz
Number of α-particles
100
200
300
400

FIGURE 7

An α-particle spectrum from the $^{16}O(^{3}He, \alpha)$ reaction on an NiO target. Groups for all of the states of ^{15}O studied in the present work appear in this spectrum; they are identified by the corresponding excitation energies in MeV. The positions where the ^{3}He-particle groups from the elastic scattering on the ^{16}O and Ni in the target would lie are indicated in the figure. (See the discussion for Figure 5.)

For additional details concerning the significance of this spectrum, see pages 16 and 17.

FIGURE 7

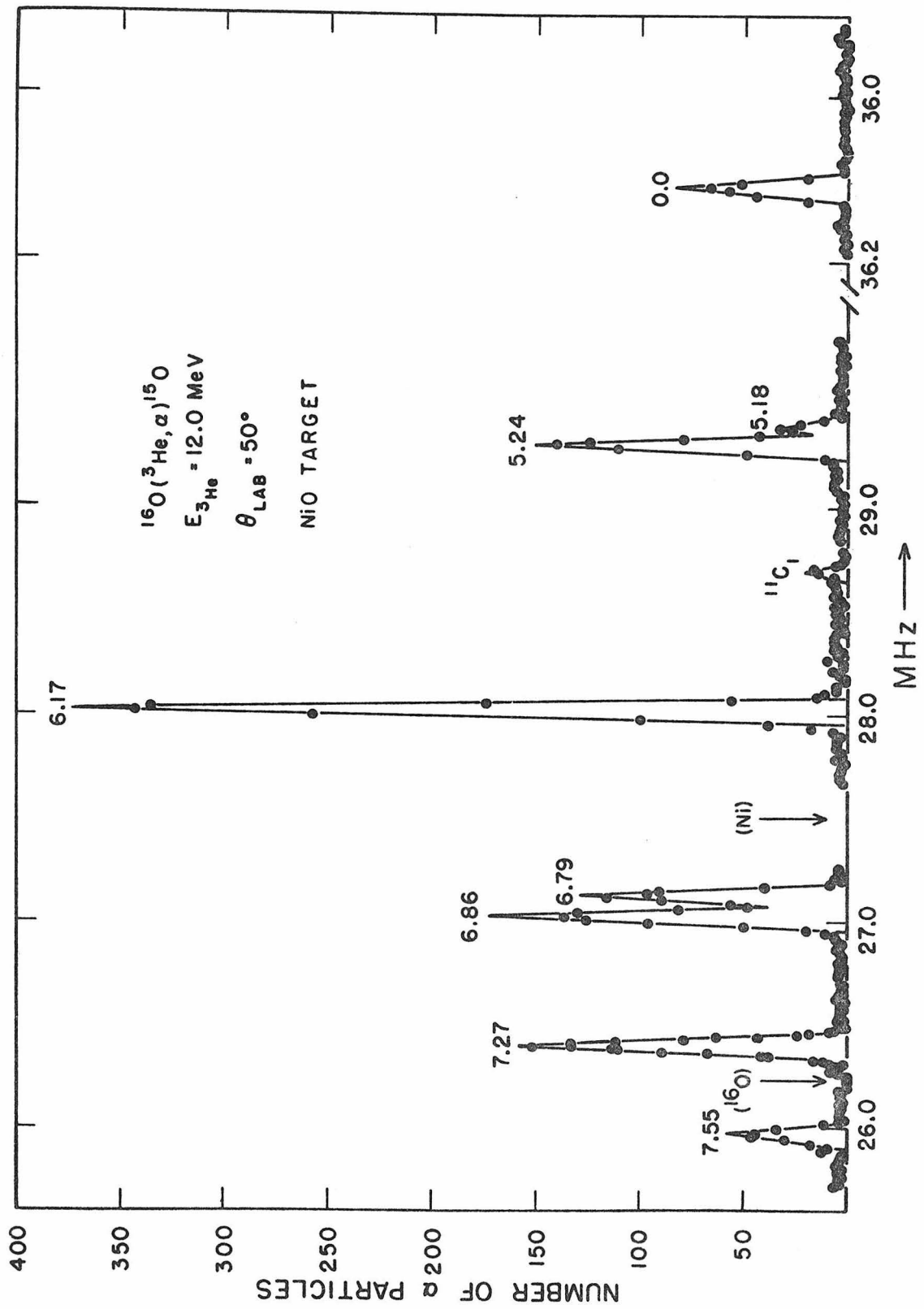
$^{16}O(^3He,\alpha)^{15}O$
$E_{^3He}$ = 12.0 MeV
θ_{LAB} = 50°
NiO TARGET
6.17
5.24
5.18
0.0
$^{11}C_1$
(Ni)
6.86
6.79
7.27
(^{16}O)
7.55
NUMBER OF α PARTICLES
MHz
400
350
300
250
200
150
100
50
26.0
27.0
28.0
29.0
36.2
36.0

FIGURE 8

An α-particle spectrum from the $^{16}O(^{3}He, \alpha)$ reaction on a NiO target. All of the bound states of ^{15}O are represented in this spectrum, and the groups are identified by the corresponding excitation energies in MeV. See page 16.

FIGURE 8

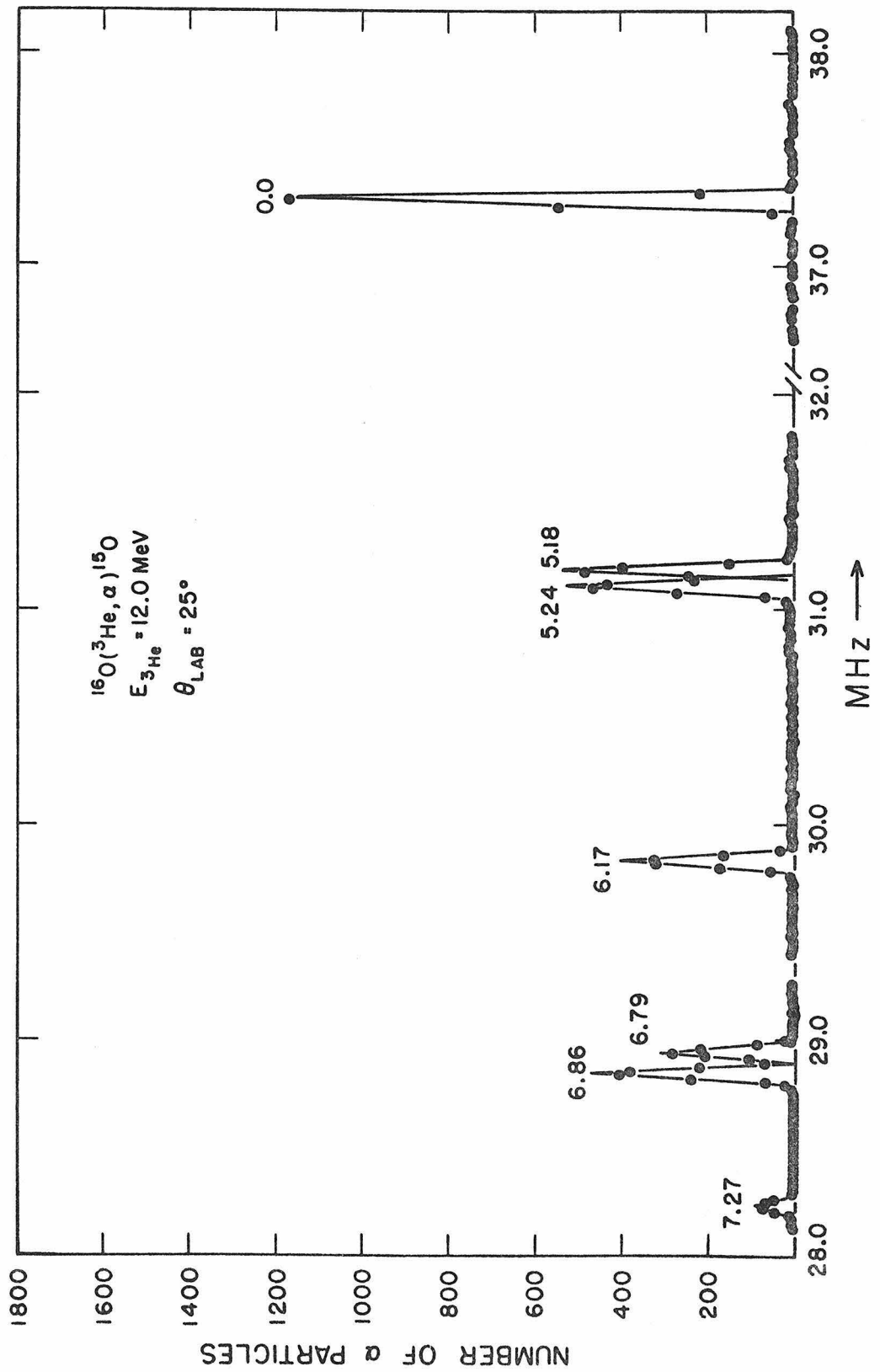
$^{16}O(^3He,\alpha)^{15}O$
$E_{^3He}$ = 12.0 MeV
θ_{LAB} = 25°
0.0
5.24
5.18
6.17
6.86
6.79
7.27
NUMBER OF α PARTICLES
MHz
1800
1600
1400
1200
1000
800
600
400
200
28.0
29.0
30.0
31.0
32.0
37.0
38.0

FIGURE 9

Angular distributions from the $^{16}O(^{3}He, \alpha)$ reaction to the ground state and 3rd excited state of ^{15}O. The data were taken at lab angles from 5^{o} to 70^{o} with the 16-counter array and were then checked and extended to larger angles with a position-sensitive detector. In addition to the indicated probable errors, there is a further uncertainty of about 10% in the absolute normalization.

For additional details, see pages 21 and 22.

FIGURE 9

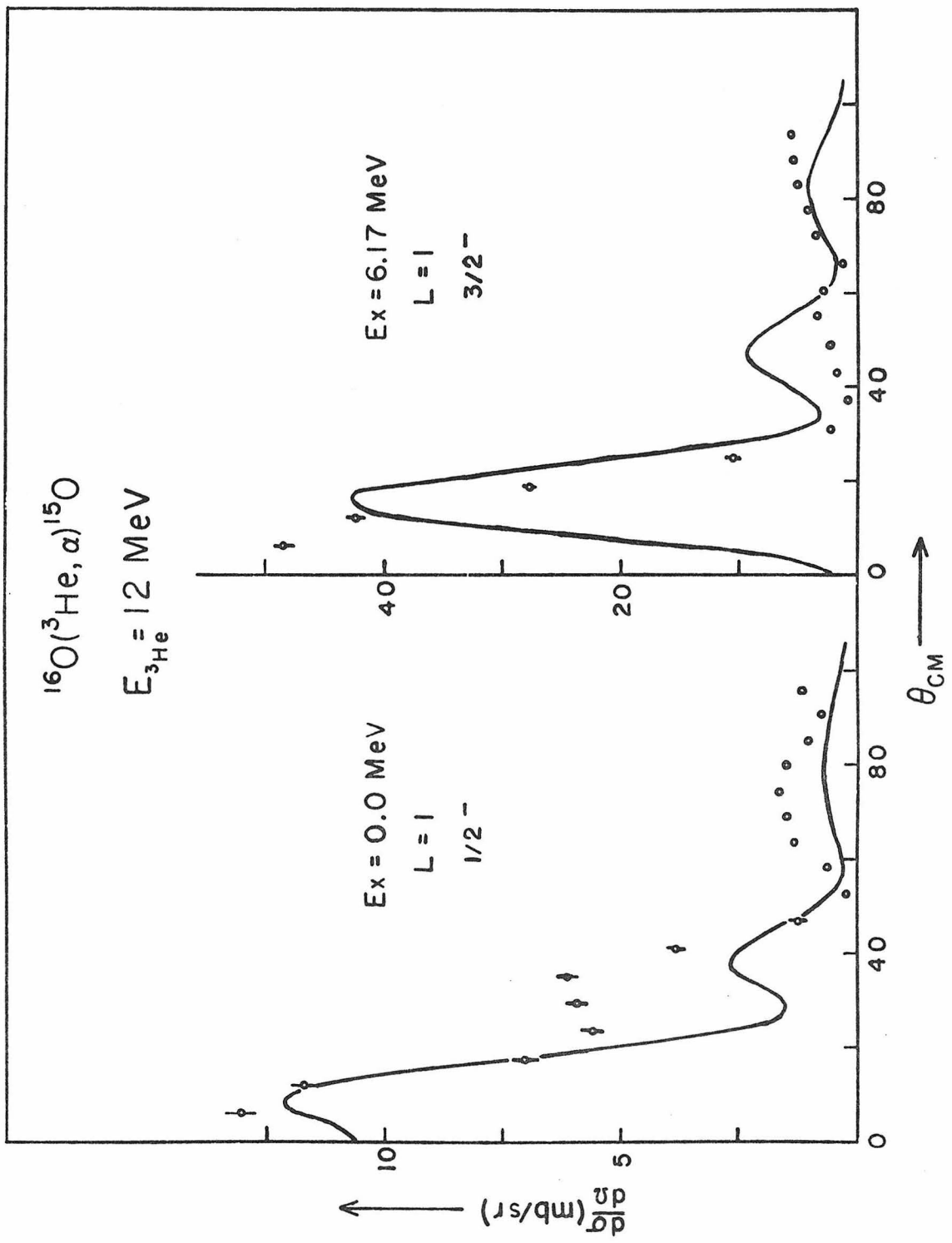
$^{16}O(^3He,\alpha)^{15}O$
$E_{^3He}$ = 12 MeV
Ex = 0.0 MeV
L = 1
1/2⁻
Ex = 6.17 MeV
L = 1
3/2⁻
$\frac{d\sigma}{d\Omega}$(mb/sr)
θ_{CM}
0
40
80
5
10
20
40

FIGURE 10

Angular distributions from the $^{16}O(^{3}He, \alpha)$ reaction for the ground state and 3rd excited state of ^{15}O; the incident energy was 10 MeV. The data were taken mainly on the small ^{16}O contamination in Ni^{18}O targets, and the probable-error bars include the affect of the α-particle background from the $^{18}O(^{3}He, \alpha)$ reaction. There is an additional uncertainty of 15% in the absolute normalization. For further details, see page 22.

FIGURE 10

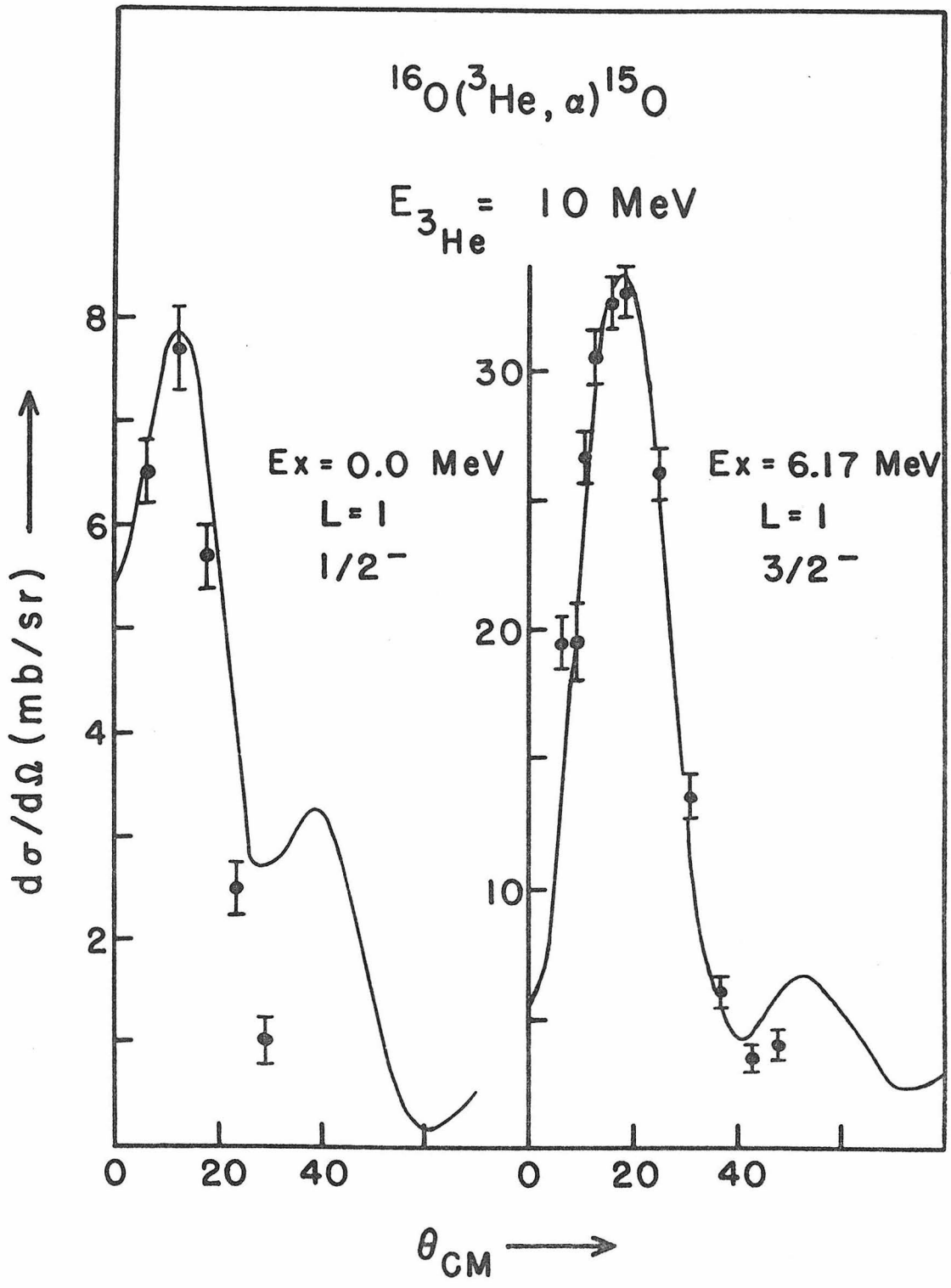
$^{16}O(^{3}He, \alpha)^{15}O$
$E_{^{3}He}$ = 10 MeV
Ex = 0.0 MeV
L = 1
1/2⁻
Ex = 6.17 MeV
L = 1
3/2⁻
dσ/dΩ (mb/sr)
θ_{CM}
0
20
40
2
4
6
8
10
20
30

FIGURE 11

Angular distributions from the $^{16}O(^{3}He, \alpha)$ reaction for the 1^{st}, 2^{nd}, 3^{rd}, 4^{th}, and 5^{th} excited states of ^{15}O. In addition to the probable-error bars indicated in the figure, there is an uncertainty of about 10% in the absolute normalization. For further details, see page 22.

FIGURE 11

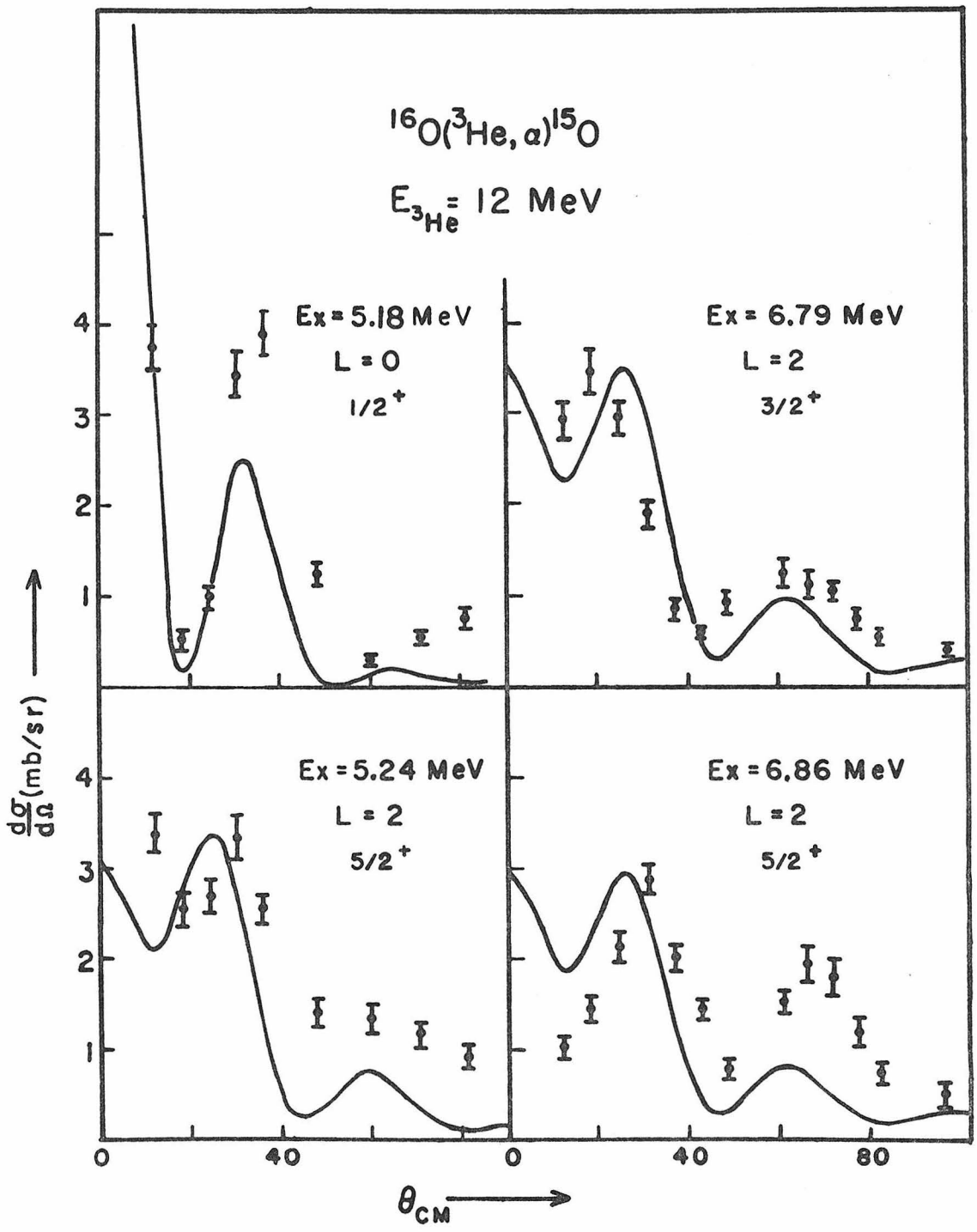
$^{16}O(^{3}He, \alpha)^{15}O$
$E_{^{3}He}$ = 12 MeV
Ex = 5.18 MeV
L = 0
1/2+
Ex = 6.79 MeV
L = 2
3/2+
Ex = 5.24 MeV
L = 2
5/2+
Ex = 6.86 MeV
L = 2
5/2+
$\frac{d\sigma}{d\Omega}$(mb/sr)
θ_{CM}
0
40
80
1
2
3
4

FIGURE 12

The angular distribution from the $^{16}O(^{3}He, \alpha)$ reaction for the 6th excited state of ^{15}O. In addition to the probable-error bars indicated in the figure, there is an uncertainty of about 10% in the absolute normalization. The smooth curve in the figure is the prediction of the DWBA theory (see Appendix IV) for an $\ell_n = 4$ angular distribution; the dashed curve gives the prediction of a PWBA theory for an $\ell_n = 4$ distribution. The cut-off radius for the PWBA theory was chosen to give the best fit to the data; the cut-off radii giving the best fits to the angular distributions for the other bound states of ^{15}O were between 6.5f and 7.25f. For additional details, see pages 22 and 23.

FIGURE 12

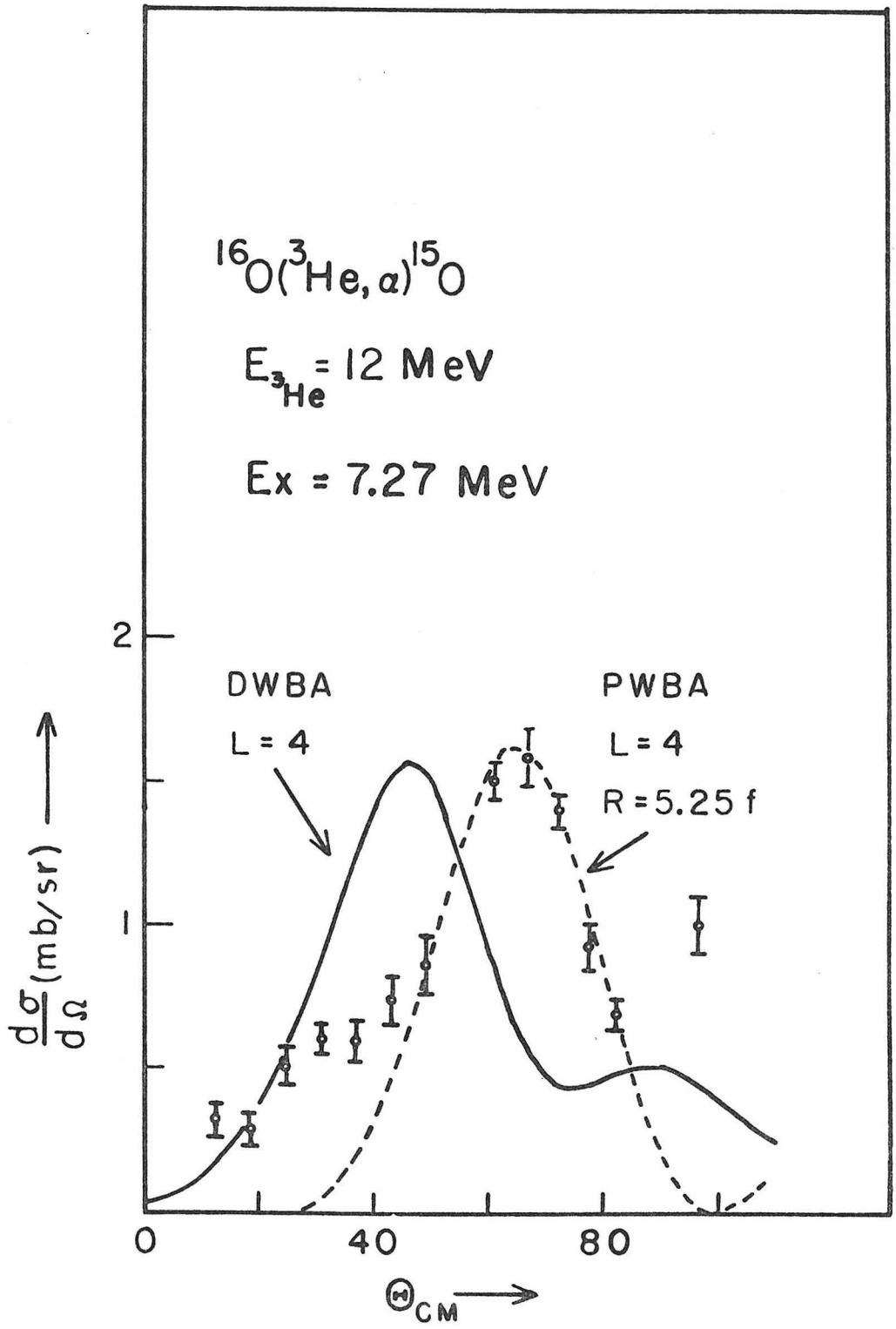
$^{16}O(^{3}He,\alpha)^{15}O$
$E_{^{3}He}$ = 12 MeV
Ex = 7.27 MeV
DWBA
L = 4
PWBA
L = 4
R = 5.25 f
2
1
0
40
80
$\frac{d\sigma}{d\Omega}$ (mb/sr)
Θ_{CM}

FIGURE 13

The α-γ angular correlations for all of the bound, excited states of ^{15}O, except the 1^{st} excited state; the α particles from the $^{16}O(^{3}He, \alpha)^{15}O^{*}$ reaction were detected at 0^{o}, and the coincident, de-exciting γ rays were measured at angles of 90^{o}, 120^{o}, 135^{o}, and 150^{o}, with respect to the beam direction. No attempt was made to obtain absolute cross-sections; hence branching ratios for the cascade decays should not be inferred from the figure.

The smooth lines are the predictions of the theory (see Appendix V) for the final choice of spins for the various states; the Legendre polynomial coefficients given by the theory for the best fits to the data are given in Table VII.

For additional details, see pages 23 through 28.

FIGURE 13

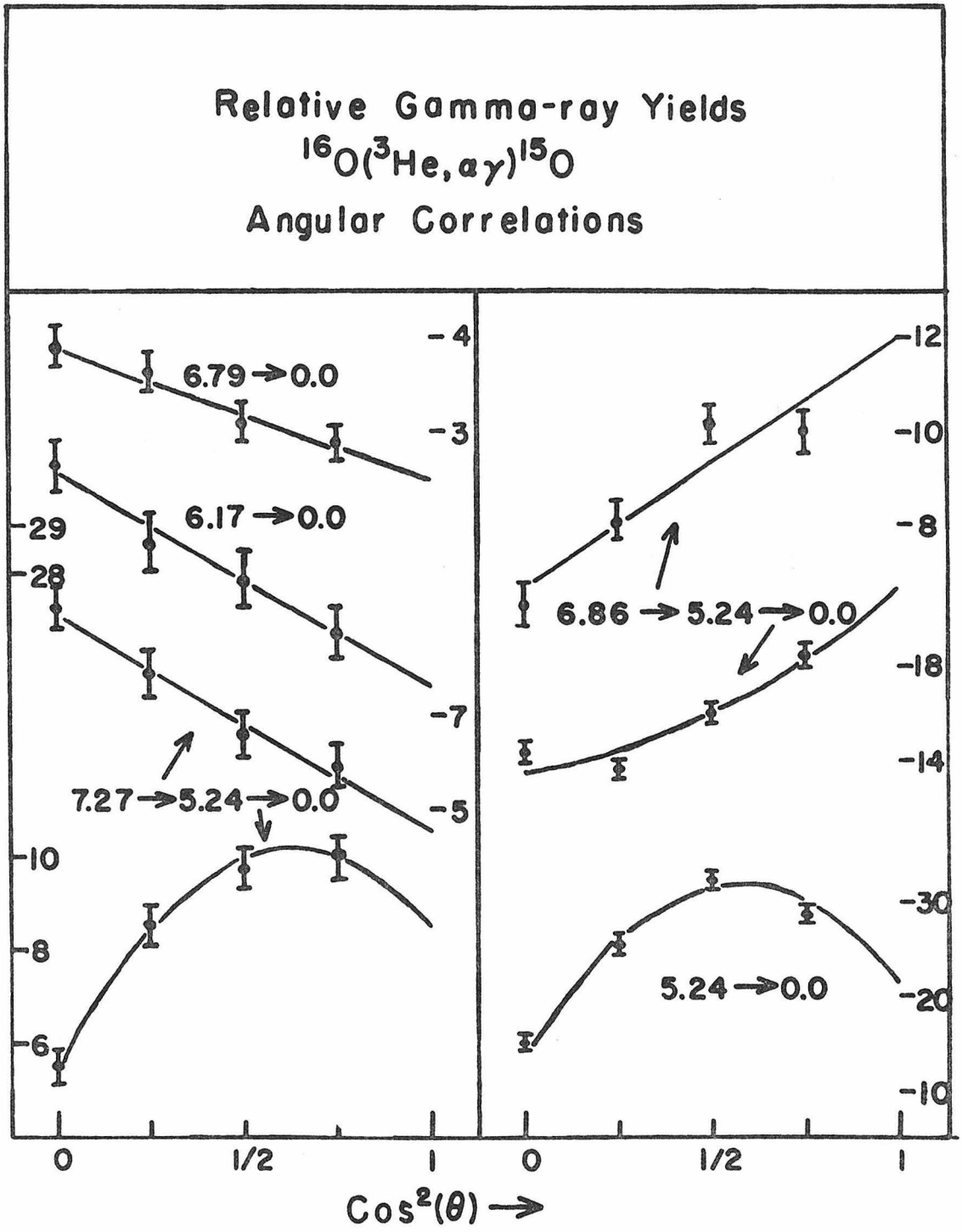
Relative Gamma-ray Yields
$^{16}O(^{3}He,\alpha\gamma)^{15}O$
Angular Correlations
6.79 → 0.0
6.17 → 0.0
7.27 → 5.24 → 0.0
6.86 → 5.24 → 0.0
5.24 → 0.0
-4
-3
-29
-28
-7
-5
-10
-8
-6
-12
-10
-8
-18
-14
-30
-20
-10
0
1/2
1
0
1/2
1
Cos²(θ) →

FIGURE 14

The Q^2 analysis of the angular correlation of the γ-ray decay of the 2^{nd} excited state of ^{15}O to the ground state. Spin combinations whose corresponding Q^2 did not fall below the 0.1% limit were rejected in this work; thus, of the four spin combinations considered in this analysis, only the spin combination of 5/2 to 1/2 was not rejected. (See page 26.)

For additional details concerning the Q^2 analysis, see pages 23 ff.

FIGURE 14

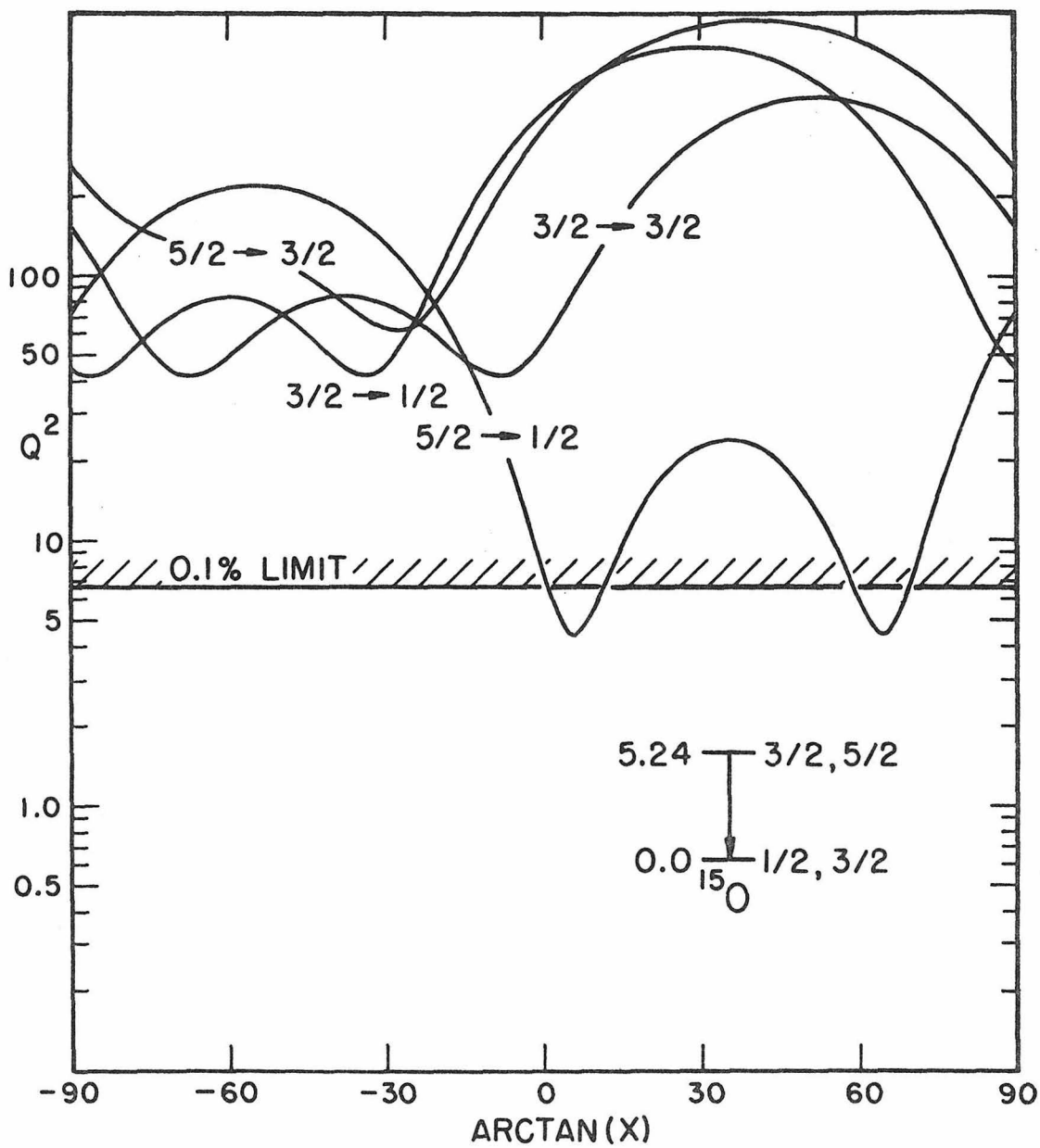
5/2 → 3/2
3/2 → 3/2
3/2 → 1/2
5/2 → 1/2
0.1% LIMIT
100
50
10
5
1.0
0.5
Q^2
5.24 — 3/2, 5/2
0.0 — 1/2, 3/2
^{15}O
-90
-60
-30
0
30
60
90
ARCTAN (X)

FIGURE 15

A γ-ray spectrum for the γ-ray decay of the 6^{th} excited state of ^{15}O. The random-coincidence background (see pages 10 and 11) has already been subtracted; the non-zero yield above 5.24 MeV is probably an indication of pulse pile-up in the γ-ray detector. (See pages 23 and 24.)

FIGURE 15

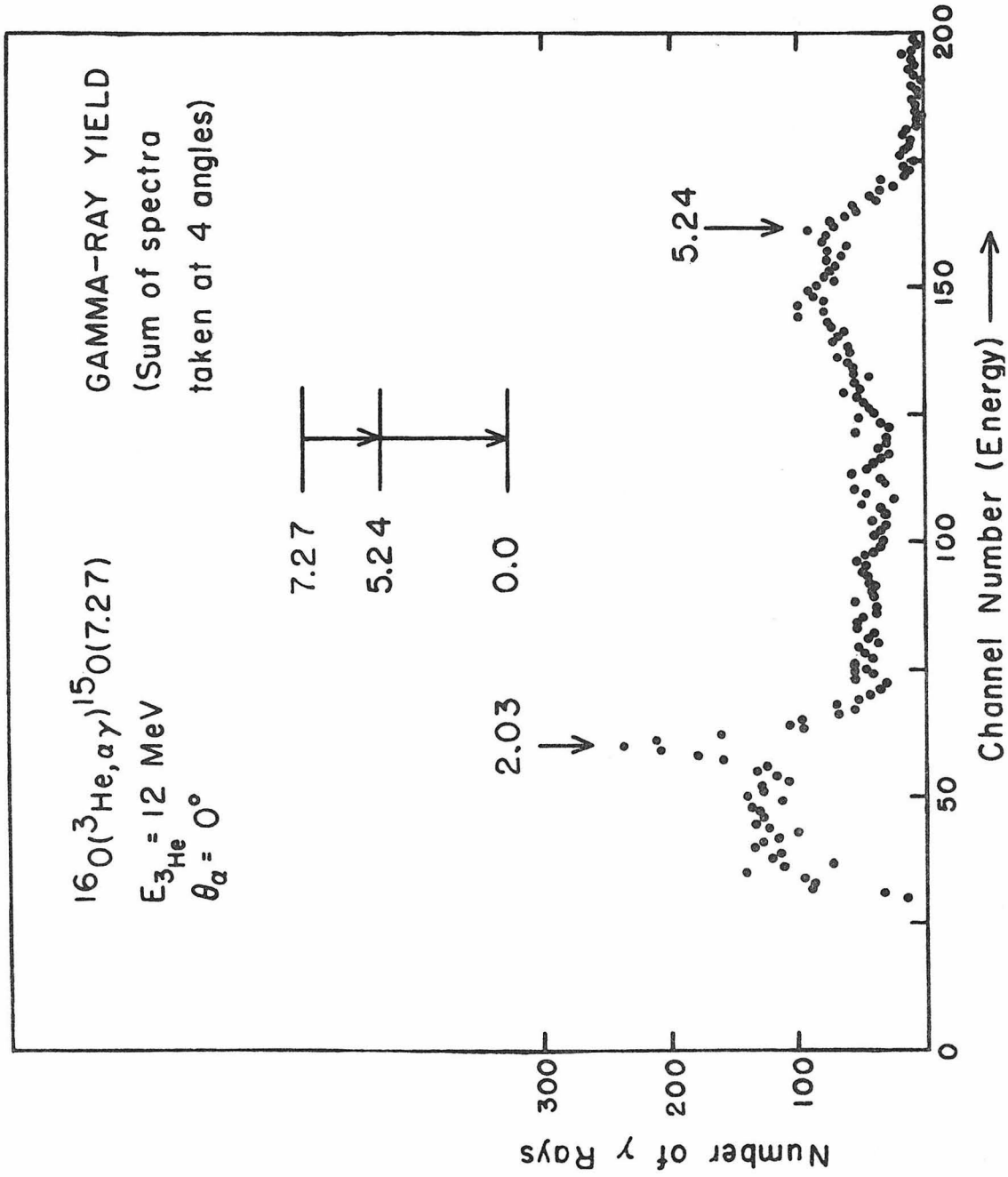
$^{16}O(^{3}He,\alpha\gamma)^{15}O(7.27)$
$E_{^{3}He}$ = 12 MeV
θ_{α} = 0°
GAMMA-RAY YIELD
(Sum of spectra
taken at 4 angles)
7.27
5.24
0.0
2.03
5.24
Number of γ Rays
Channel Number (Energy)
0
50
100
150
200
100
200
300

FIGURE 16

The Q^2 analysis of the α-γ angular correlation for the 4^{th} excited state of ^{15}O. A spin of 5/2 for this state was rejected because Q^2 for this spin does not fall below the 0.1% limit. (See pages 26 and 27.)

For additional details concerning the Q^2 analysis, see pages 23ff.

FIGURE 16

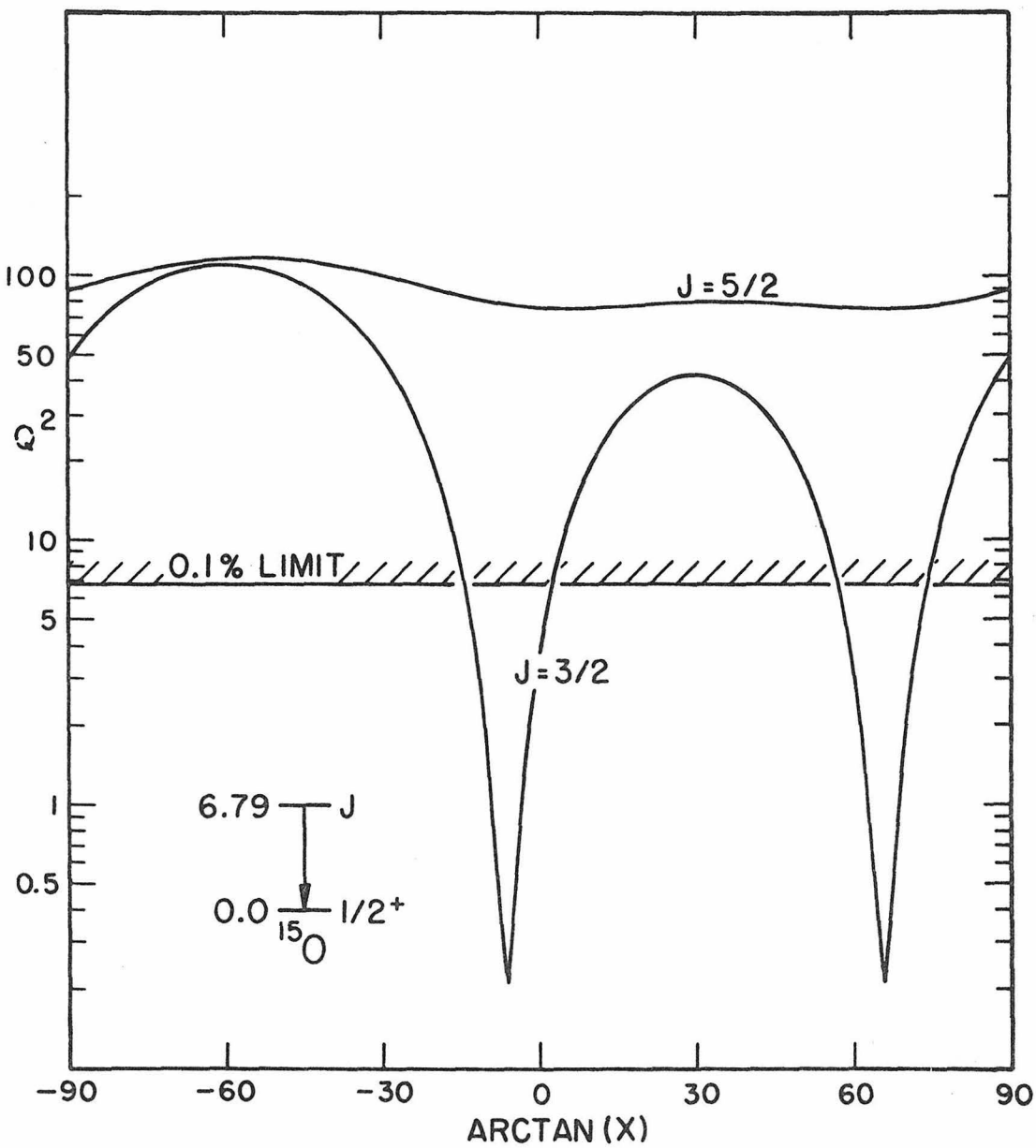
100
50
Q^2
10
5
1
0.5
J = 5/2
0.1% LIMIT
J = 3/2
6.79
J
0.0
^{15}O
1/2+
−90
−60
−30
0
30
60
90
ARCTAN (X)

FIGURE 17

The Q^2 analysis of the α-γ angular correlation for the γ-ray decay of the 5^{th} excited state of ^{15}O to the 2^{nd} excited state. Neither spin possibility could be rejected because both have Q^2 solutions falling below the 0.1% limit. (See page 27.)

For additional details concerning the Q^2 analysis, see pages 23ff.

FIGURE 17

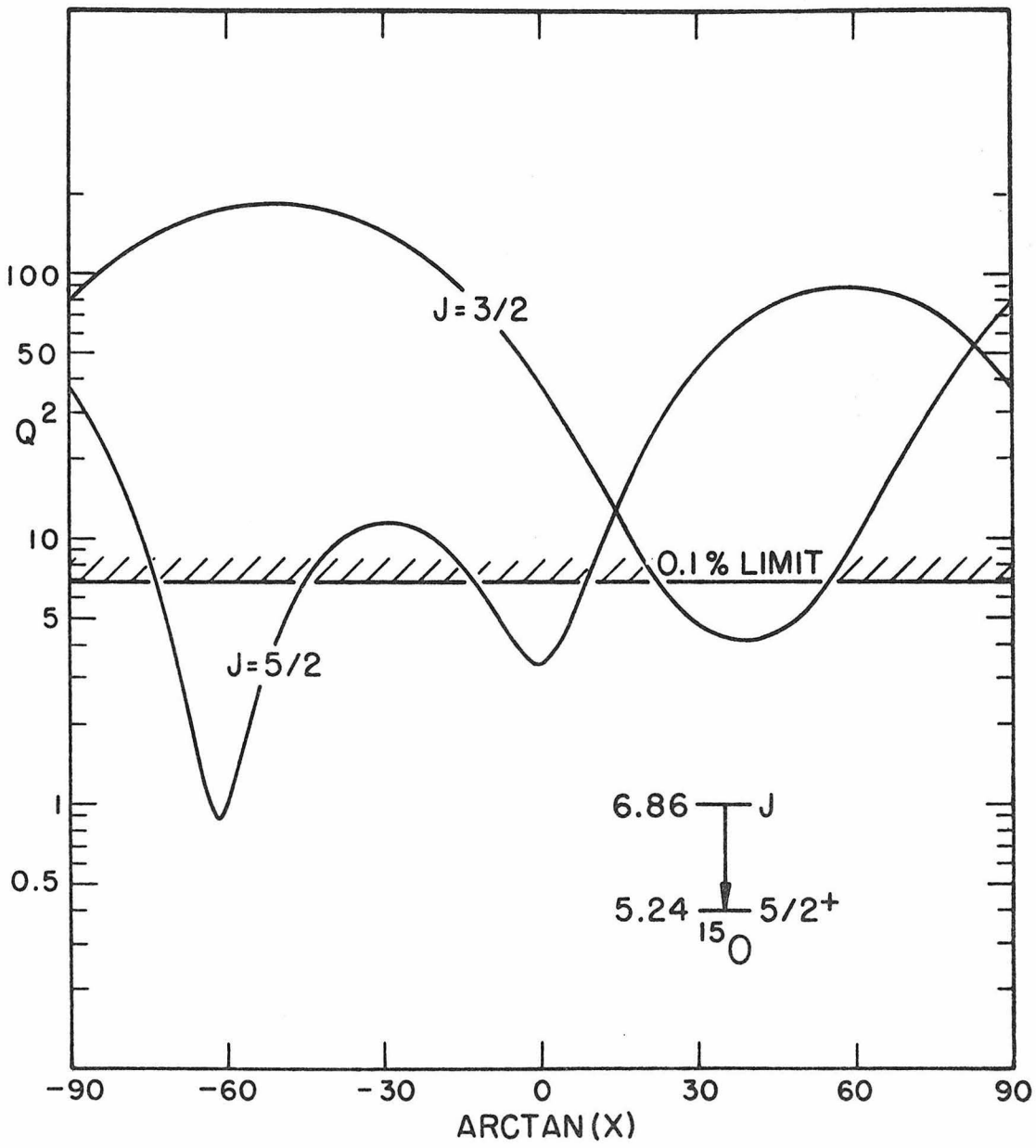
100
50
Q^2
10
5
1
0.5
J=3/2
J=5/2
0.1% LIMIT
6.86
J
5.24
5/2+
^{15}O
-90
-60
-30
0
30
60
90
ARCTAN(X)

FIGURE 18

A 2-dimensional Q^2 analysis of the α-γ angular correlation of the cascade γ-ray decay of the 5^{th} excited state of ^{15}O. The 0.1% limit in this figure corresponds to $Q^2 = 4.5$. A further restriction on a possible solution is that Q^2 fall below the 0.1% limit for values of X(2-3) indicated by the vertical dashed lines; this multipole mixing was measured previously (see Figure 14 and Table VIII). The significance of this analysis is discussed on page 27.

For additional details concerning the Q^2 analysis, see pages 23ff.

FIGURE 18

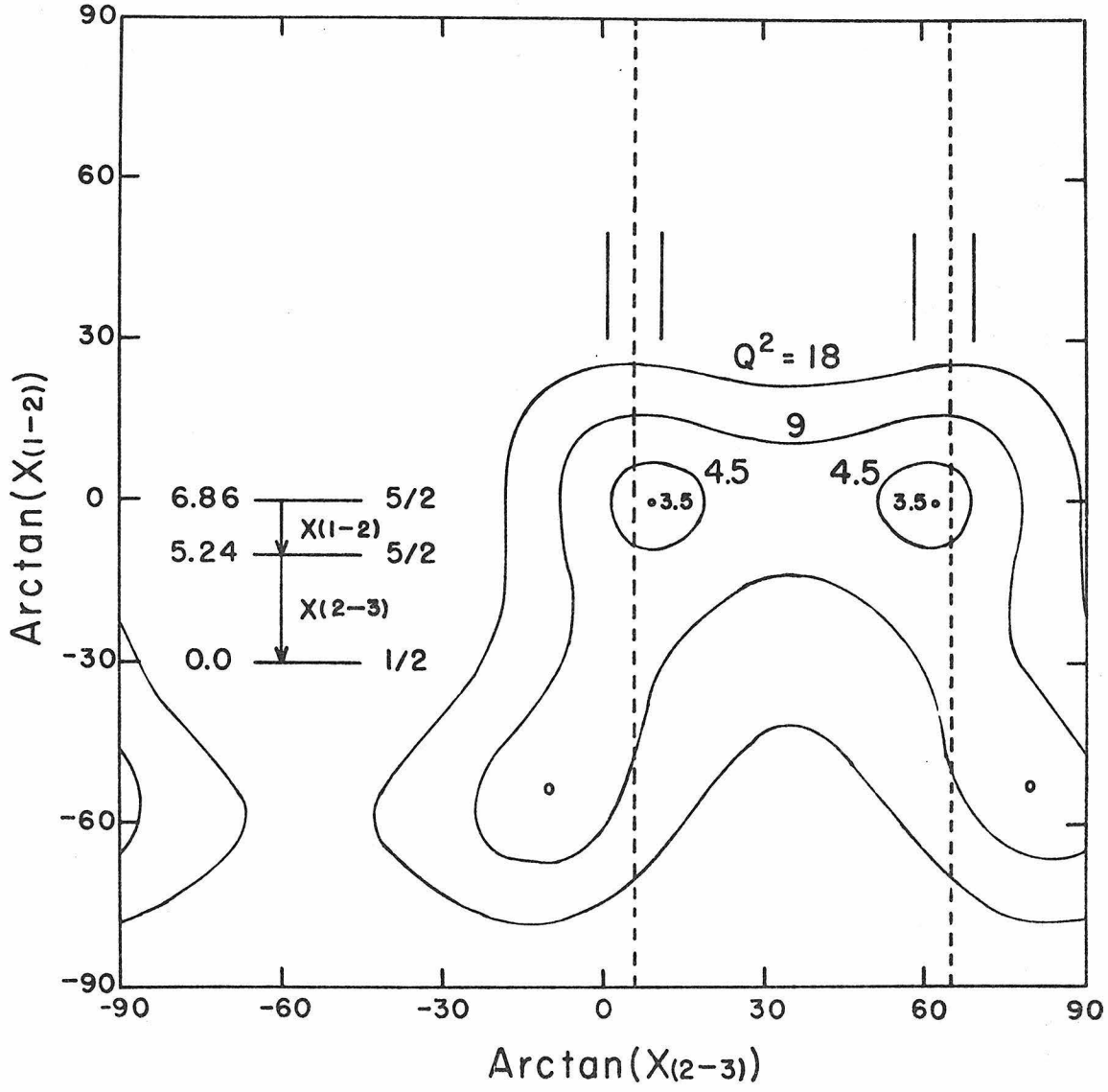
90
60
30
0
-30
-60
-90
-90
-60
-30
0
30
60
90
Arctan(X(1-2))
Arctan(X(2-3))
Q^2 = 18
9
4.5
4.5
3.5
3.5
6.86
5/2
X(1-2)
5.24
5/2
X(2-3)
0.0
1/2

FIGURE 19

A Q^2 analysis of the α-γ angular correlation of the 2^{nd} γ-ray from the cascade γ-ray decay of the 5^{th} excited state of ^{15}O. This Q^2 analysis is symmetric around 0^o. The significance of this analysis is discussed on page 27.

For additional details concerning the Q^2 analysis, see pages 23ff.

FIGURE 19

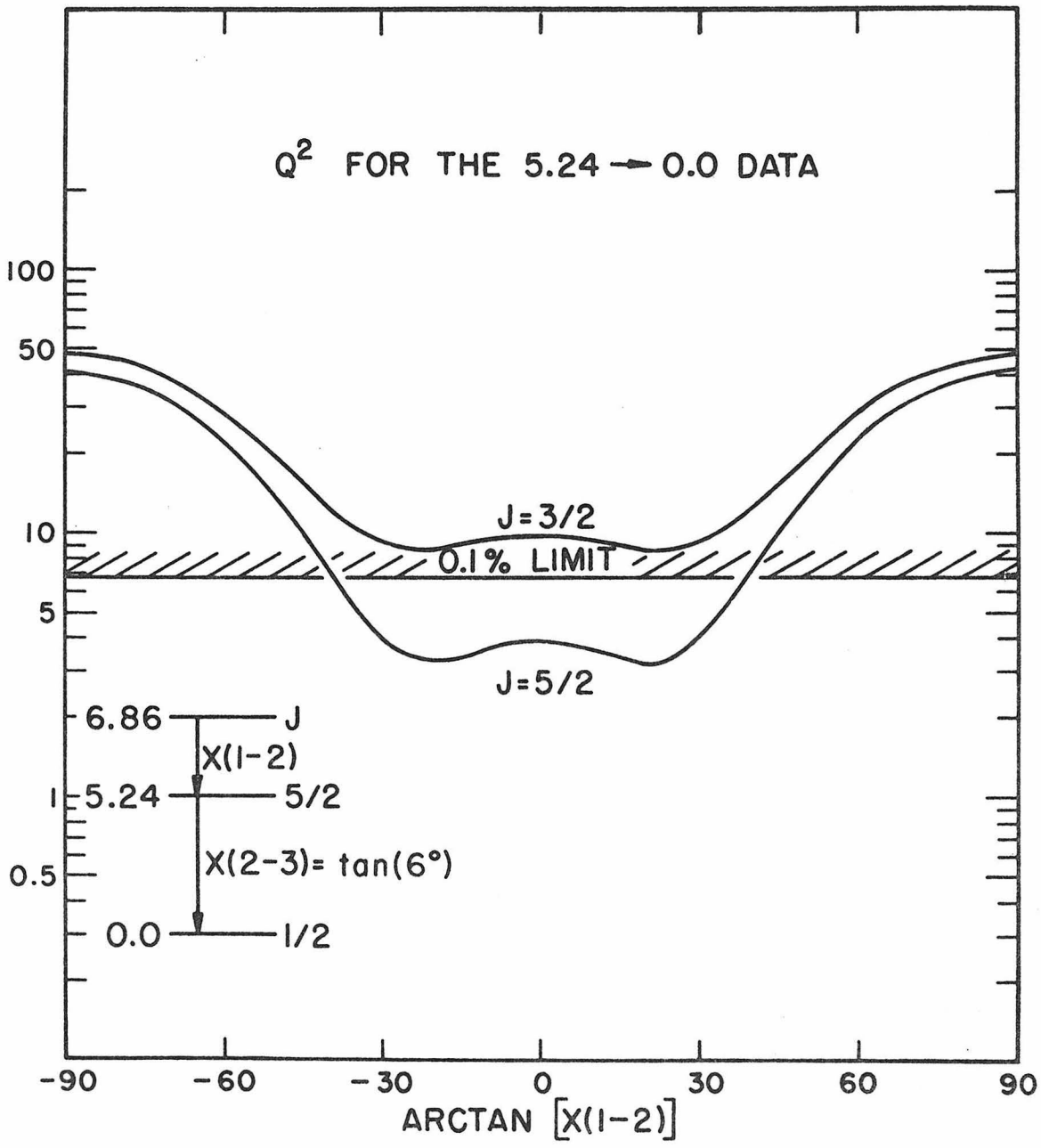
Q^2 FOR THE 5.24 → 0.0 DATA
100
50
10
5
1
0.5
J=3/2
0.1% LIMIT
J=5/2
6.86
J
X(1-2)
5.24
5/2
X(2-3)= tan(6°)
0.0
1/2
-90
-60
-30
0
30
60
90
ARCTAN [X(1-2)]

FIGURE 20

The Q^2 analysis of the α-γ angular correlation for the γ-ray decay of the 6^{th} excited state of ^{15}O to the 2^{nd} excited state. Spins of 1/2 and 9/2 for the 6th excited state can be excluded because Q^2 for these spins does not fall below the 0.1% limit. (See pages 27 and 28.)

For additional details concerning the Q^2 analysis, see pages 23ff.

FIGURE 20

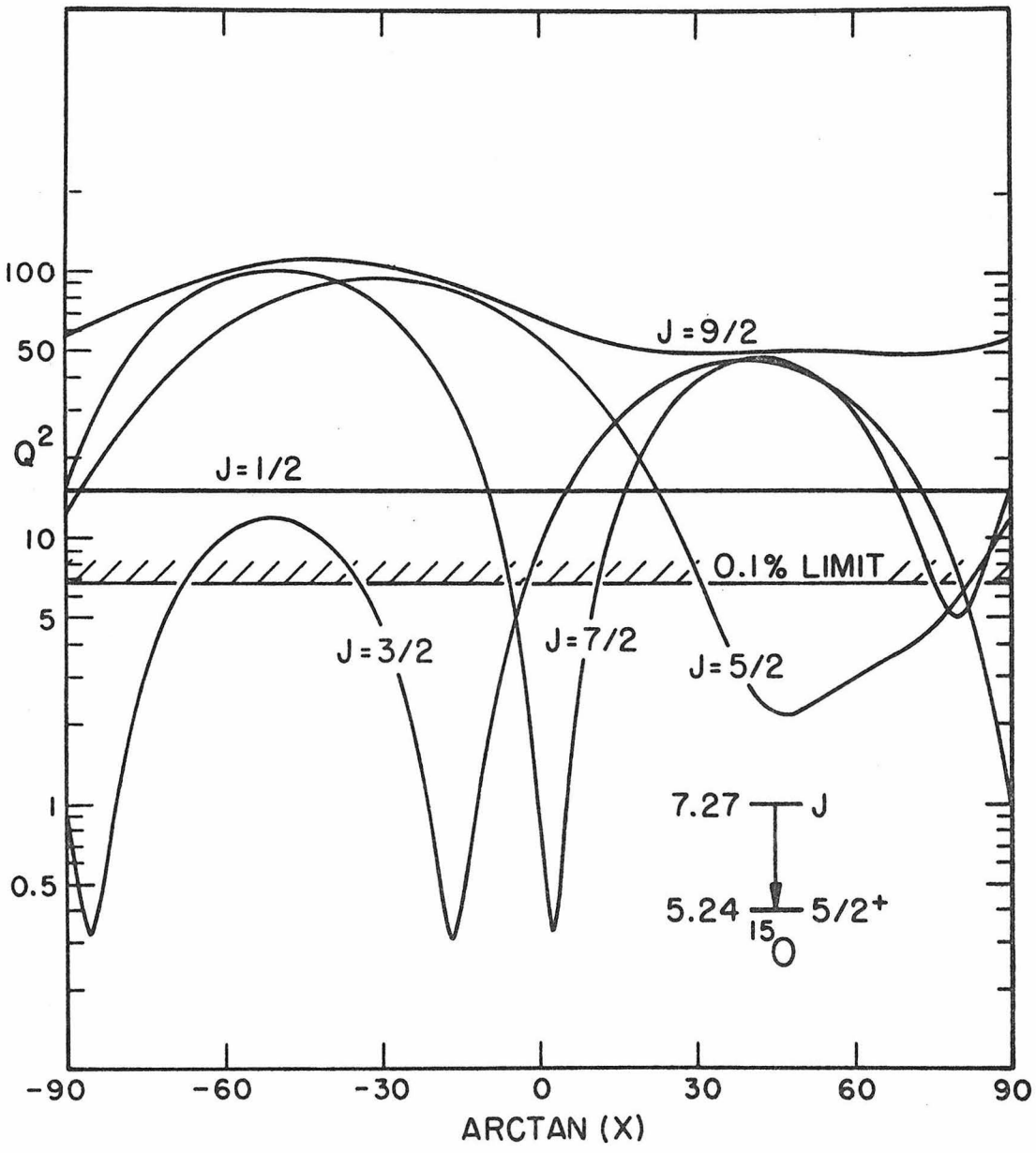
100
50
Q^2
10
5
1
0.5
J=9/2
J=1/2
0.1% LIMIT
J=3/2
J=7/2
J=5/2
7.27 J
5.24 5/2+
15O
-90
-60
-30
0
30
60
90
ARCTAN (X)

FIGURE 21

A Q^2 analysis of the α-γ angular correlation of the 2^{nd} γ-ray from the cascade γ-ray decay of the 6^{th} excited state of ^{15}O. This Q^2 analysis is symmetric about 0^o. The significance of this analysis is discussed on pages 27 and 28.

For additional details concerning the Q^2 analysis, see pages 23ff.

FIGURE 21

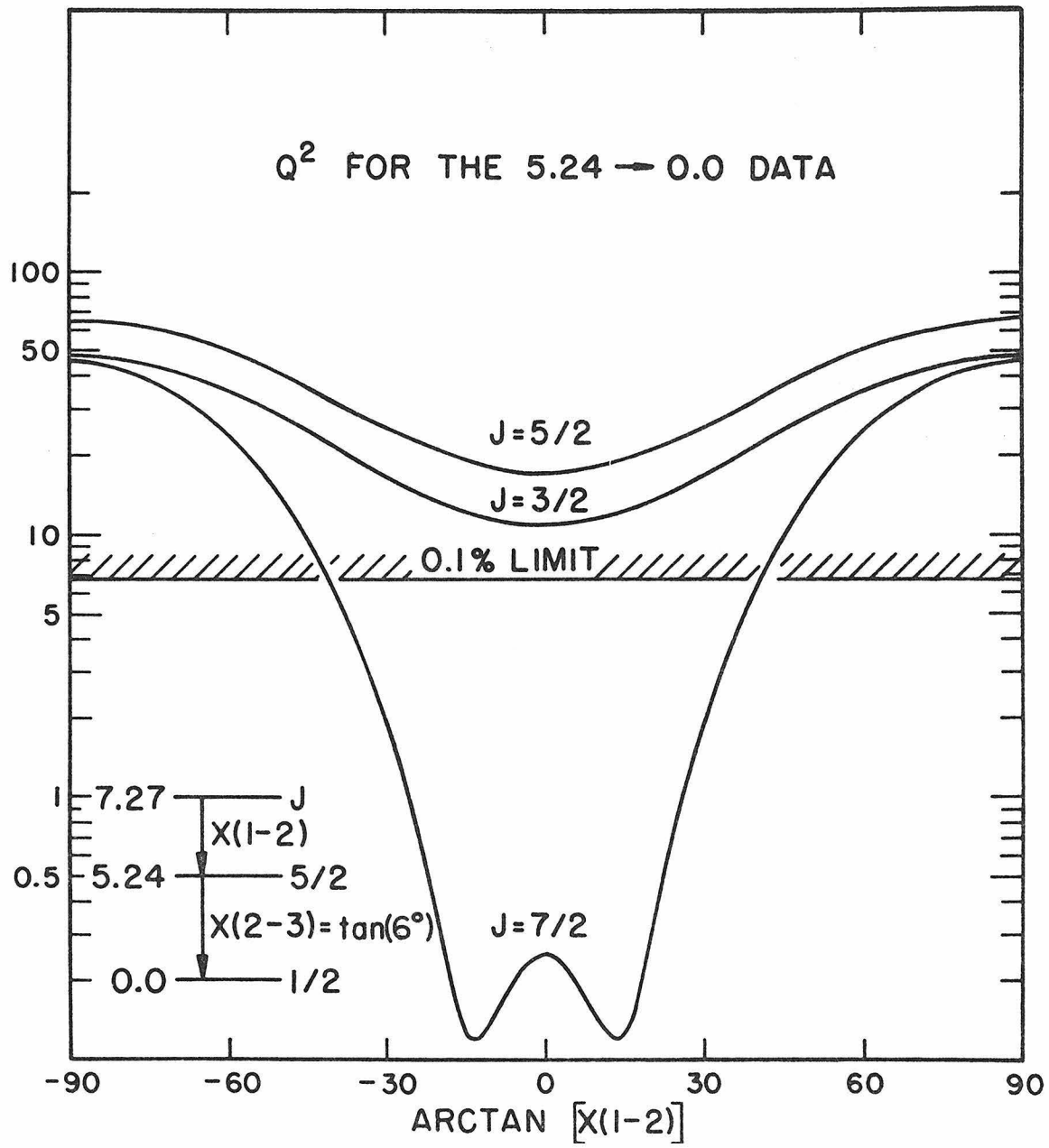
Q² FOR THE 5.24 → 0.0 DATA
100
50
10
5
1
0.5
J=5/2
J=3/2
0.1% LIMIT
7.27
J
X(1-2)
5.24
5/2
X(2-3)= tan(6°)
J=7/2
0.0
1/2
-90
-60
-30
0
30
60
90
ARCTAN [X(1-2)]

FIGURE 22

A 2-dimensional Q^2 analysis of the α-γ angular correlation of the cascade γ-ray decay of the 6^{th} excited state of ^{15}O. The 0.1% limit in this figure comes for $Q^2 = 4.5$. A further restriction on a possible solution is that Q^2 fall below the 0.1% limit for values of X(2-3) indicated by the vertical dashed lines; this multipole mixing was measured previously (see Figure 14 and Table VIII). The significance of this analysis is discussed on pages 27 and 28.

For additional details concerning the Q^2 analysis, see pages 23ff.

FIGURE 22

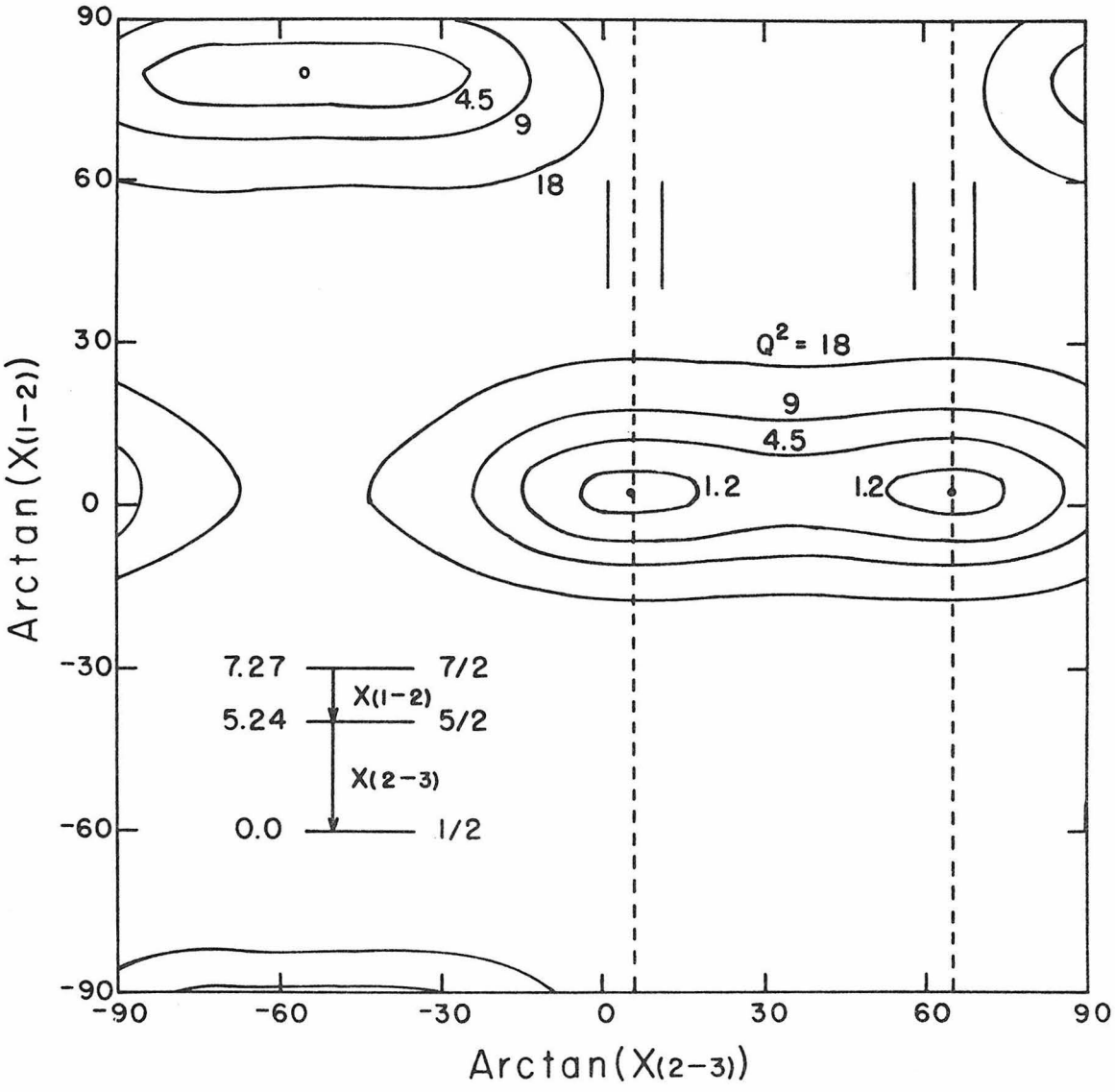
90
60
30
0
-30
-60
-90
-90
-60
-30
0
30
60
90
Arctan (X(1-2))
Arctan (X(2-3))
0
4.5
9
18
Q^2 = 18
9
4.5
1.2
1.2
7.27
7/2
X(1-2)
5.24
5/2
X(2-3)
0.0
1/2

FIGURE 23

Q^2 analyses of α-γ angular correlations for the γ-ray decay of the 2^{nd} excited state of ^{15}O. This γ-ray decay was part of the cascade γ-ray decay of both the 5^{th} and 6^{th} excited states of ^{15}O; the multipole mixings for the first γ-ray of the cascades are given in Table VIII. The significance of these analyses is discussed on page 28.

For additional details concerning the Q^2 analysis, see pages 23ff.

FIGURE 23

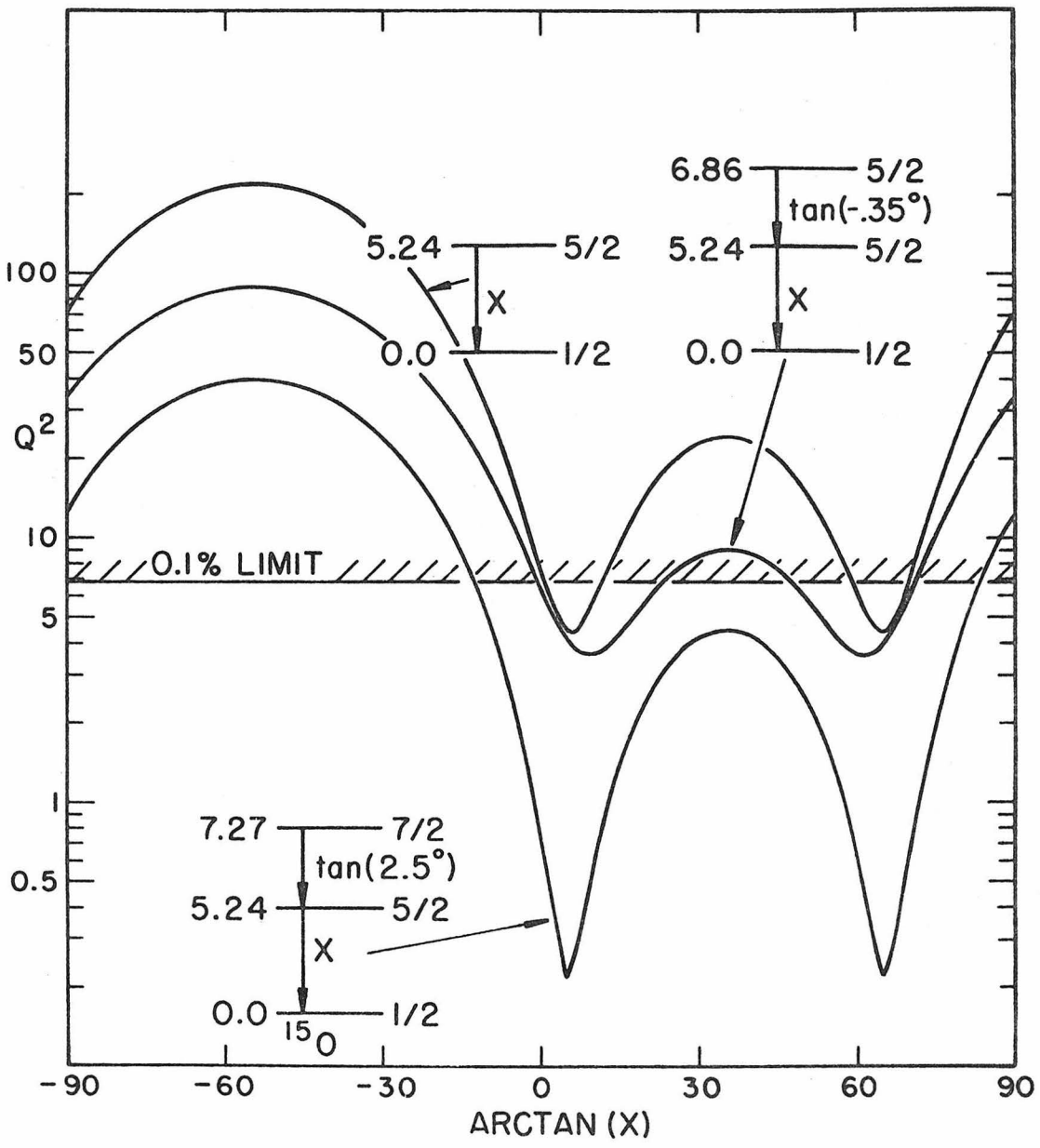
6.86
5/2
tan(-.35°)
5.24
5/2
X
0.0
1/2
5.24
5/2
X
0.0
1/2
100
50
Q^2
10
0.1% LIMIT
5
1
0.5
7.27
7/2
tan(2.5°)
5.24
5/2
X
0.0
1/2
^{15}O
-90
-60
-30
0
30
60
90
ARCTAN (X)

FIGURE 24

An energy-level diagram for ^{15}O based on the results of the present work for ^{15}O; these results are summarized in Table IX. All energies are in keV.

The changes in the information on the energy levels of ^{15}O resulting from the present work can best be seen by comparing this figure with Figure 4. Two spin and four parity assignments have been established, and the remaining assignments for the bound states have been confirmed. Because of the change in the value for the ground-state mass, three quantities which depend directly on this value have been changed: the Q-value for the $^{16}O(^{3}He, \alpha)^{15}O$ reaction; the value for the $^{14}N + p$ threshold; and the value for the excitation energy of the 7^{th} excited state (7.55 MeV). In addition, several of the values for the excitation energies have undergone significant changes, particularly that for the 6^{th} excited state; these last changes had little to do with the change in the value for the ground-state mass.

For additional details, see pages 29ff.

FIGURE 24

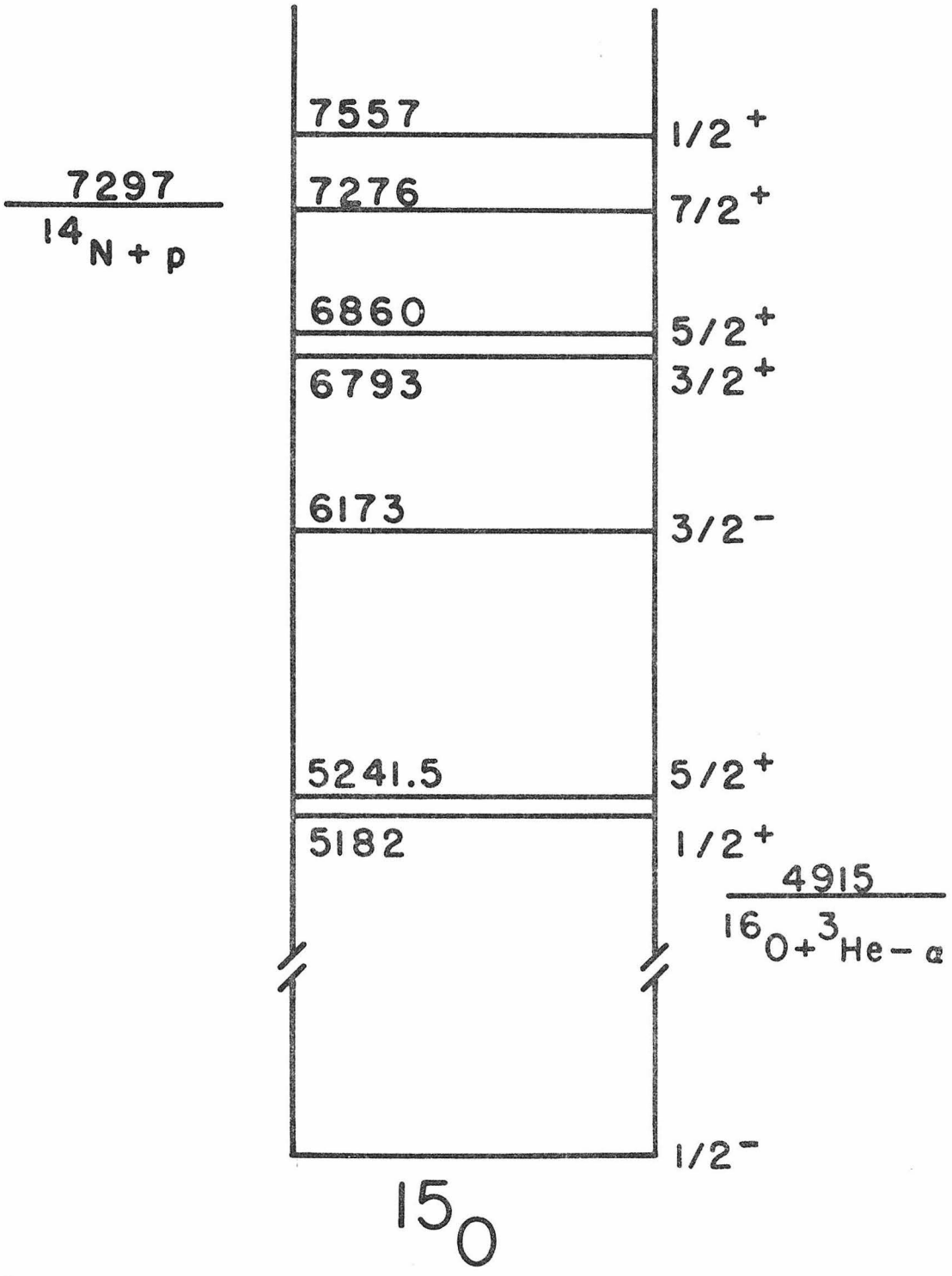
7557
1/2+
7297
14N + p
7276
7/2+
6860
5/2+
6793
3/2+
6173
3/2−
5241.5
5/2+
5182
1/2+
4915
16O+3He−α
1/2−
15O

FIGURE 25

The ratios of cross-sections from the $^{16}O(^{3}He, \alpha)$ reaction to the three, bound excited states of ^{15}O having $\ell_n = 2$ angular distributions. The smooth curves serve only to connect the data points. These ratios demonstrate a systematic difference between the two $\ell_n = 2$ angular distributions with J = 5/2 and the one with J = 3/2. In particular, the maximum near 39^{o} in the lower two curves is largely absent in the upper curve.

For further details, see pages 32 and 33.

FIGURE 25

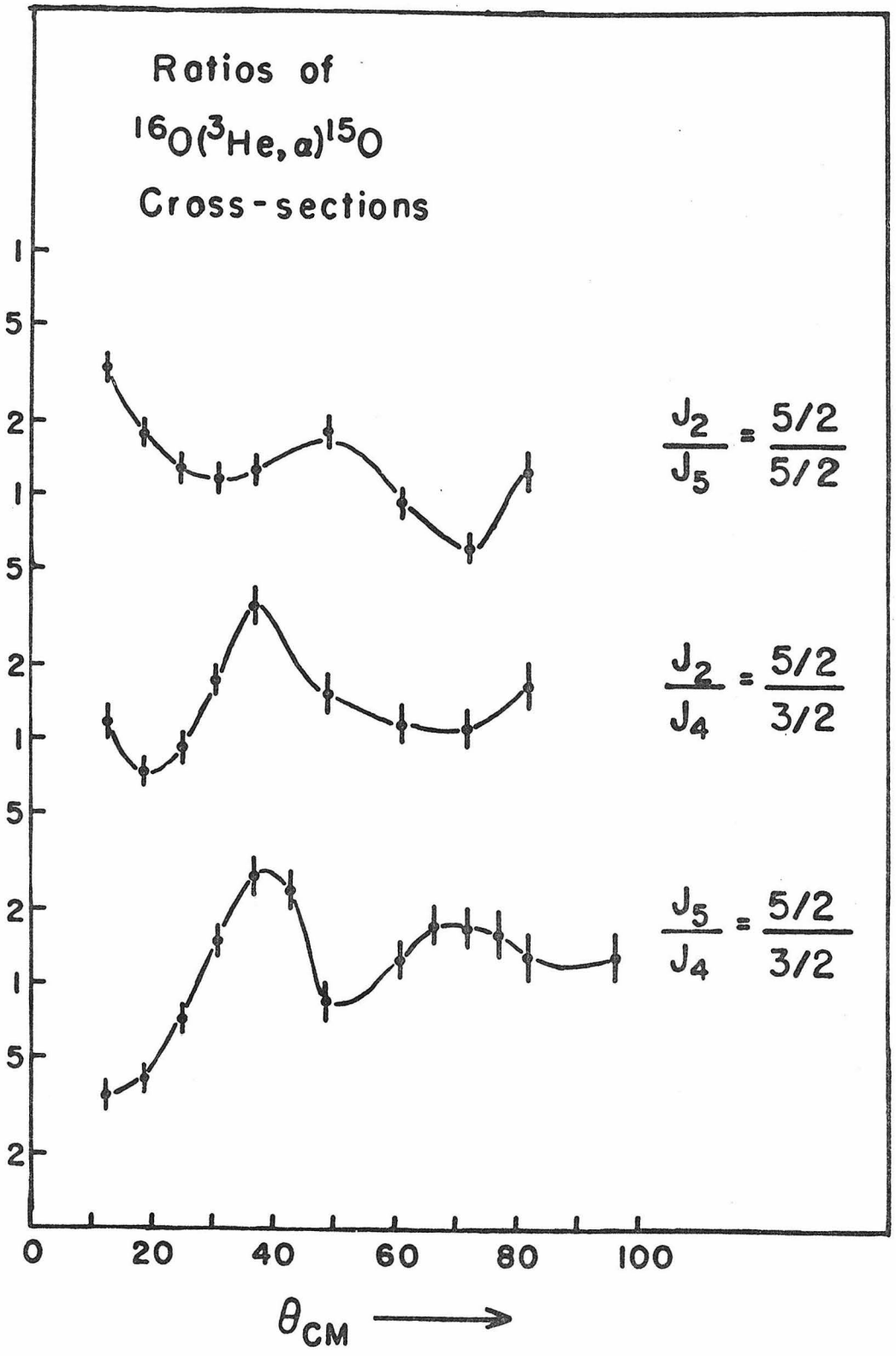
Ratios of
$^{16}O(^{3}He,\alpha)^{15}O$
Cross-sections
1
5
2
1
5
2
1
5
2
1
5
2
$\frac{J_2}{J_5} = \frac{5/2}{5/2}$
$\frac{J_2}{J_4} = \frac{5/2}{3/2}$
$\frac{J_5}{J_4} = \frac{5/2}{3/2}$
0
20
40
60
80
100
θ_{CM} ⟶

FIGURE 26

These proton spectra from the (^{3}He, p) reaction on two different targets gave the first clear evidence for the lowest T = 3/2 state in ^{13}C. A comparison of the two spectra indicates that the proton group near 18.6 MHz in the lower spectrum cannot have resulted from the usual ^{12}C and ^{16}O contamination in the boron target and must be due to the ^{11}B in the target. (See pages 40 and 41.)

FIGURE 26

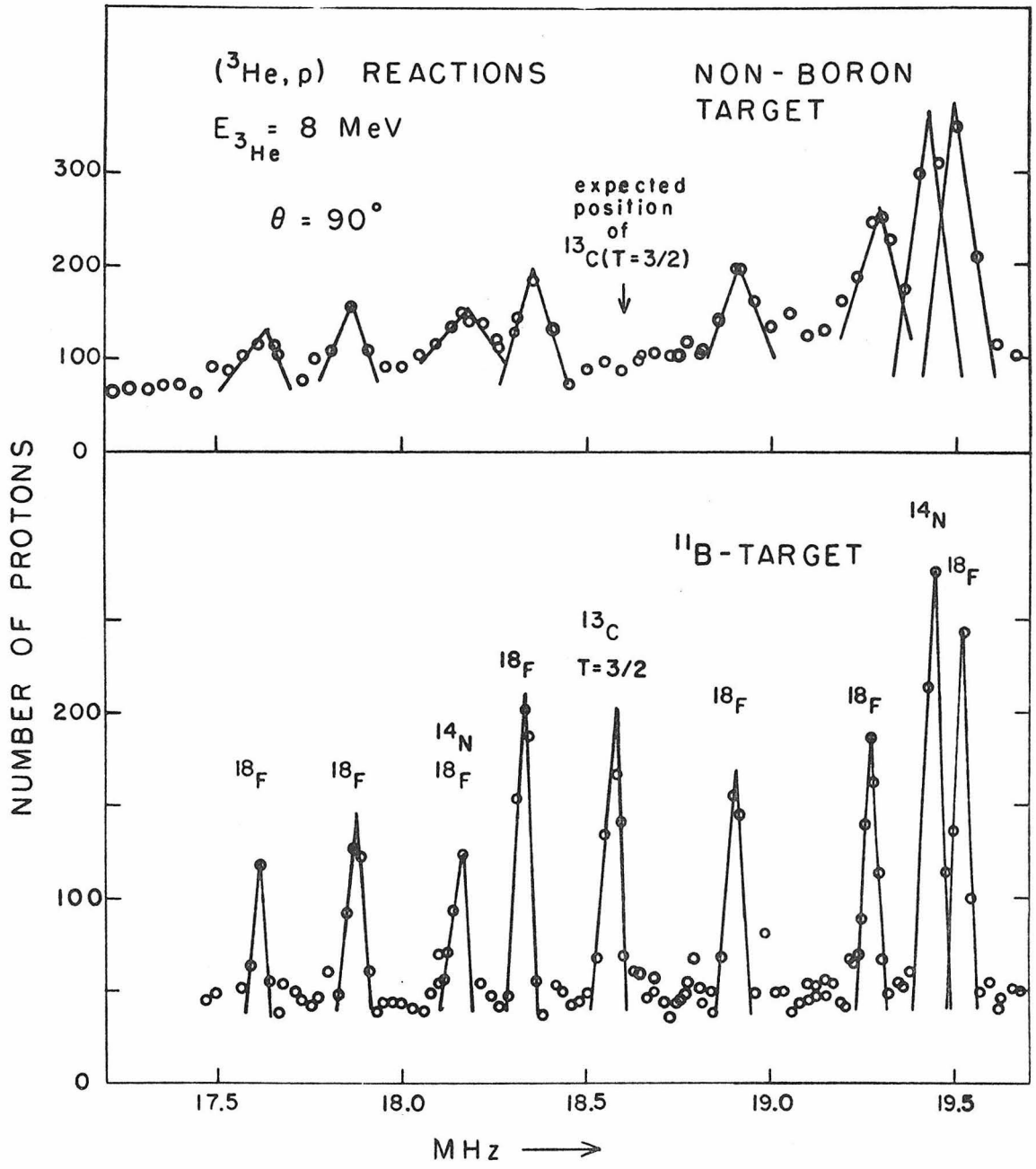
(3He, p) REACTIONS
E3He = 8 MeV
θ = 90°
NON-BORON TARGET
expected position of 13C(T=3/2)
11B-TARGET
18F
14N
13C T=3/2
NUMBER OF PROTONS
MHz
17.5
18.0
18.5
19.0
19.5
0
100
200
300

FIGURE 27

An isobar diagram for T = 3/2 states with A = 13; all energies are in MeV. The information on ^{13}B comes from Middleton and Pullen (1964); the information on ^{13}N comes from Adelberger (1967). For further details concerning this figure, see pages 50 and 51.

FIGURE 27

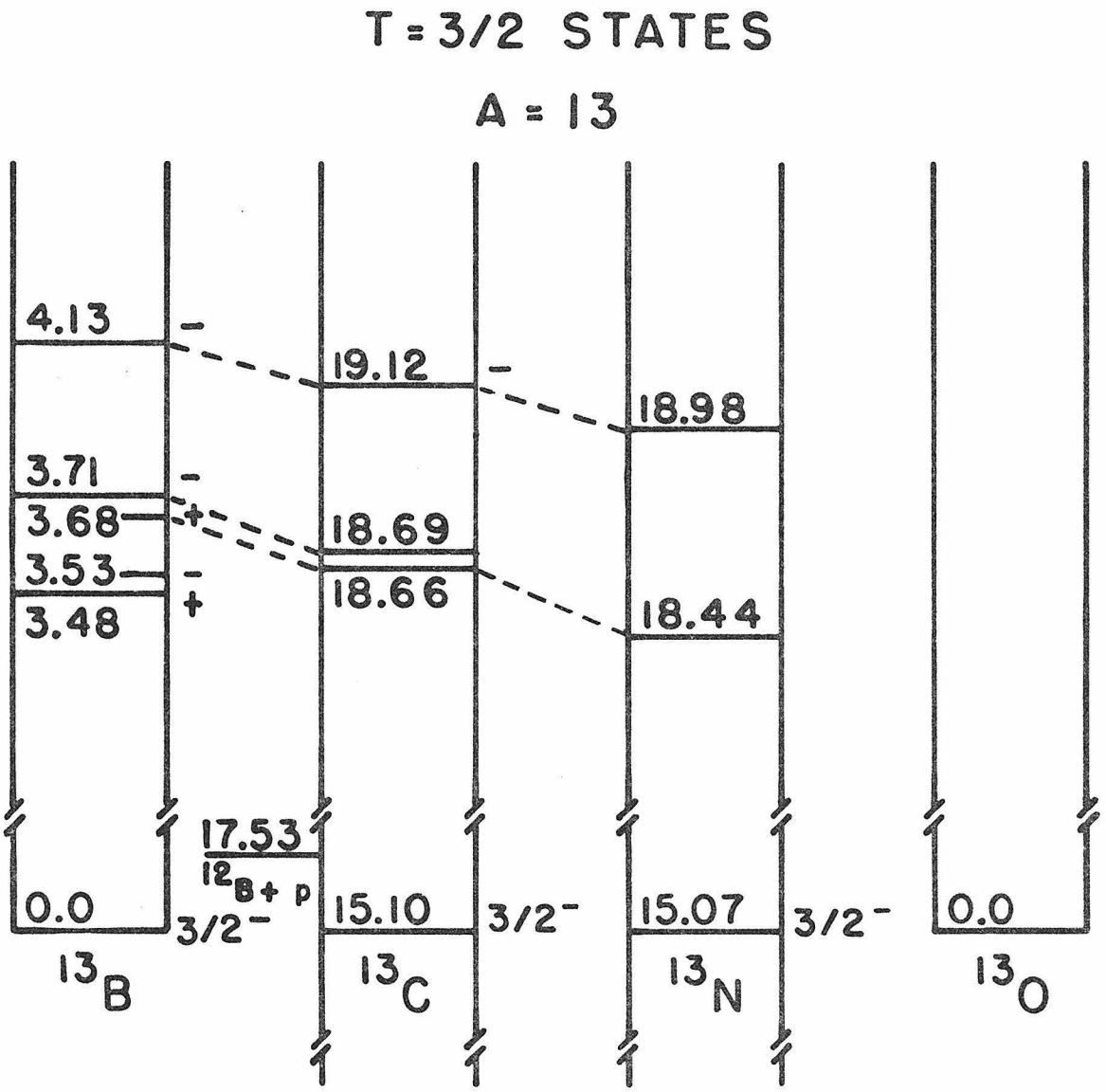
T = 3/2 STATES
A = 13
4.13
3.71
3.68
3.53
3.48
19.12
18.69
18.66
18.98
18.44
17.53
12B + p
0.0
3/2−
15.10
3/2−
15.07
3/2−
0.0
13B
13C
13N
13O

FIGURE 28

These proton spectra resulted from the (^{3}He, p) reaction on the targets indicated to the right of each of the spectra; note the suppressed zero in two of the spectra. A comparison of the lowest spectrum with the two upper spectra indicates the presence of at least three groups arising from the ^{11}B(^{3}He, p) reaction; these groups were assumed to correspond to T = 3/2 states in ^{13}C. The approximate positions of groups for two other T = 3/2 states in ^{13}C expected to be excited by the ^{11}B(^{3}He, p) reaction are indicated in the lowest spectrum. (See page 40.)

FIGURE 28

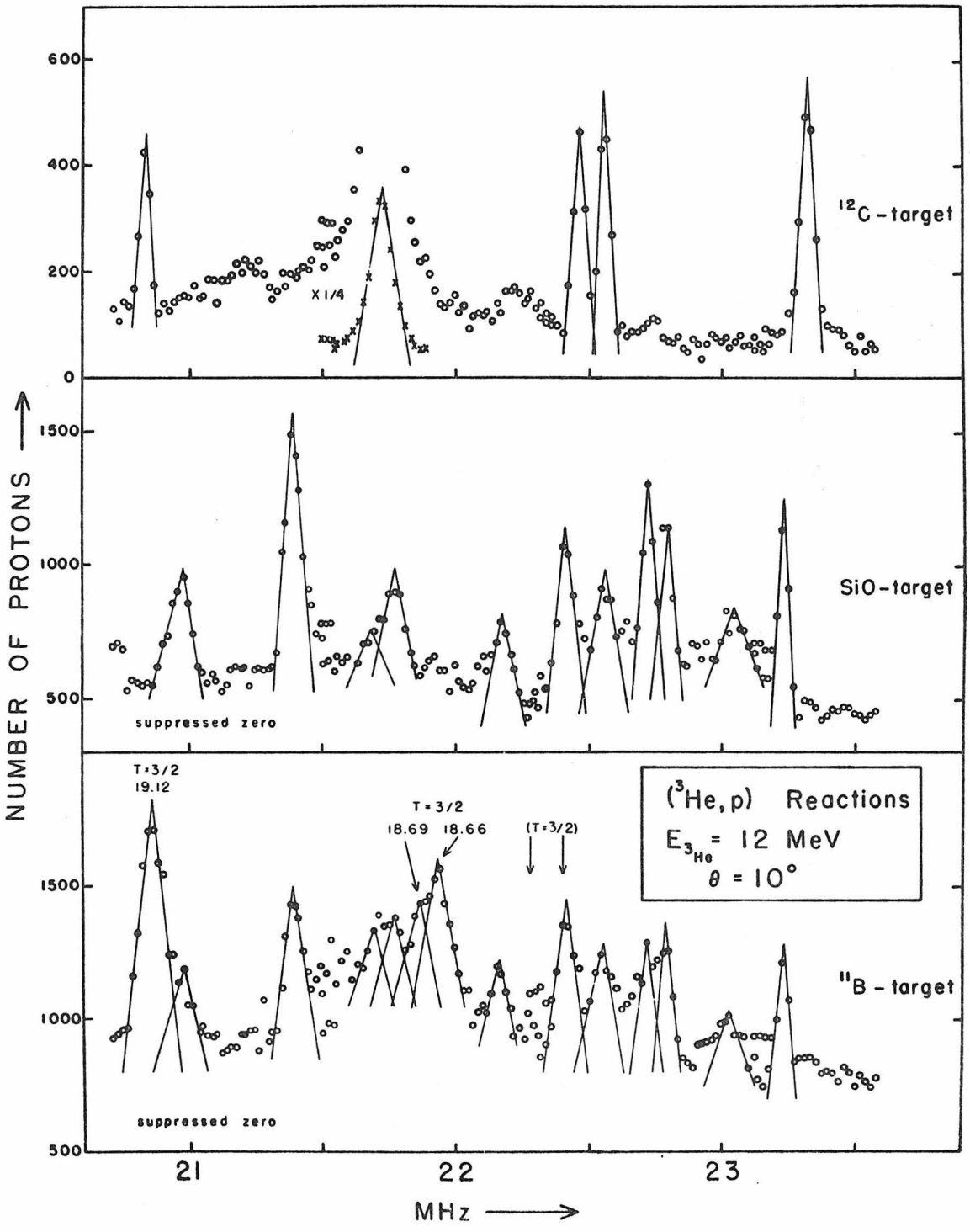
NUMBER OF PROTONS
600
400
200
0
X 1/4
^{12}C - target
1500
1000
500
SiO - target
suppressed zero
T=3/2
19.12
T = 3/2
18.69 18.66
(T=3/2)
(^{3}He, p) Reactions
$E_{^{3}He}$ = 12 MeV
θ = 10°
^{11}B - target
suppressed zero
1500
1000
500
21
22
23
MHz

FIGURE 29

This proton spectrum from the $^{11}B(^{3}He, p)$ reaction shows the T = 3/2 doublet at 18.67 MeV in more detail. Even though this spectrum was taken with a boron target with a very small oxygen contamination, it was not possible to identify the proton group at 22.4 MHz as corresponding to one of the two T = 3/2 states in ^{13}C expected there because of the presence of a group for a state in ^{18}F. (See page 42.)

FIGURE 29

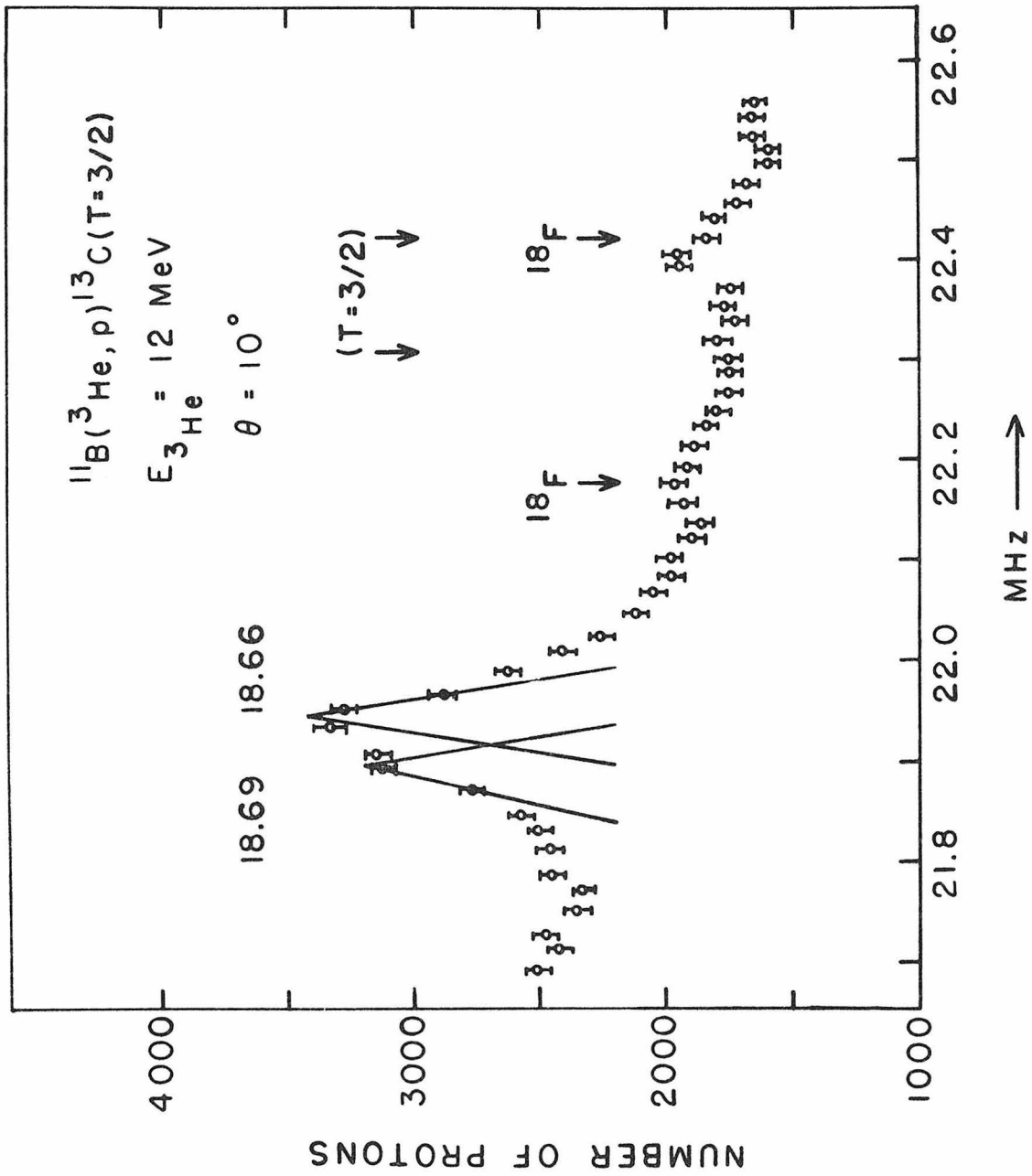
$^{11}B(^3He,p)^{13}C(T=3/2)$
$E_{^3He}$ = 12 MeV
θ = 10°
(T=3/2)
^{18}F
^{18}F
18.69
18.66
NUMBER OF PROTONS
4000
3000
2000
1000
21.8
22.0
22.2
22.4
22.6
MHz

FIGURE 30

The α-particle spectra are from the (^{3}He, α) reaction on gold-backed carbon targets, ^{12}C in the upper spectrum and ^{14}C in the lower spectrum. There was also a small ^{16}O contamination in both of the targets. A comparison of the two spectra indicates that the group at 32 MHz in the lower spectrum must arise from the ^{14}C(^{3}He, α) reaction; the group corresponds to the T = 3/2 state in ^{13}C at 15.1 MeV. (See page 43.)

FIGURE 30

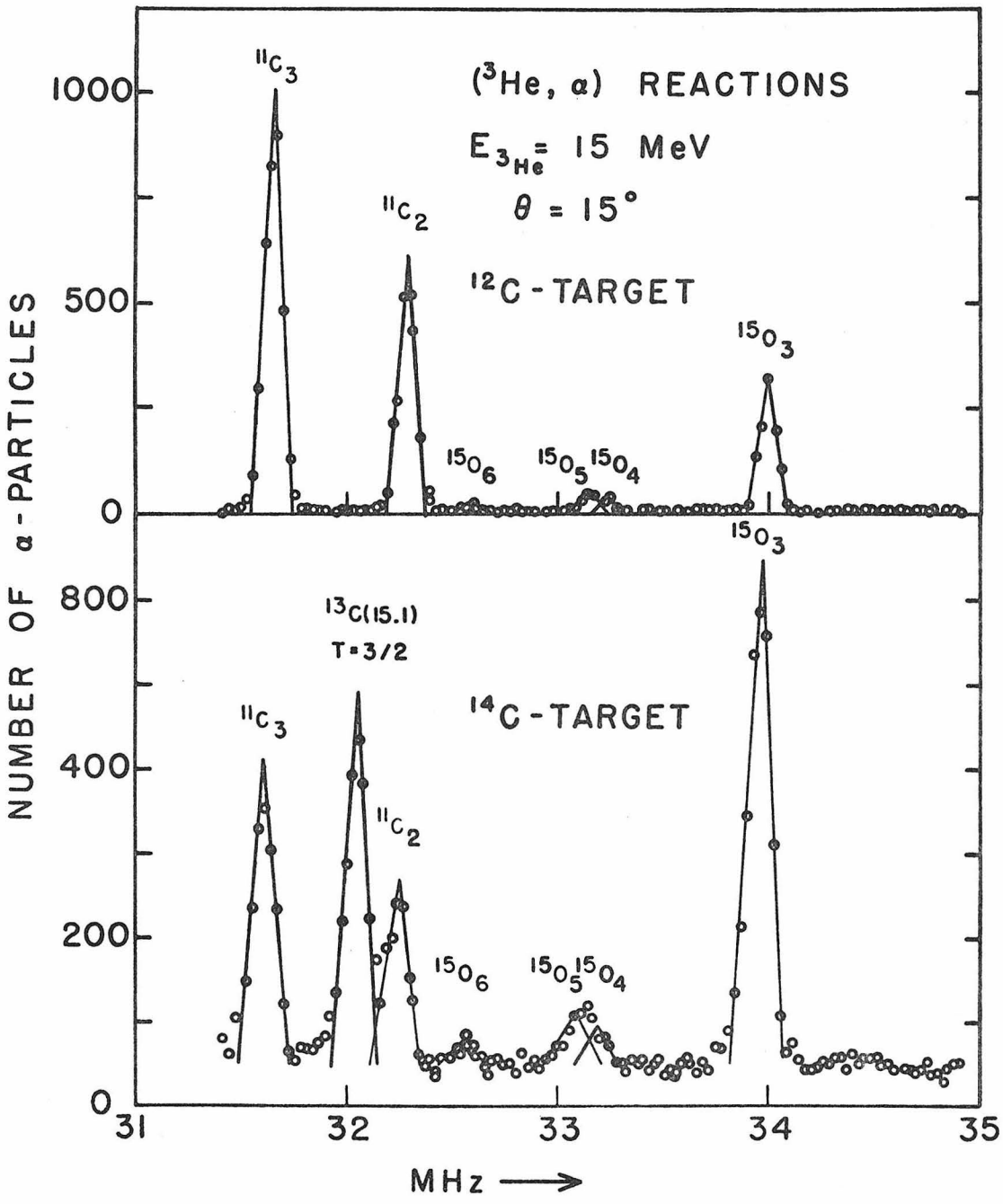
(3He, α) REACTIONS
E3He = 15 MeV
θ = 15°
12C-TARGET
14C-TARGET
11C3
11C2
15O6
15O5 15O4
15O3
13C(15.1)
T=3/2
NUMBER OF α-PARTICLES
MHz
0
200
400
500
800
1000
31
32
33
34
35

FIGURE 31

An angular distribution from the $^{11}B(^{3}He, p)$ reaction for the lowest T = 3/2 state in ^{13}C. In addition to the probable errors indicated in the figure, there is an uncertainty of about 10% in the absolute normalization. See pages 47 and 48 for additional details.

FIGURE 31

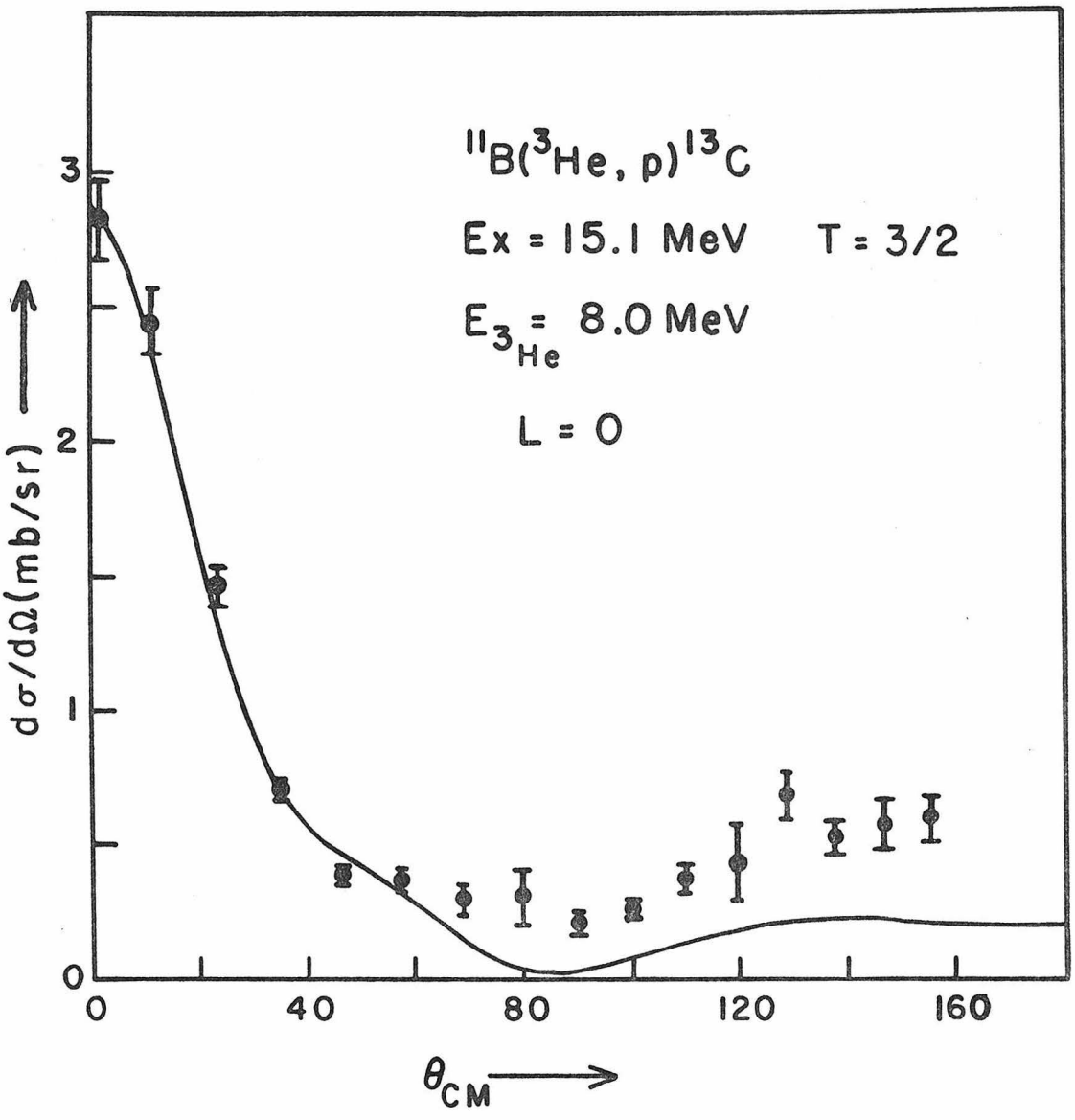
$^{11}B(^3He, p)^{13}C$
Ex = 15.1 MeV T = 3/2
$E_{^3He}$ = 8.0 MeV
L = 0
dσ/dΩ(mb/sr)
θ_{CM}
0
1
2
3
0
40
80
120
160

FIGURE 32

Angular distributions from the $^{11}B(^{3}He, p)$ reaction for the T = 3/2 states in ^{13}C at 15.1 and 19.12 MeV. In addition to the probable errors indicated in the figure, there is an uncertainty of about 20% in the absolute normalization. See pages 47 and 48 for additional details.

FIGURE 32

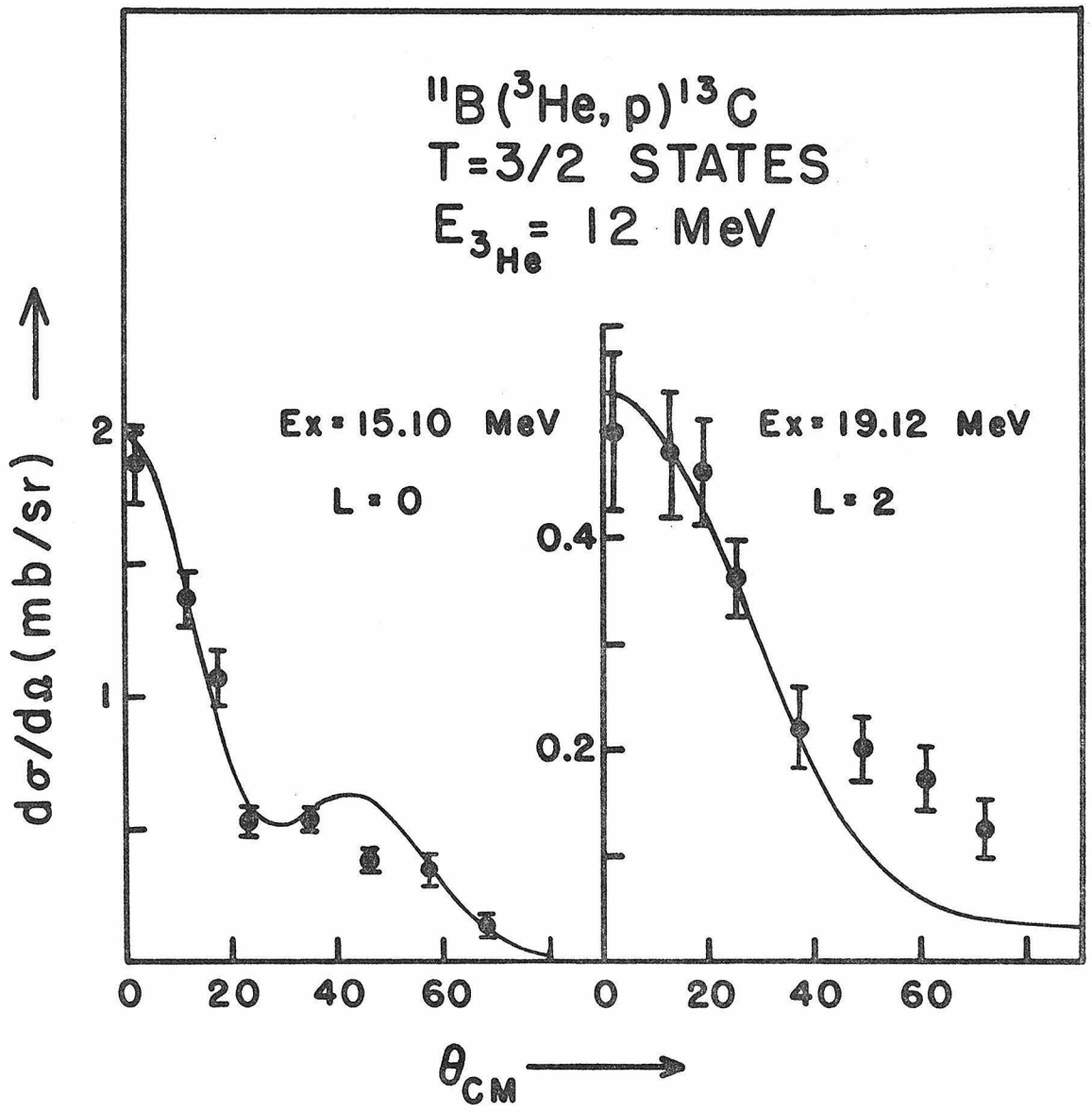
$^{11}B(^3He, p)^{13}C$
T=3/2 STATES
$E_{^3He}$ = 12 MeV
Ex = 15.10 MeV
L = 0
Ex = 19.12 MeV
L = 2
dσ/dΩ (mb/sr)
2
1
0.4
0.2
0
20
40
60
θ_{CM}

FIGURE 33

A proton spectrum from the $^{11}B(^{3}He, p)$ reaction with the protons detected at 0^{o}. The FWHM of the proton group corresponding to the lowest T = 3/2 state in ^{13}C is close to the expected resolution, and this indicates that the width of the T = 3/2 state is probably much less than 18 keV. (See page 48.)

FIGURE 33

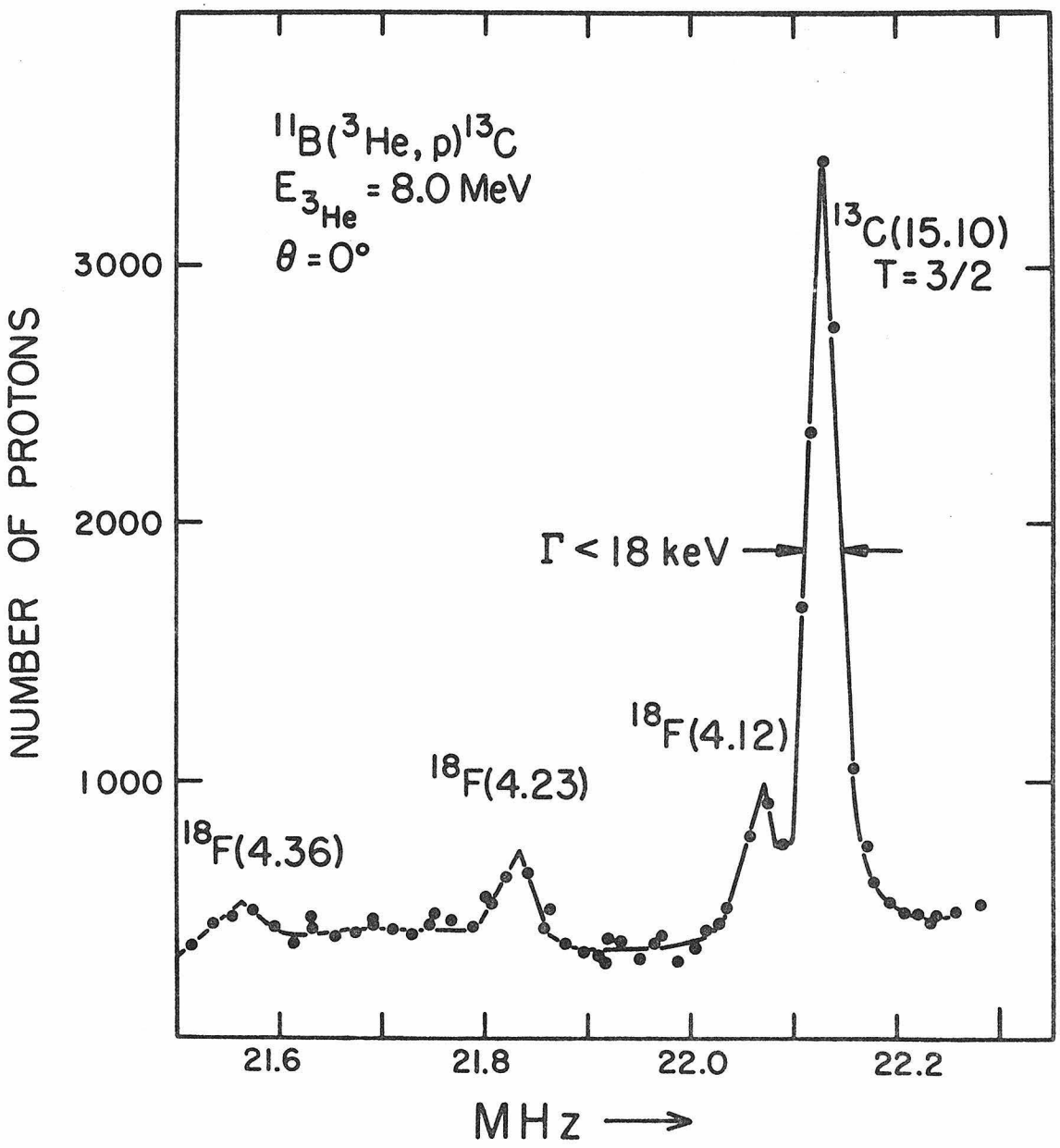
$^{11}B(^3He, p)^{13}C$
$E_{^3He}$ = 8.0 MeV
θ = 0°
$^{13}C(15.10)$
T = 3/2
Γ < 18 keV
$^{18}F(4.12)$
$^{18}F(4.23)$
$^{18}F(4.36)$
NUMBER OF PROTONS
3000
2000
1000
21.6
21.8
22.0
22.2
MHz ⟶

FIGURE 34

A high-resolution proton spectrum from the $^{11}B(^{3}He, p)$ reaction to the lowest $T = 3/2$ state in ^{13}C, on a thin, tantalum-backed boron target. The experimental resolution was assumed equal to the FWHM of the triangle shown in the figure. An attempt to explain this resolution by folding together the three contributions depicted schematically above the proton group is represented by the dashed line. For additional details and a discussion of the significance of this spectrum, see pages 43 through 45.

FIGURE 34

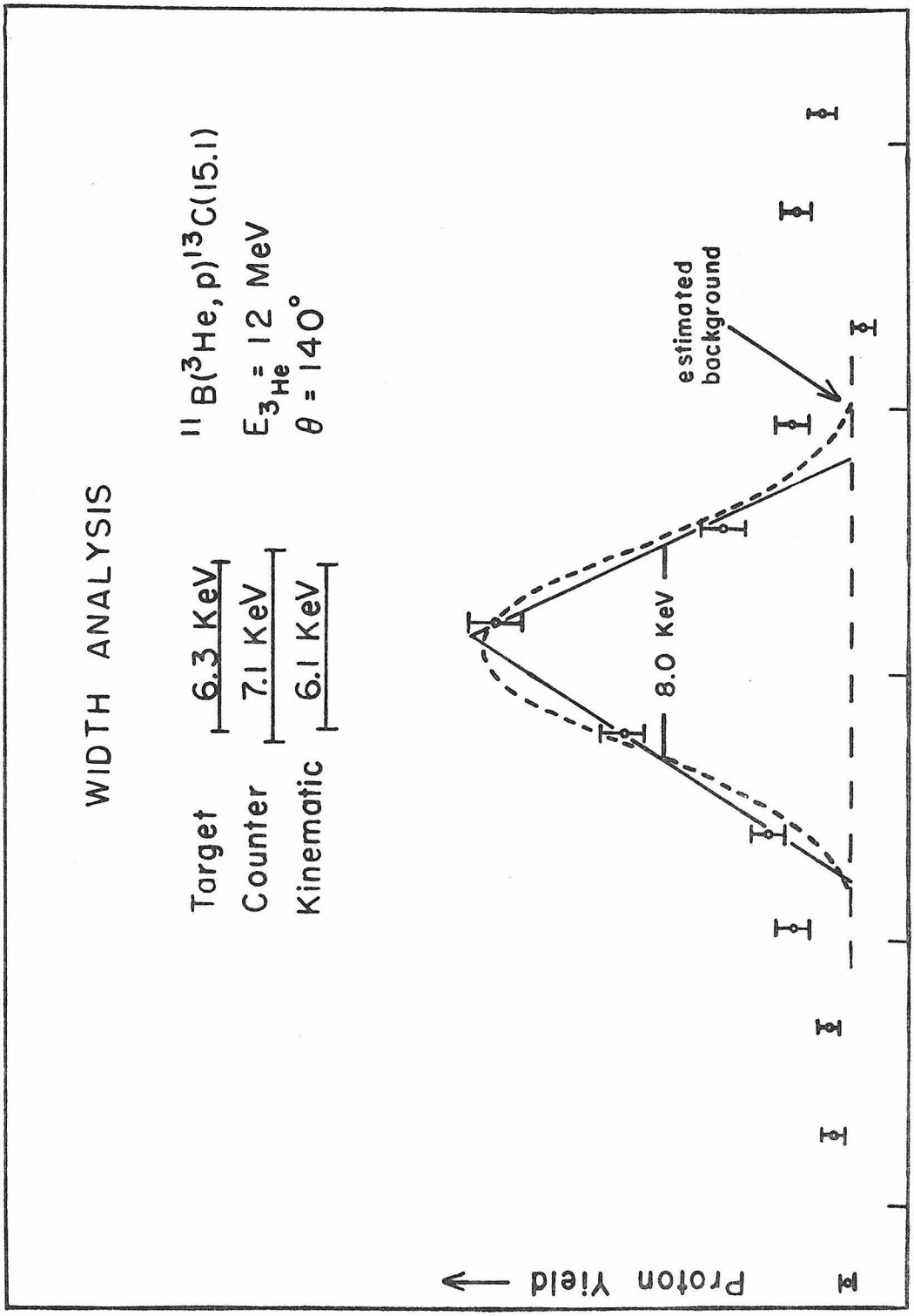
WIDTH ANALYSIS
$^{11}B(^3He, p)^{13}C(15.1)$
$E_{^3He} = 12$ MeV
$\theta = 140°$
Target 6.3 KeV
Counter 7.1 KeV
Kinematic 6.1 KeV
8.0 KeV
estimated background
Proton Yield
Proton Energy(KeV)
2970
2980
2990
3000
3010

FIGURE 35

Two α-particle spectra from the (^{3}He, α) reaction on a Ni ^{18}O target, which had a small ^{12}C and ^{16}O contamination. Groups arising from the reaction on the contaminants are identified according to the final nucleus; groups for T = 3/2 states in ^{17}O are identified by their corresponding excitation energies in MeV. Seven T = 3/2 states in ^{17}O were identified in these spectra. (See page 52.)

FIGURE 35

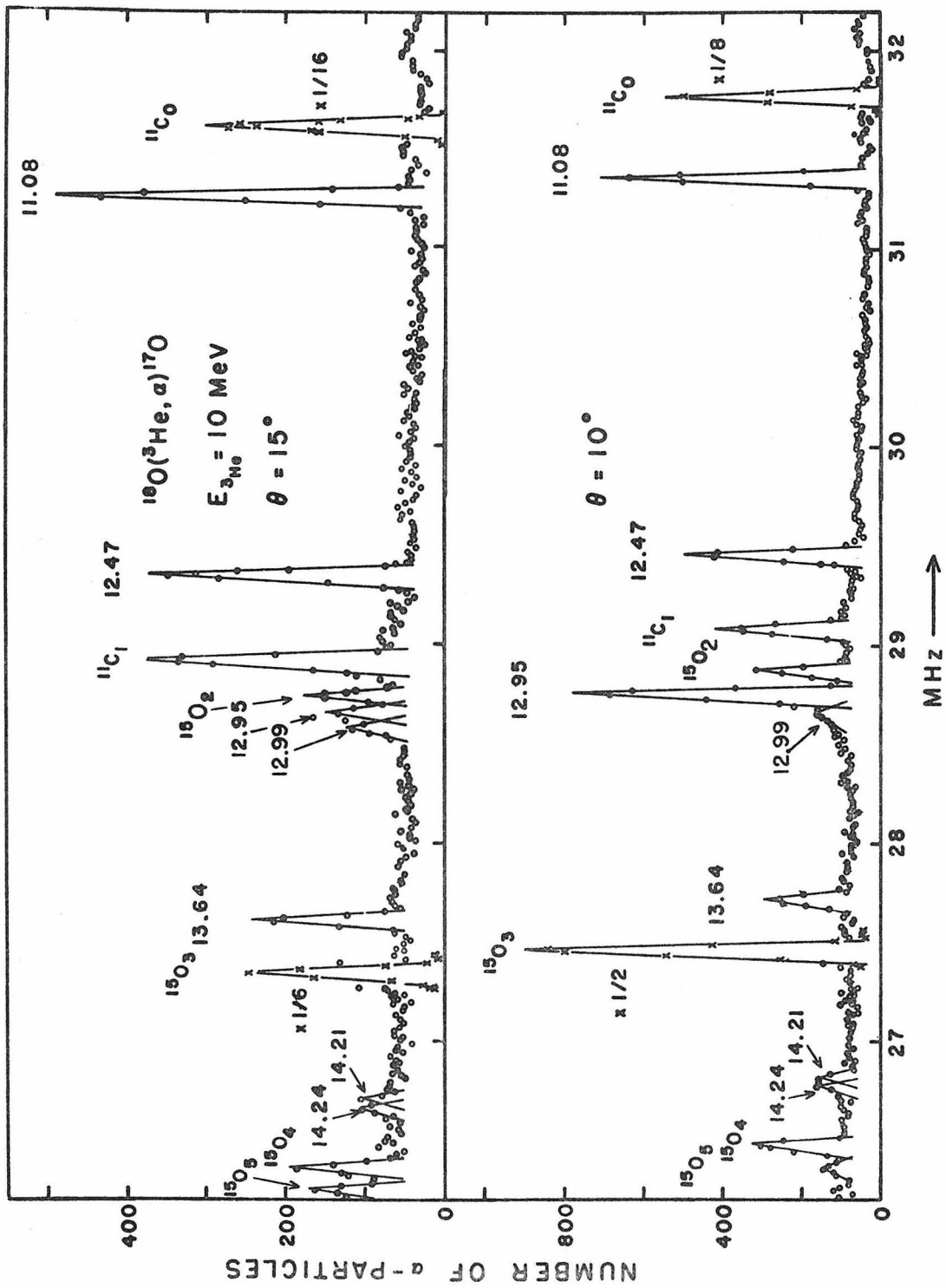
NUMBER OF α-PARTICLES
MHz
$^{16}O(^3He,\alpha)^{17}O$
$E_{^3He}$ = 10 MeV
θ = 15°
θ = 10°
11.08
12.47
12.95
12.99
13.64
14.21
14.24
$^{11}C_0$
$^{11}C_1$
$^{15}O_2$
$^{15}O_3$
$^{15}O_4$
$^{15}O_5$
x1/16
x1/6
x1/2
x1/8

FIGURE 36

An isobar diagram for T = 3/2 states with A = 17; all energies are in MeV. The information on ^{17}N comes from Ajzenberg-Selove and Lauritsen (1959); the information on ^{17}F comes from Adelberger (1967). For further details, see pages 61 through 63.

FIGURE 36

T = 3/2 STATES

A = 17

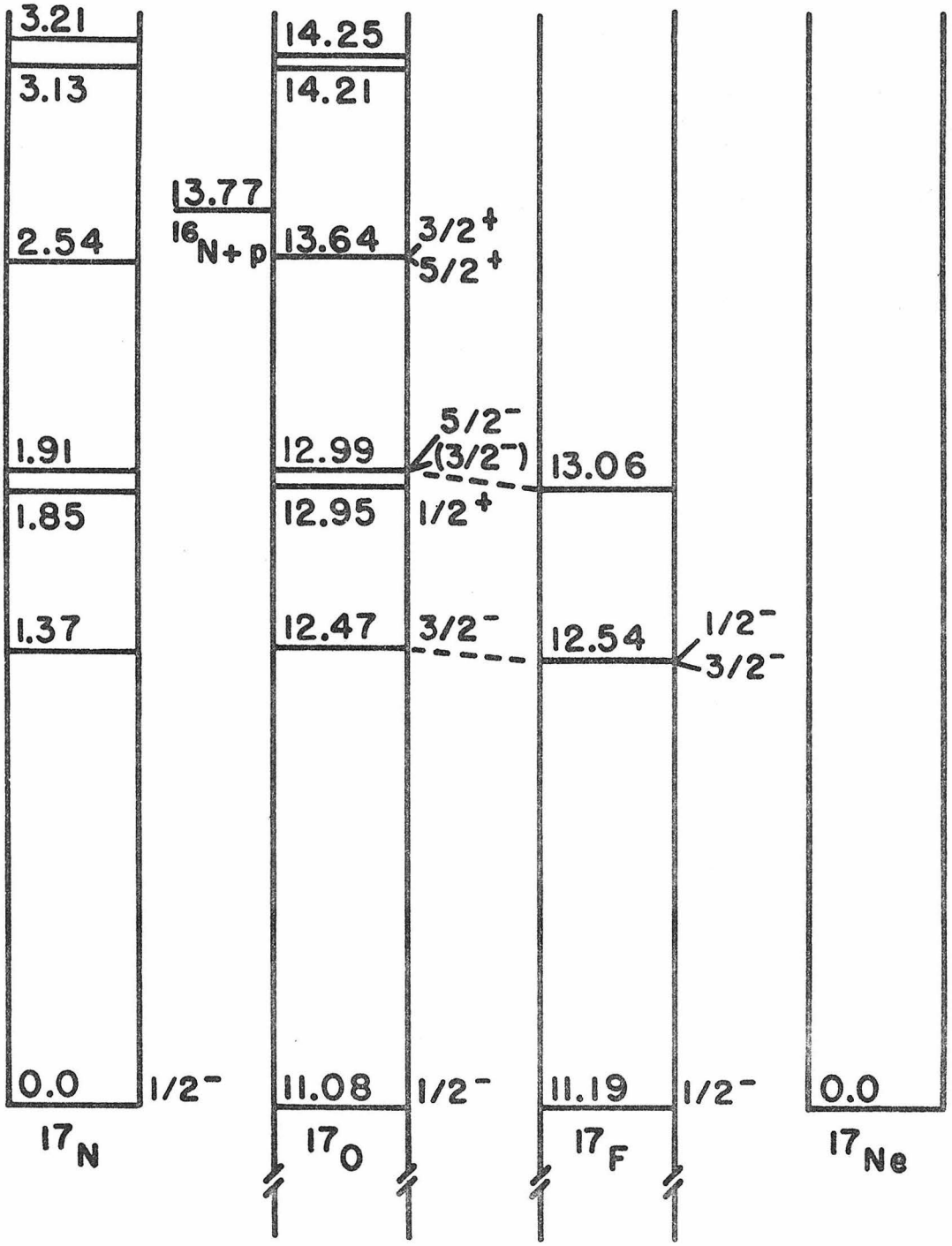

FIGURE 37

Proton spectra from the $^{15}N(^{3}He, p)$ reaction on ^{15}N in the gas target, taken at angles of 10^{o} and 30^{o}. Groups corresponding to some of the T = 3/2 states noted in Figure 35 are indicated by the respective excitation energies in MeV. The "recoil proton" group arises from the $p(^{3}He, p)^{3}He$ reaction on a hydrogen contamination in the ^{15}N gas. The remaining groups were assumed to correspond to T = 1/2 states in ^{17}N. For further details, see pages 52 and 53.

FIGURE 37

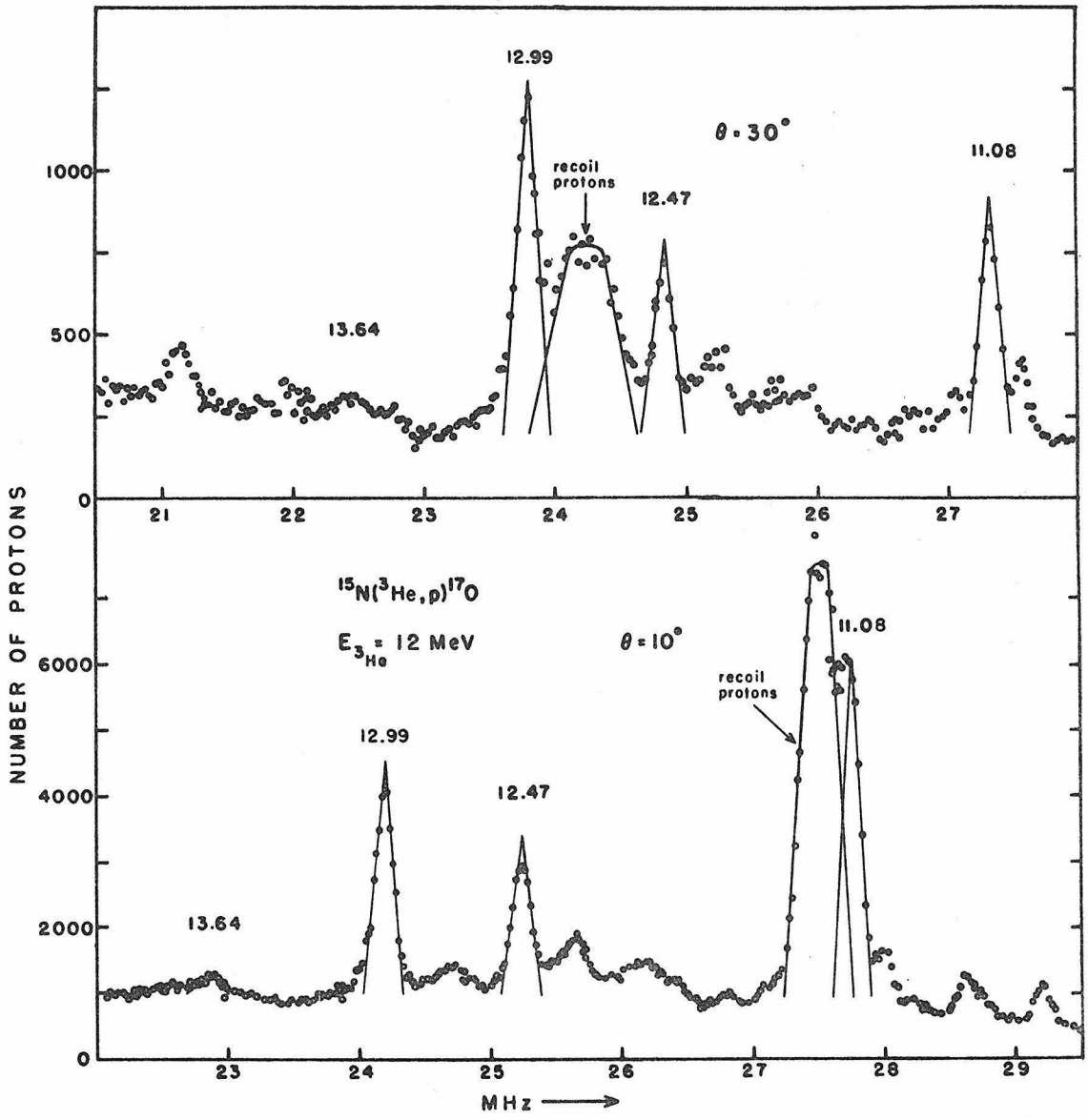
12.99
θ = 30°
11.08
recoil protons
12.47
13.64
1000
500
0
21
22
23
24
25
26
27
NUMBER OF PROTONS
15N(3He,p)17O
E3He = 12 MeV
θ = 10°
11.08
recoil protons
6000
12.99
12.47
4000
13.64
2000
0
23
24
25
26
27
28
29
MHz

FIGURE 38

Angular distributions from the $^{15}N(^{3}He, p)$ reaction for three T = 3/2 states in ^{17}O. The effective incident energy was 11.86 MeV after correcting the 12-MeV incident energy for energy losses in the entrance foil and the target gas. In addition to the probable errors indicated in the figure, there is an uncertainty of approximately 20% in the absolute normalization. For further details, see pages 56 and 57.

FIGURE 38

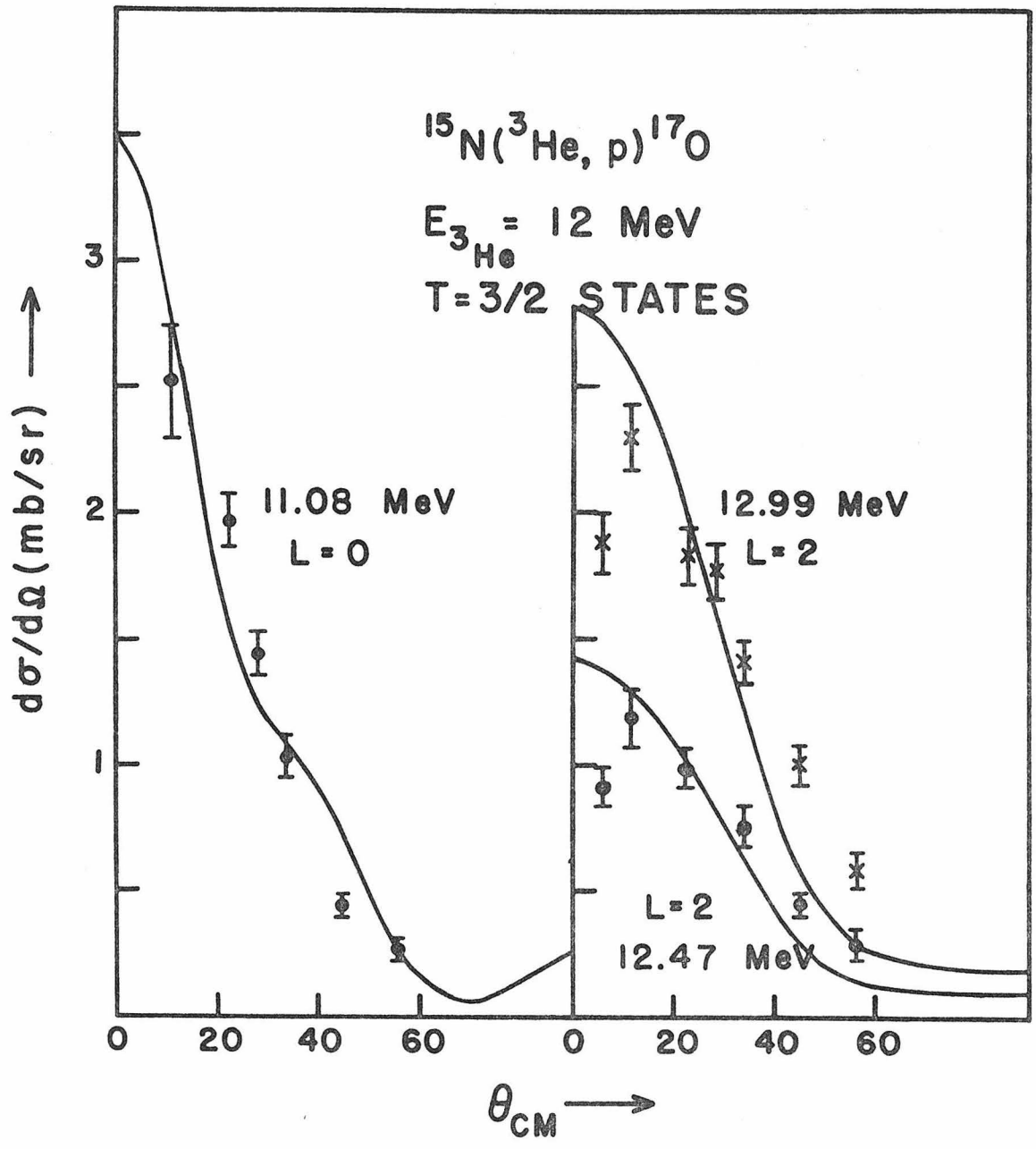
$^{15}N(^{3}He, p)^{17}O$
$E_{^{3}He}$ = 12 MeV
T=3/2 STATES
11.08 MeV
L=0
12.99 MeV
L=2
L=2
12.47 MeV
dσ/dΩ (mb/sr)
θ_{CM}
0
20
40
60
1
2
3

FIGURE 39

Angular distributions from the $^{18}O(^{3}He, \alpha)$ reaction for four T = 3/2 states in ^{17}O; the distributions were measured at incident energies of 10 and 12 MeV. In addition to the probable errors indicated in the figure, there is an uncertainty of approximately 20% in the absolute normalization. For further details, see pages 57 and 58.

FIGURE 39

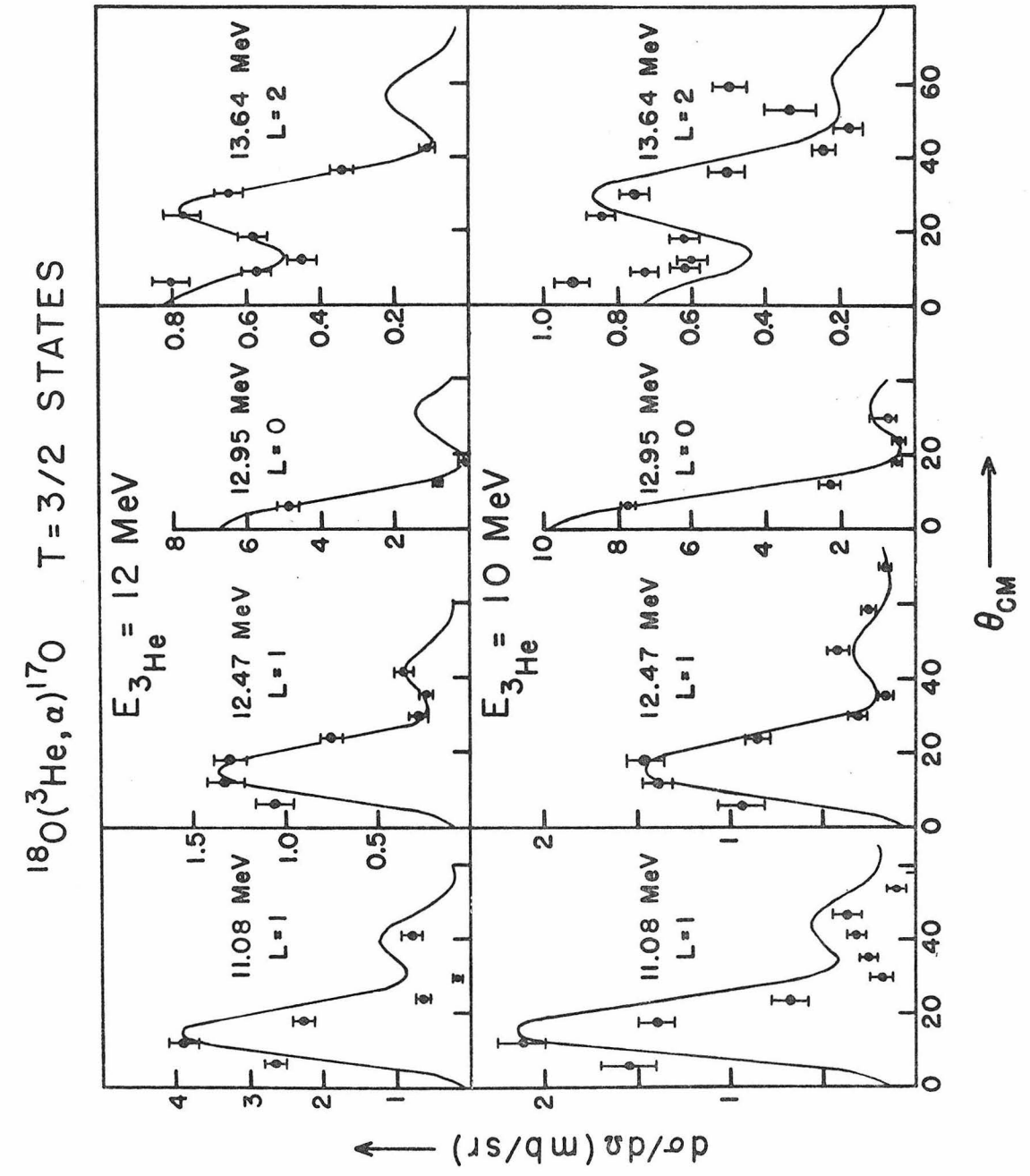
$^{18}O(^3He,\alpha)^{17}O$ T=3/2 STATES
$E_{^3He}$ = 12 MeV
$E_{^3He}$ = 10 MeV
11.08 MeV L=1
12.47 MeV L=1
12.95 MeV L=0
13.64 MeV L=2
dσ/dΩ (mb/sr)
θ_{CM}

FIGURE 40

An angular distribution from the $^{18}O(^{3}He, \alpha)$ reaction for the T = 3/2 state in ^{17}O at an excitation energy of 12.99 MeV. Data from five separate experiments are included in this figure; three data sets were taken with the 16-counter array, and two data sets with a position-sensitive counter (PSC). The smooth line in the figure is the prediction of the DWBA theory for an $\ell_n = 3$ angular distribution, and the arrows at the top of the figure indicate the angles at which the first maxima for $\ell_n = 1$ and $\ell_n = 2$ angular distributions are predicted to lie. For further details and a discussion of the significance of this figure, see pages 58 through 60.

FIGURE 40

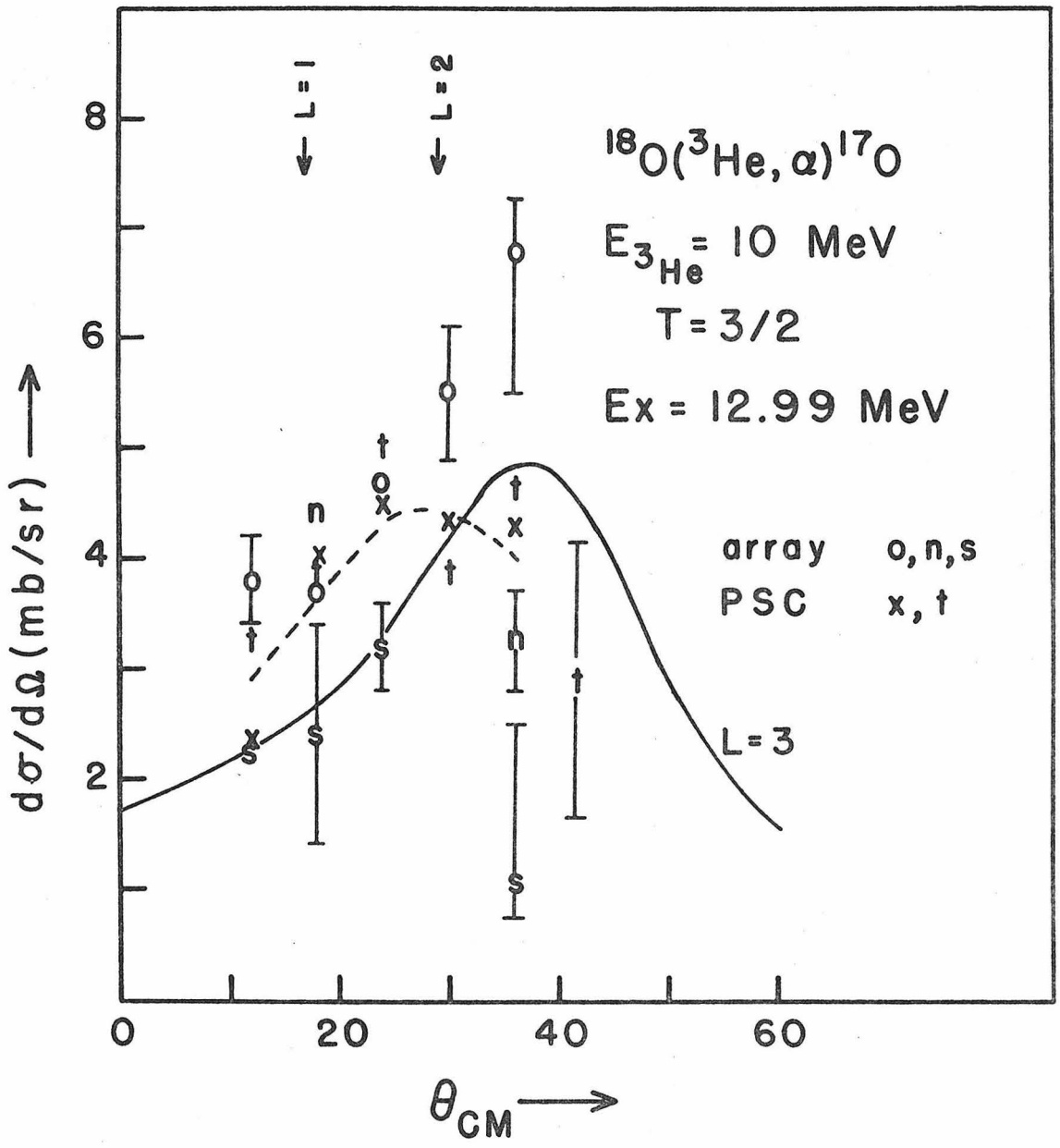
L=1
L=2
$^{18}O(^3He,\alpha)^{17}O$
$E_{^3He}$= 10 MeV
T=3/2
Ex = 12.99 MeV
array o,n,s
PSC x,t
L=3
$d\sigma/d\Omega$ (mb/sr)
θ_{CM}
0
20
40
60
2
4
6
8

FIGURE 41

Two α-particle spectra from the $^{18}O(^{3}He, \alpha)$ reaction to T = 3/2 states in ^{17}O near 13-MeV excitation energy. The purpose of these spectra is to demonstrate some of the difficulties of resolving the 12.99-MeV state at angles greater than 30^{o}.
See pages 58 and 59.

FIGURE 41

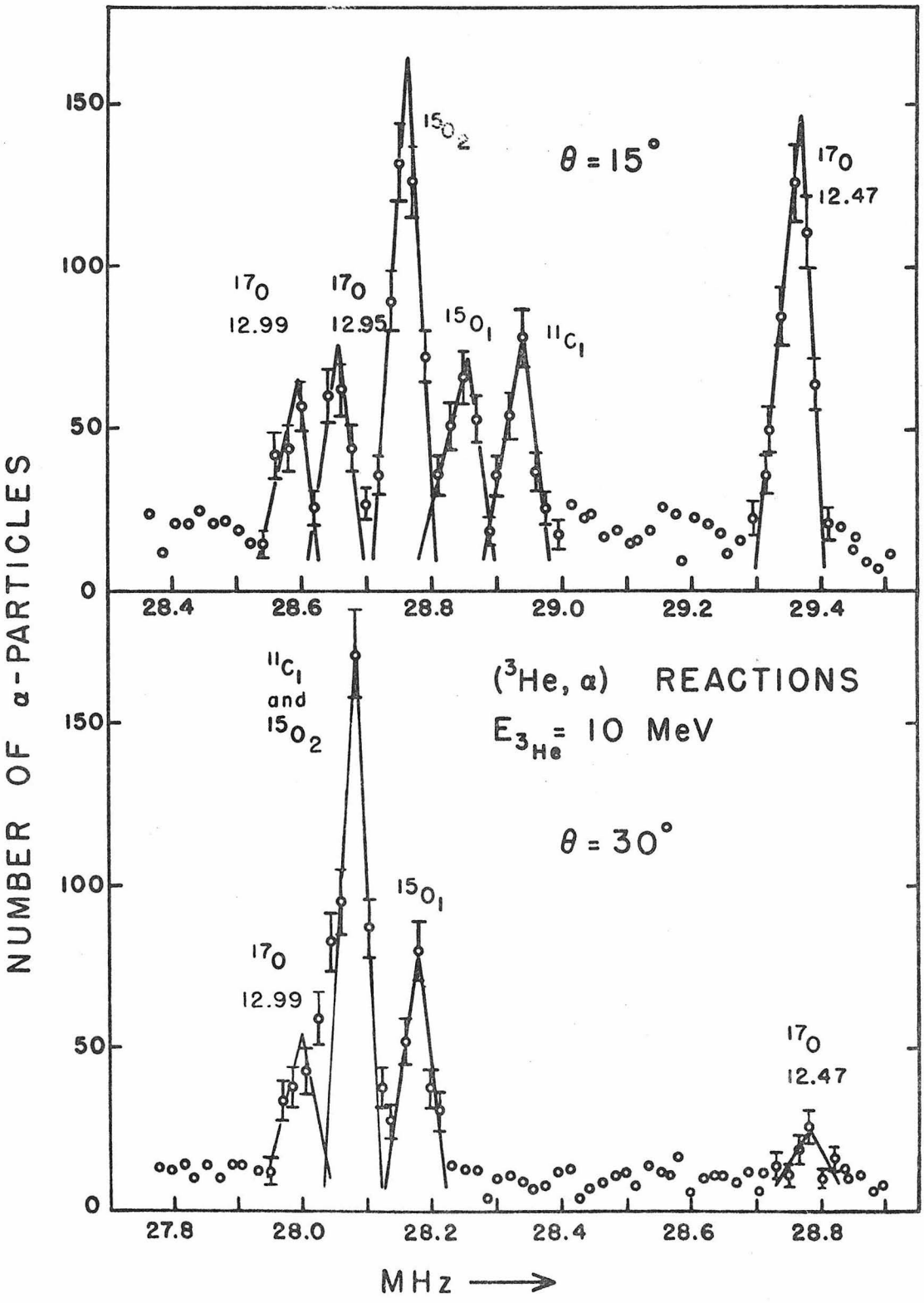
NUMBER OF α-PARTICLES
150
100
50
0
$^{15}O_2$
θ = 15°
^{17}O 12.47
^{17}O 12.99
^{17}O 12.95
$^{15}O_1$
$^{11}C_1$
28.4
28.6
28.8
29.0
29.2
29.4
$^{11}C_1$ and $^{15}O_2$
(^{3}He, α) REACTIONS
$E_{^3He}$ = 10 MeV
θ = 30°
$^{15}O_1$
^{17}O 12.99
^{17}O 12.47
27.8
28.0
28.2
28.4
28.6
28.8
MHz ⟶

FIGURE 42

Two proton spectra from the $^{19}F(^{3}He, p)$ reaction to the region of excitation energy where the two lowest T = 3/2 states in ^{21}Ne were expected. Note that the doublet at 33.3 MHz in the lower spectrum has been divided by a factor of 6. The groups are identified according to their excitation energies (keV) in ^{21}Ne. See pages 63 and 64.

FIGURE 42

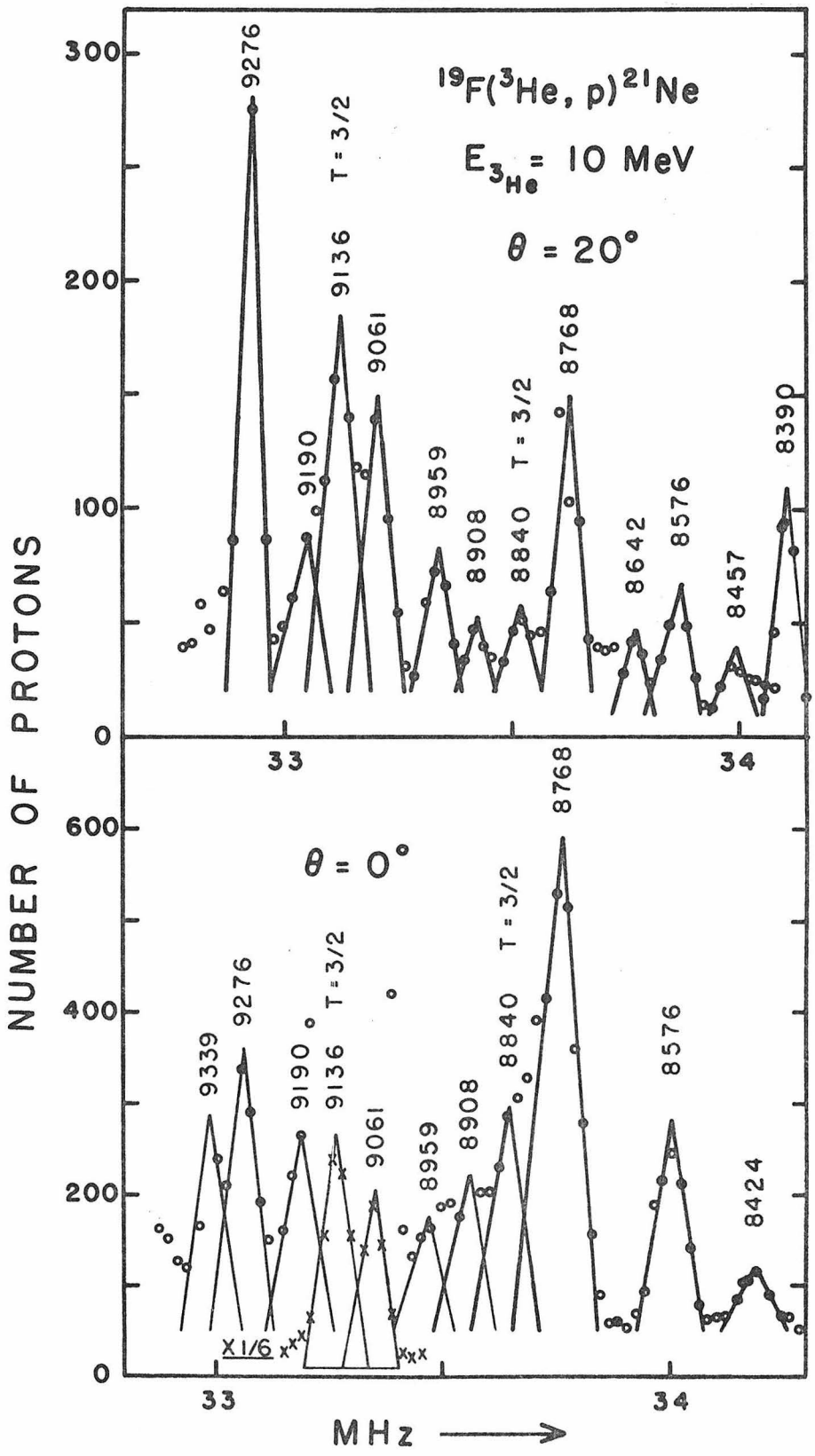
$^{19}F(^3He, p)^{21}Ne$
$E_{^3He}$ = 10 MeV
θ = 20°
θ = 0°
T = 3/2
T = 3/2
T = 3/2
T = 3/2
9276
9136
9061
9190
8959
8908
8840
8768
8642
8576
8457
8390
9339
9276
9190
9136
9061
8959
8908
8840
8768
8576
8424
X1/6
NUMBER OF PROTONS
MHz
300
200
100
0
600
400
200
0
33
34

FIGURE 43

An α-particle spectrum from the $^{22}Ne(^{3}He, \alpha)$ reaction on ^{22}Ne gas in the gas target. Groups corresponding to states of ^{21}Ne are marked according to the excitation energy in MeV. Groups corresponding to states of ^{11}C and ^{15}O come from the $(^{3}He, \alpha)$ reaction on small ^{12}C and ^{16}O contaminations of the gas in the gas target. See pages 64 and 65.

FIGURE 43

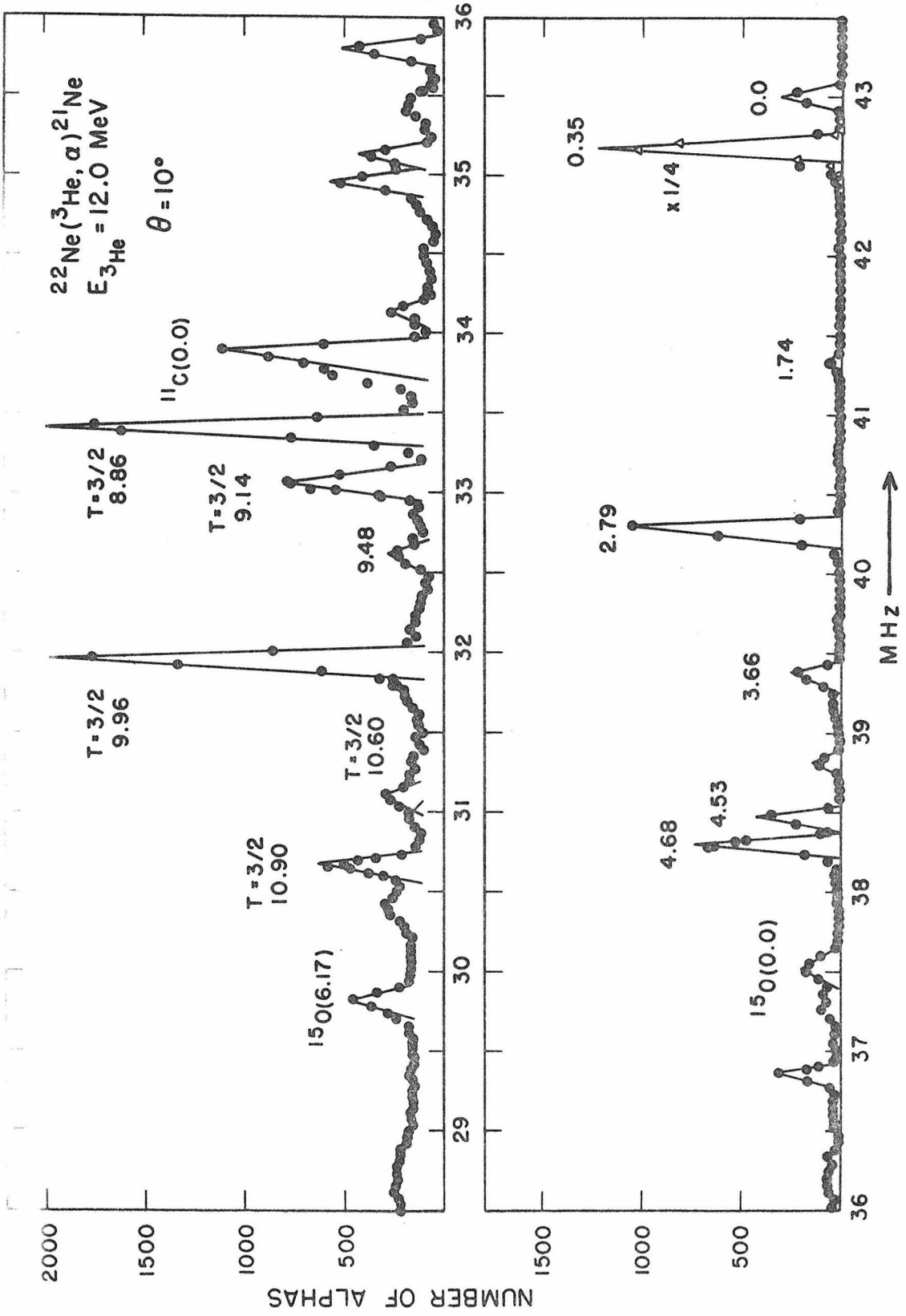
$^{22}Ne(^{3}He,\alpha)^{21}Ne$
$E_{^{3}He}$ = 12.0 MeV
θ = 10°
$^{11}C(0.0)$
T=3/2 8.86
T=3/2 9.14
9.48
T=3/2 9.96
T=3/2 10.60
T=3/2 10.90
$^{15}O(6.17)$
$^{15}O(0.0)$
4.68
4.53
3.66
2.79
1.74
0.35
0.0
x 1/4
NUMBER OF ALPHAS
MHz

FIGURE 44

An isobar diagram for T = 3/2 states with A = 21; all energies are in MeV. The information on ^{21}F comes from Horvat (1964); the information on ^{21}Na comes from McDonald and Adelberger (1968); and the information on ^{21}Mg comes from Butler et al. (1968). For further details concerning this figure, see pages 69 through 71.

FIGURE 44

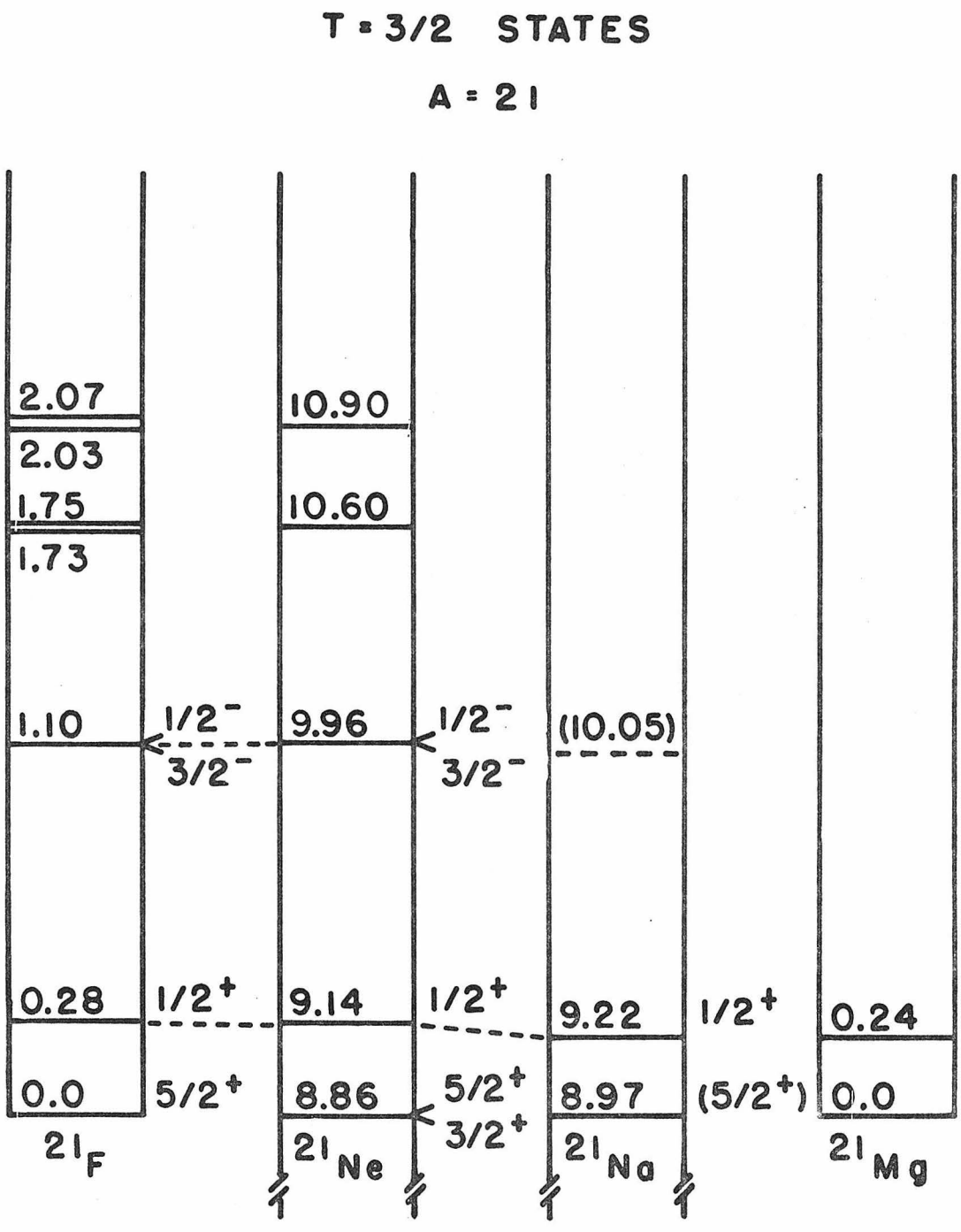
T = 3/2 STATES
A = 21
2.07
2.03
1.75
1.73
1.10
0.28
0.0
21F
1/2−
3/2−
1/2+
5/2+
10.90
10.60
9.96
9.14
8.86
21Ne
1/2−
3/2−
1/2+
5/2+
3/2+
(10.05)
9.22
8.97
21Na
1/2+
(5/2+)
0.24
0.0
21Mg

FIGURE 45

Two α-particle spectra from the $^{22}Ne(^{3}He, \alpha)$ reaction to the excitation region in ^{21}Ne containing the T = 3/2 states. Groups arising from small ^{12}C and ^{16}O contaminations of the ^{22}Ne gas in the gas target can be seen in the spectra; groups corresponding to states of ^{21}Ne are identified by the excitation energy in MeV. See pages 64 and 65.

FIGURE 45

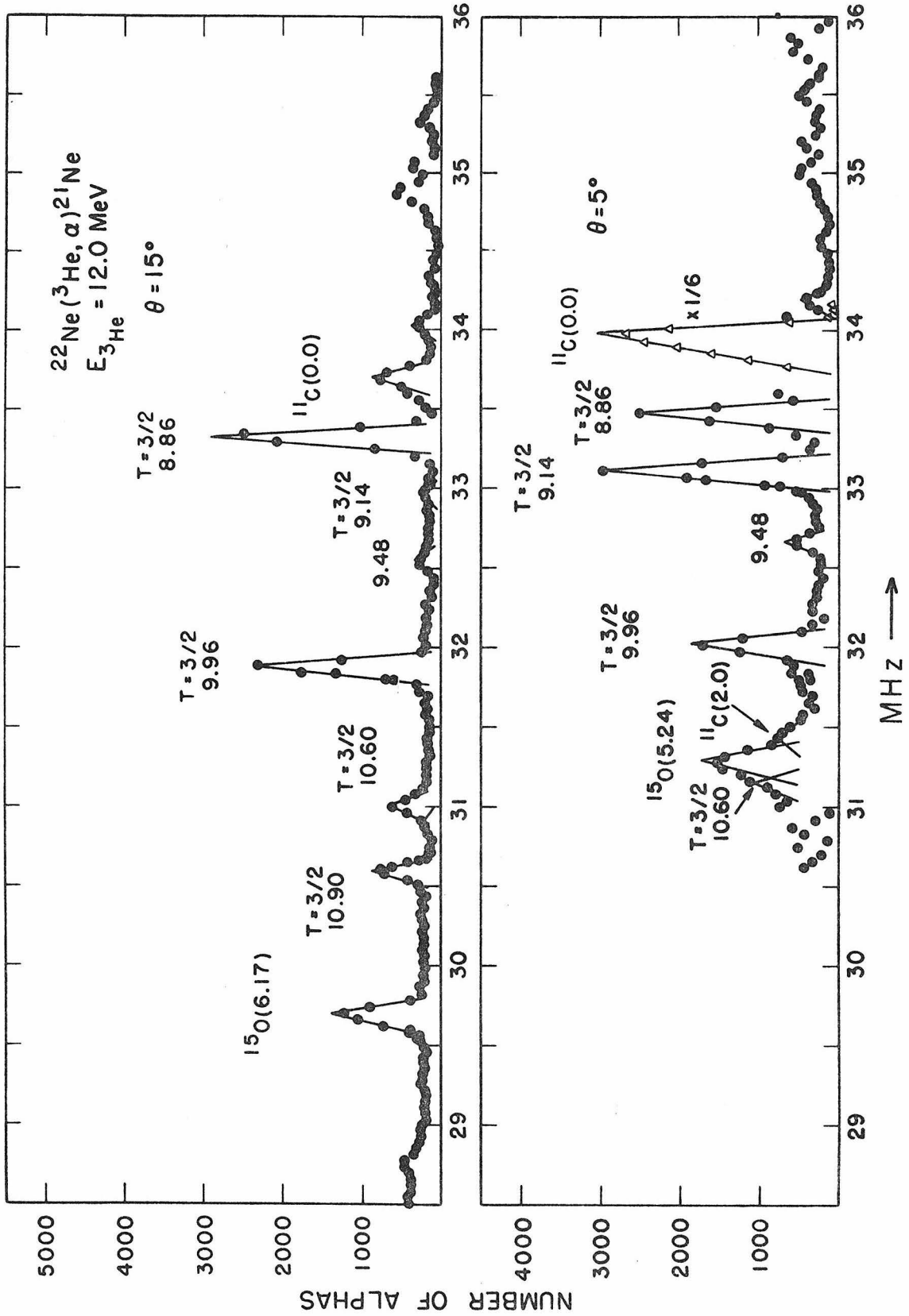
$^{22}Ne(^3He,\alpha)^{21}Ne$
$E_{^3He}$ = 12.0 MeV
θ = 15°
θ = 5°
T = 3/2 8.86
T = 3/2 9.14
T = 3/2 9.96
T = 3/2 10.60
T = 3/2 10.90
$^{11}C(0.0)$
$^{15}O(6.17)$
$^{15}O(5.24)$
$^{11}C(2.0)$
9.48
x1/6
NUMBER OF ALPHAS
MHz

FIGURE 46

Angular distributions from the $^{19}F(^{3}He, p)$ reaction for the two lowest T = 3/2 states in ^{21}Ne. In addition to the probable-error bars indicated in the figure, there is an uncertainty of approximately 10% in the absolute normalization. The smooth curves in the figure are the predictions of the DWBA theory; the dashed curves are the predictions of a PWBA theory (see Appendix IV). See pages 67 and 68.

FIGURE 46

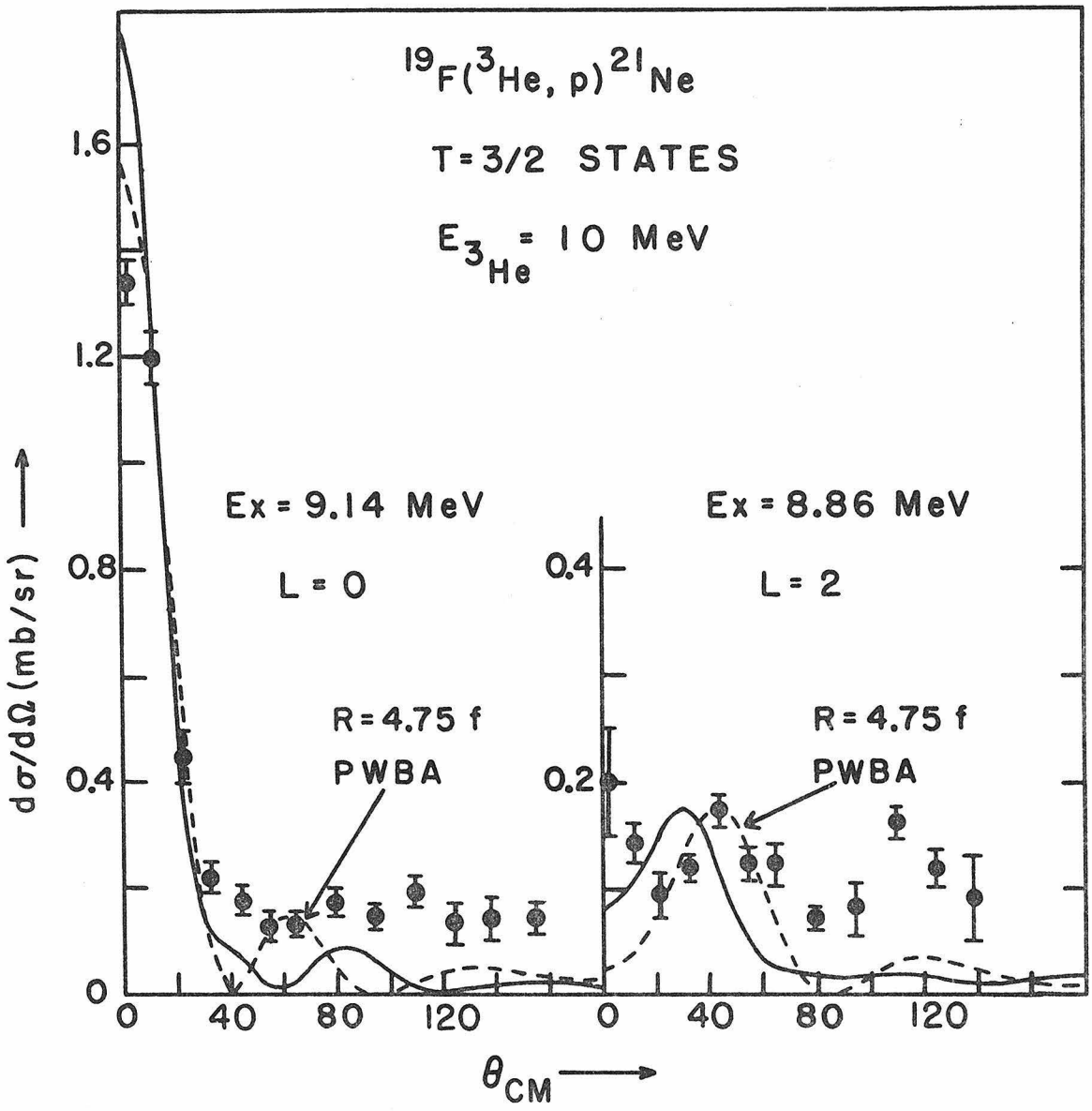
$^{19}F(^{3}He, p)^{21}Ne$
T=3/2 STATES
$E_{^{3}He}$ = 10 MeV
Ex = 9.14 MeV
L = 0
R = 4.75 f
PWBA
Ex = 8.86 MeV
L = 2
R = 4.75 f
PWBA
dσ/dΩ (mb/sr)
θ_{CM}
0
0.4
0.8
1.2
1.6
0.2
40
80
120

FIGURE 47

Angular distributions from the $^{22}Ne(^{3}He, \alpha)$ reaction for T = 3/2 states in ^{21}Ne. In addition to the probable errors indicated in the figure, there is an uncertainty of approximately 20% in the absolute normalization. The effective incident energy was 11.86 MeV after correcting the 12-MeV incident energy for energy losses in the entrance foil and target gas. See pages 68 and 69.

FIGURE 47

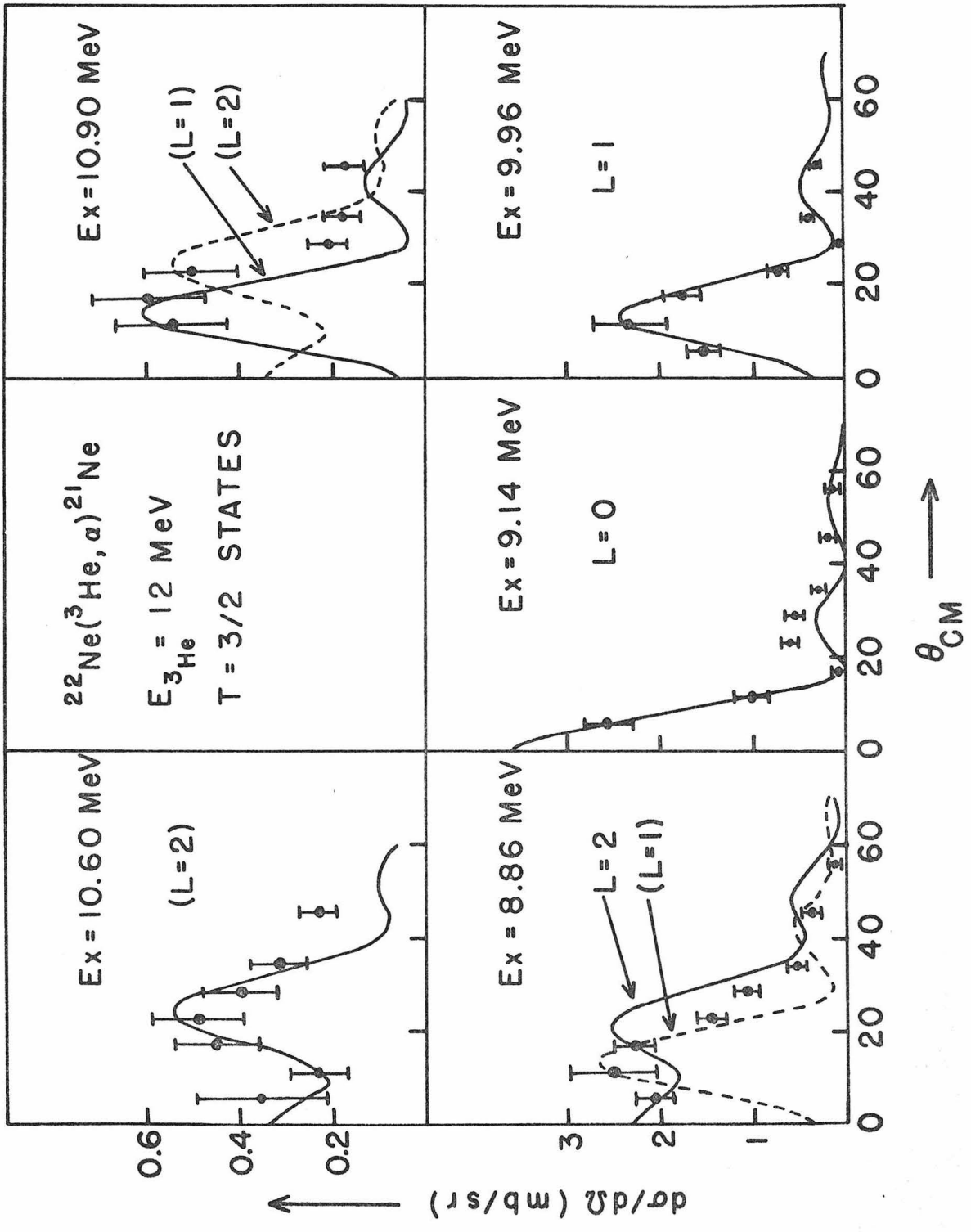
$^{22}Ne(^3He,\alpha)^{21}Ne$
$E_{^3He}$ = 12 MeV
T = 3/2 STATES
Ex = 10.60 MeV
(L=2)
Ex = 10.90 MeV
(L=1)
(L=2)
Ex = 9.96 MeV
L=1
Ex = 9.14 MeV
L=0
Ex = 8.86 MeV
L=2
(L=1)
0.6
0.4
0.2
3
2
1
0
20
40
60
$d\sigma/d\Omega$ (mb/sr)
θ_{CM}